INTEGRATION OF MULTIFOCAL MULTIPHOTON MICROSCOPE (MMM) AND SECOND HARMONIC GENERATION MICROSCOPE (SHG) FOR 3D HIGH-RESOLUTION IMAGING IN LIVER FIBROSIS

PENG QIWEN
(B.S., Southeast University)

A THESIS SUBMITTED
FOR THE DEGREE OF DOCTOR OF PHILOSOPHY

IN COMPUTATION AND SYSTEMS BIOLOGY (CSB)
SINGAPORE-MIT ALLIANCE

NATIONAL UNIVERSITY OF SINGAPORE
2014

DECLARATION

I hereby declare that this thesis is my original work and it has been written by me in its entirety. I have duly acknowledged all the sources of information which have been used in the thesis.

This thesis has also not been submitted for any degree in any university previously.

Peng Qi

Peng Qiwen

18 December 2014

Acknowledgements

The journey of pursuing PhD is full of laugh and tears along with my growth. Studies during the past years have showed me a new world to science and brought wonderful people into my life. First and foremost, I want to give my deepest appreciation to my family, my parents and grandparents for their selfless support and love. They always care my life and my feelings no matter how far I am away from home.

I would like to express my gratitude to my supervisors, Prof. Hanry Yu and Prof. Peter So for their kind guidance and patience. They not only offered advices through all the research problems I have met, but also trained me the way of thinking and working with their great scientific passion and knowledge.

I am very grateful to Mr. Alvin Kang Chiang Huen in Singapore and Dr. Jaewon Cha in MIT for their mentorship. They taught me all the knowledge and skills about optics hand by hand without any reservation in the first two years of my PhD.

I would like to thank all the group members from Yu's lab and So's lab for their kindness of listening and help on the research during my studies. Dr. Yew Yan Seng Elijah, Dr. Zhuo Shuangmu and Mr. Kang Yuzhan helped me on imaging experiments; Dr. Xu Shuoyu gave me many advices on imaging processing; Dr. Xia Lei, Dr. Tong Wen Hao and Ms. Xing Jiangwa shared all my thoughts and feelings.

I also would like to thank my friends Dr. Zhang Chenyu, Dr. Zhang Bo, Dr. Yin Lu, Ms. Shao Yiou and Ms. Zhang Yujie who did not involve in my research work but are very important to make my life better in Singapore.

Last but not least, I want to thank Singapore-MIT Alliance for the scholarship, research funding and giving me such great experience studying in Singapore and MIT.

Table of Contents

Summary

Liver fibrosis is the consequence of a sustained wound-healing response to chronic hepatocellular damage and it leads to mechanical and biochemical alteration of the tissue environments. As one of the most significant phenomena and diagnostic characteristics, excessive accumulation of the extra cellular matrix (ECM) distorts the hepatic architecture and deteriorates hepatocellular function. Since both fibrosis progression and regression are inhomogeneous, it is important to investigate the whole tissue spatial relationship between stiffening and biochemical responses by measuring, quantifying and spatially locating variations of ECM and cellular structure/functional changes. Imaging is an established technique to obtain such information. We have previously established second harmonic generation (SHG) microscope as a label-free technique for collagen quantification. However, one drawback of conventional microscopes is that the frame rate is limited by the time-consuming point-wise scanning process. By using multifocal multiphoton microscopy (MMM), we can not only quantify tissue morphology and physiology with sub-cellular resolution and also dramatically improve the imaging speed. In this thesis, the correlation of forward second harmonic generation (SHG) signal and backward SHG signal in different liver fibrosis stages has been investigated. The combination of the various features can provide a more accurate prediction than each feature alone in fibrosis diagnosis. To realize fast speed imaging, an integrated imaging system composed of both MMM and SHG techniques is established to scan a specimen with multiple excitation foci instead of a single excitation focus so that imaging speed is enhanced 64 times. A novel descanned mode and image post processing for emission photon reassignment have been investigated for signal-to-noise ratio (SNR) improvement. Coupled with an automated slicing module, a large volume tissue sample can be imaged at a high speed in order to spatially locate and study collagen variation in the development of liver fibrosis.

List of Publications

1. **Q. Peng**, S. Zhuo, P. T. C. So and H. Yu, “Improving liver fibrosis diagnosis based on forward and backward second harmonic generation signals,” *Applied Physics Letters*, 106(8), 083701 (2015).

2. S. Zhuo, J. Yan, Y. Kang, S. Xu, **Q. Peng**, P. T. C. So and H. Yu, “In vivo, label-free, three-dimensional quantitative imaging of liver surface using multi-photon microscopy,” *Applied Physics Letters*, 105(2), 023701 (2014).

3. S. G. Stanciu, S. Xu, **Q. Peng**, J. Yan, G. A. Stanciu, R. E Welsch, P. T. C. So, G. Csucs and H. Yu, “Experimenting liver fibrosis diagnostic by two photon excitation microscopy and Bag-of-Features image classification,” *Scientific Report*, 4, 4636 (2014).

4. K. P. Divya, S. Sreejith, A. Pichandi, Y. Kang, **Q. Peng**, S. K. Maji, Y. Tong, H. Yu, Y. Zhao, P. Ramamurthy and A. Ajayaghosh, “A ratiometric fluorescent molecular probe with enhanced two-photon response upon Zn2+ binding for in vitro and in vivo bioimaging,” *Chemical Science*, 5(9), 3469-3474 (2014).

5. J. W. Cha, V. R. Singh, K. H. Kim, J. Subramanian, **Q. Peng**, H. Yu, E. Nedivi and P. T. C. So, “Reassignment of scattered emission photons in multifocal multiphoton microscopy,” *Scientific Report*, 4, 5153 (2014).

6. S. Xu, Y. Wang, D. C. Tai, S. Wang, C. L. Cheng, **Q. Peng**, J. Yan, Y. Chen, J. Sun, X. Liang, Y. Zhu, J. C. Rajapakse, R. E Welsch, P. T. C. So, A. Wee, J. Hou, H. Yu, “qFibrosis: A fully-quantitative innovative method incorporating histological features to facilitate accurate fibrosis scoring in animal model and chronic hepatitis B patients,” *Journal of Hepatology*, 61(2), 260-269 (2014).

7. B. C. Narmada, Y. Kang, L. Venkatraman, **Q. Peng**, R. B. Sakban, B. Nugraha, X. Jiang, R. M. Bunte, P. T. C. So, L. Tucker-Kellogg, H. Q. Mao and H. Yu, “Hepatic stellate cell-targeted delivery of hepatocyte growth factor transgene via bile duct infusion enhances its expression at fibrotic foci to regress dimethylnitrosamine-induced liver fibrosis,” *Human Gene Therapy*, 24(5), 508-519 (2013).

8. Y. He, C. H. Kang, S. Xu, X. Tuo, S. Trasti, D. C. S. Tai, A. M. Raja, **Q. Peng**, P. T. C. So, J. C. Rajapakse, R. Welsch and H. Yu, “Toward surface quantification of liver fibrosis progression,” *Journal of Biomedical Optics*, 15(5), 056007 (2010).

List of Tables

List of Figures

List of Symbols and Abbreviations

1D	One-dimensional
2D	Two-dimensional
2PE	Two-photon excitation
3D	Three-dimensional
3PE	Three-photon excitation
AOD	Acousto-optical deflector
AOM	Acousto-optic modulator
BDL	Bile duct ligation
BRC	Biological Resource Centre
CARS	Coherent anti-Stokes Raman scattering
CCD	Charge coupled device
CMOS	Complementary metal–oxide–semiconductor
DMN	Dimethylnitrosamine
DOE	Diffractive optical element
ECM	Extra cellular matrix
FPGA	Field-programmable gate array
FWHM	Full-width at half-maximum
GFP	Green fluorescent protein
GMM	Gaussian mixture model

GVD	Group velocity dispersion
HAI	Histologic activity index
HGF	Hepatocyte growth factor
HSC	Hepatic stellate cell
IACUC	Institutional Animal Care and Use Committee
ip.	Intra-peritoneal injection
IR	Infra-red
lp	Line-pair
MAPMT	Multi-anode photomultiplier tubes
MMM	Multifocal multiphoton microscopy
MMP	Matrix metalloproteinase
MT	Masson's trichrome
NA	Numerical aperture
NASH	Non-alcoholic steatohepatitis
OI	Osteogenesis imperfect
PBS	Phosphate buffer solution
PMT	Photomultiplier tube
PSF	Point spread function
ROC	Receiver operating characteristic
SD	Standard deviation
SHG	Second harmonic generation
SNR	Signal-to-noise ratio
SVM	Support vector machine

TAA	Thioacetamide
TGF-β1	Transforming growth factor-β1
THG	Third harmonic generation
TIMP	Tissue inhibitor of metalloproteinase
TPEF	Two-photon excited fluorescence
TSP1	Thrombospondin-1

Chapter 1

Introduction

Liver fibrosis is the consequence of a sustained wound-healing response to chronic hepatocellular damage that may result in cirrhosis, liver failure, and portal hypertension [1, 2]. The damage can result from a variety of causes including viral, autoimmune, drug induced, cholestatic and metabolic diseases [3]. One of the most significant phenomena and diagnostic characteristics of liver fibrosis is excessive accumulation of the extra cellular matrix (ECM) proteins, including: collagens, proteoglycans and glycoproteins [4]. During liver injury, the accumulation of ECM proteins distorts the hepatic architecture by forming a fibrous scar, causing hepatocellular function to deteriorate. Subsequent development of nodules of regenerating hepatocytes defines cirrhosis, the advanced stage of fibrosis [3, 4].

Currently, percutaneous liver biopsy is still the gold standard for the diagnosis and assessment of liver fibrosis [5]. Additionally, researchers have reported many noninvasive methods to diagnose and monitor liver fibrosis and its treatment, such as testing serum aminotransferase levels [6] and markers including laminin [7], cytokines [8, 9], collagens [9] etc. However, both progression and regression processes of liver fibrosis are inhomogeneous. All the methods mentioned above have either small sampling or low sensitivity that is insufficient to correctly quantify fibrotic status. To better understand progression and regression processes of liver fibrosis, spatial and temporal information are required. With the development of mode-locked lasers and related optical techniques, non-linear microscopy with its advantages of high resolution and deep penetration becomes an affordable option for three-dimensional (3D) high resolution tissue imaging.

Among various multiphoton processes, two-photon excited fluorescence (TPEF) and second harmonic generation (SHG) signals are commonly used to detect cells and fibers respectively. In particular, the feasibility of using SHG microscopy in monitoring fibrosis in livers has been demonstrated [10, 11]. Combined TPEF and SHG microscopy was utilized for highly sensitive collagen quantification and for collagen remodeling study during the early stages of liver fibrosis. The results have showed that subtle changes in the distribution, amount of collagen and cell morphology are quantitatively characterized in the TPEF/SHG images without tissue staining.

However, a practical limitation of conventional multiphoton microscopy is its imaging speed which typically ranges from 0.1 to 2 frames per second [12]. This speed is not sufficient to do 3D imaging for large tissue volume. Besides using higher speed scanners and wide-field technique, a means to increase acquisition speed and fully utilize laser power is to parallelize the multiphoton imaging process by multifocal multiphoton microscopy (MMM) [13]. So far, all MMM setups have been built focus on the improvement of either multifocal generation or signal detection. Moreover, they all have only one channel and most of them acquire TPEF signals. However, it is crucial to obtain collagen signals as well for liver fibrosis studies. Therefore, the purpose of this thesis is to study liver fibrosis by using a new high resolution MMM system integrated with SHG microscopy.

A complete literature review is presented in Chapter 2, including liver fibrosis and its diagnosis, nonlinear optics, techniques for increasing imaging speed and different types of MMM. Chapter 3 gives a summary of limitations of current work and specific aims of this project.

Chapter 4 demonstrates the feasibility of liver fibrosis staging by analyzing both forward and backward SHG signals and their average intensity ratio. An improvement on fibrosis diagnosis can be achieved with combination of features using a support vector machine (SVM) algorithm. To study liver fibrosis staging, animal model establishment is necessary to be done and optimized. Bile duct ligation (BDL) and drug induction are two main methods to induce liver fibrosis. In this study, we chose Thioacetamide (TAA) as the induction drug. However, to focus on the main problem, comparison of different animal models is discussed in less detail even though they are very important for liver fibrosis study.

The next chapter (Chapter 5) describes the design and construction of a new MMM system for the needs of imaging speed enhancement and TPEF/SHG acquisition. The chapter recounts all the mechanical, optical and electrical components in the system. Basic measurements and tests for main parts, such as DOE and discriminators are discussed.

Chapter 6 presents the characteristics and improvement of the new MMM system for the study of liver fibrosis. High resolution is validated by doing pixel size measurement, fluorescent beads visualization and optical resolution measurement. To present high-quality liver images, a post-processing method based on maximum likelihood estimation algorithm is developed to increase signal-to-noise ratio (SNR). Furthermore, an automated slicing module is designed and implemented into the system to realize large volume tissue imaging for future 3D reconstruction.

Chapter 2

Background

2.1 Liver fibrosis

2.1.1 Liver and liver fibrosis

Liver is the second largest organ in human body and performs many essential functions, including glycogen storage, decomposition of red blood cells, plasma protein synthesis, hormone production, and detoxification. These functions related to digestion, metabolism, immunity, and the storage of nutrients make the liver a vital organ; without which the tissues of the body would quickly die from lack of energy and nutrients [14].

At the cellular level, the parenchyma of liver are made up of microscopic units called lobules (Figure 2.1), the hexagonal-shaped structural units of the liver. They are comprised of lines of hepatocytes from a central point and blood-filled sinusoids between the cells. At the “corners” of a lobule, there are portal tracts which consist of adjacent and parallel terminal branches of bile ducts, portal veins, and hepatic arteries that border the hepatocytes. Terminal branches of the central veins are in the center of hepatic lobules. Blood flows from the portal tracts past the hepatocytes and drains via central veins and then transports out of the liver.

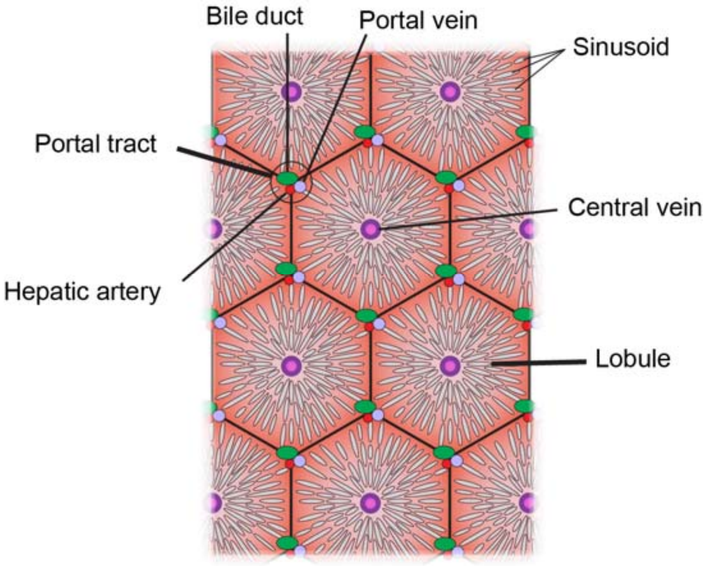

Figure 2.1 Structure of standard liver tissue with lobules - the structure unit of the liver. Blood flows from the portal tracts consisted of portal veins, hepatic arteries and bile ducts, past lines of hepatocytes and drains via central veins which locate at center of the lobules.

Liver fibrosis is the consequence of a sustained wound-healing response to chronic hepatocellular damage and it may result in cirrhosis, liver failure, and portal hypertension [1]. The damage can be resulted from a variety of causes including viral, autoimmune, drug induced, cholestatic and metabolic diseases [3] and recently non-alcoholic steatohepatitis (NASH) is considered to be a leading cause of fibrosis.

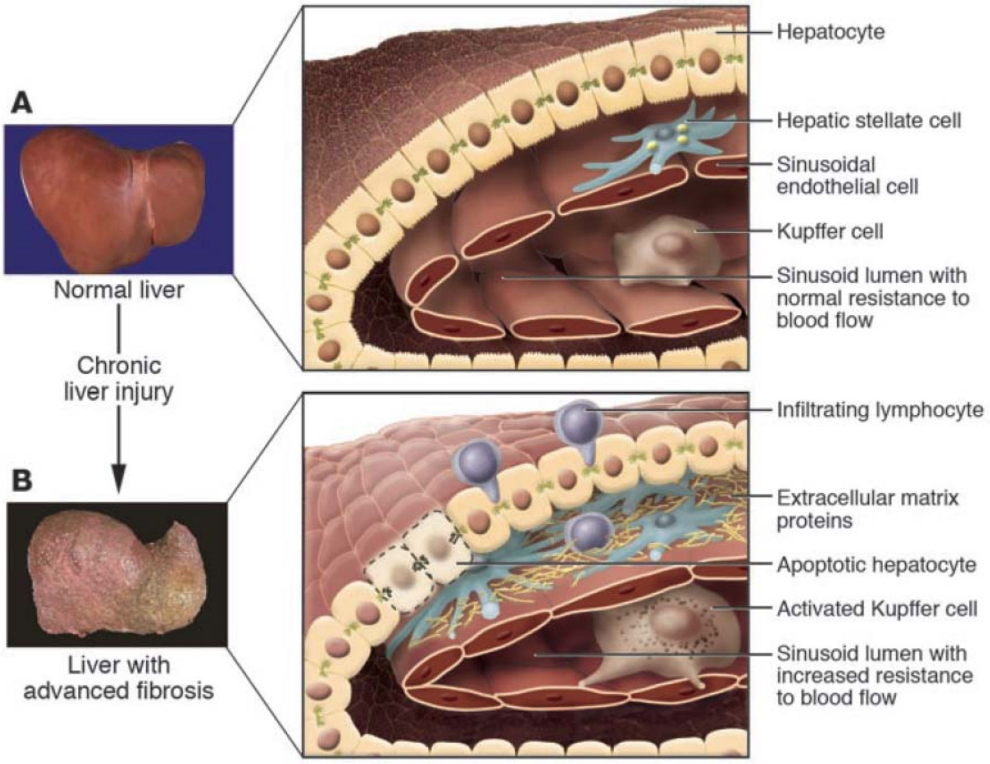

Figure 2.2 Changes in the hepatic architecture (A) associated with advanced hepatic fibrosis (B). Following chronic liver injury, inflammatory lymphocytes infiltrate the hepatic parenchyma. Some hepatocytes undergo apoptosis, and Kupffer cells activate, releasing fibrogenic mediators. HSCs proliferate and undergo a dramatic phenotypical activation, secreting large amounts of ECM. Sinusoidal endothelial cells lose their fenestrations, and the tonic contraction of HSCs causes increased resistance to blood flow in the hepatic sinusoid. (Adapted from [1], reprinted with permission.)

One of the most significant phenomena and diagnostic characteristics of liver fibrosis is excessive accumulation of ECM proteins that represent approximately 30% of the total structural proteins in mammalian tissues [15]. A limited deposition of ECM associated with an inflammatory response occurs as a repair mechanism after an acute liver injury. Regeneration fails, however, when the hepatic injury persists and deregulation of the normal healing does not repair effectively enough, resulting in liver fibrosis and massive deposition of ECM (Figure 2.2). In advanced stages, the overall amount of ECM in the liver increases by approximately six-fold compared with that in normal livers. During this process, the accumulation of ECM proteins distorts the hepatic architecture by becoming scar-like, and hepatocellular function deteriorates. Even when the density is low; ECM provides signals that maintain the differentiating function of surrounding cells. Subsequent development of nodules of regenerating hepatocytes defines cirrhosis, the advanced stage of fibrosis [1, 3].

Activation of Hepatic Stellate Cells (HSCs) is believed to be the major cause of ECM accumulation [16]. HSCs, comprising 15% of liver cells, are normally in their quiescent state [2]. In the normal liver, HSCs reside in the sinusoidal space of Disse and are the major storage sites of vitamin A. After chronic injury, HSCs become myofibroblast-like and proliferative (activated state) [16] (Figure 2.2). Activated HSCs migrate and accumulate at the sites of tissue repair, secreting large amounts of ECM, mainly type I collagen and regulating ECM degradation. Activated HSCs cause accumulation of ECM in mainly three ways: 1) increase synthesis of ECM proteins; 2) decrease activity of ECM-removing matrix metalloproteinases (MMPs) [17]; and 3) over-express specific tissue inhibitor of metalloproteinases (TIMPs) [18], which are the inhibitors of MMPs. These changes in ECM related proteins are correlated to fibrosis [16]. If HSCs are activated, they can go into self-activation. During activation, HSCs produce much more thrombospondin-1 (TSP1) [19]. Subsequently, TSP1 will activate more transforming growth factor-β1 (TGF-β1), which can activate HSCs. Therefore, HSCs can activate themselves once stimulated. Besides HSCs, other cell sources also contribute to fibrogenic populations in liver, including bone marrow, portal fibroblasts and epithelial mesenchymal transition.

Collagen is a major fibrillar protein present in the ECM; it constitutes the principal structural protein in mammalian tissues [15]. Fibril-forming or fibrillar collagens include type I, II, III, XI and type XXIV, XXVII collagen that are discovered more recently. Being a largely mechanical role, they provide tensile strength to both tissues and organs [20]. They are the most plentiful and widely distributed in the body (Table 2.1) [21].

During fibrogenesis, accumulated ECM includes collagen type I, III and IV. The fibrotic process initially occurs on a background of progressive changes in the surrounding ECM within the subendothelial space of Disse. Over time, the matrix composition changes from one comprised of collagen type IV to one rich in fibril-forming collagens, predominantly collagen I and III. Type I increases most and its ratio to types III and IV also increases [22, 23]. As the prototype constituent of the fibril-forming matrix in fibrotic liver, collagen type I degradation is being particularly important for recovery of normal liver histology [24].

Table 2.1 The members of fibrillar collagen family and tissue distributions in the body.

Fibrillar Collagen Type	Tissue distribution
I	Throughout the body except in the cartilage, bone, skin, tendon, ligaments, cornea
II	Cartilage, vitreous body, nucleus pulposus
III	Blood vessels, intestinal organs, cartilage, skin
V	Bone, cornea, lung, fetal membranes
XI	Articular cartilage, vitreous body
XXIV	Bone and cornea
XXVII	Cartilage

2.1.2 Diagnosis of liver fibrosis

Currently biopsy is still considered to be the gold-standard method for detecting changes in liver fibrosis even though it is an invasive procedure [25]. Based on the biopsy, a grade or stage is evaluated by pathologists to predict patient outcome. This stage is a measure of how far the liver fibrosis has progressed in its natural history. In most of chronic liver diseases, the end stage is cirrhosis with clinical decompensation, while earlier stages represent mild fibrosis or cirrhosis. This grading method should ideally predict the severity of the underlying liver disease and guide further therapies [26]. Histopathologic features that can be considered for grading and staging in nonneoplastic liver diseases include hepatocellular changes, inflammation of lobular and portal areas, biliary changes, fibrosis and architectural changes. Specific staining of ECM proteins (with Sirius red or Masson's trichrome (MT)) is used for such histological grading.

There are a few grading systems that are widely used for chronic hepatitis. They all describe fibrosis progression from none to fibrous portal expansion to bridging fibrosis to incomplete cirrhosis and finally to established cirrhosis. The Metavir is a simple one [27]. It categorizes the disease process into five stages as F0-F4. The Knodell score is a more complex system based on histologic activity index (HAI) [28]. It is composed of four individually assigned numerical numbers that make up a single score. Among the four components, fibrosis degree is also scored from 0 to 4. The Ishak score is another commonly used grading system that is modified from Knodell score [29]. In this score, stage is ranged from 0 to 6.

Table 2.2 describes the grading systems of Meravir, Knodell and Ishak respectively and their descriptions on different liver fibrosis degrees.

However, there are two main limitations for biopsy: sampling error and interobserver variability [30]. Since a needle for liver biopsy only removes 1/50000 of the total organ, probability of sampling error is substantial when performing grading and staging. Based on autopsy and laparoscopy study, cirrhosis is missed on single blind biopsy in about 10% to 30% of cases [31-33]. To avoid sampling error, at least 15 mm long and containing more than 5 portal tracts are suggested for an adequate biopsy sample [34, 35]. On the other hand, subjectivity occurs during pathologic assessment. Sometimes histological examination does not predict disease progression well, although excellent inter- and intra-observer reproducibility can be achieved based on developed score system as discussed earlier [36].

Table 2.2 Grading and staging systems for chronic liver fibrosis using different scoring systems.

Score	Metavir	Knodell	Ishak
0	No fibrosis	No fibrosis	No fibrosis
1	Fibrous portal expansion	Fibrous portal expansion	Fibrous expansion of some portal areas, with or without short fibrous septa
2	Few bridges or septa		Fibrous expansion of most portal areas, with or without short fibrous septa
3	Numerous bridges or septa	Bridging fibrosis	Fibrous expansion of most portal areas with occasional portal to portal bridging
4	Cirrhosis	Cirrhosis	Fibrous expansion of portal areas with marked bridging (portal to portal as well as portal to central)
5			Marked bridging (portal-portal and/or portal-central) with occasional nodules (incomplete cirrhosis)
6			Cirrhosis, probable or definite

Besides liver biopsy, plenty of putative serum markers have been evaluated for liver fibrosis assessment and can be considered into direct or indirect category. Direct serum assays reflect serum ECM turnover, while indirect markers including platelet count, coagulation studies and hepatic aminotransferases reflect alterations in hepatic function but not hepatic ECM metabolism [37, 38]. These scores can detect mild and advanced fibrosis but are not accurate for intermediate grades.

2.2 Nonlinear optical microscopy

As a commonly employed approach, by expressing fluorescently labeled proteins or protein subdomains in living cells, imaging via fluorescence microscopy is able to probe the interactions between proteins, their localization, and structural dynamics that are critical in modern cell biology [39]. Over the past few decades, developments in fluorescence microscopy have enabled biological imaging studies to move from the single cell level to the tissue level and even to whole animals. Two key developmental techniques in this field are using green fluorescent protein (GFP) as a marker of gene expression and protein localization as well as using the optical sectioning microscope which allows 3D imaging dataset from the intact, live sample [40]. Nonlinear microscopy with its distinct advantages for 3D imaging is considered to be an alternative to conventional confocal microscopy for the imaging of biological samples.

Multiphoton (two or more photons) processes are divided into two categories of absorption and scattering depending on the interaction between photons and specimens. The useful multiphoton absorption events are two- and three-photon excitation (2PE, 3PE); while the scattering events are second and third harmonic generation (SHG, THG), as well as coherent anti-Stokes Raman scattering (CARS). Comparing to single-photon actions, the most remarkable advantage of multiphoton phenomena is the restriction of multiphoton occurrence at focal region so as to generate more accurate signals. Moreover, multiphoton events provide capability to penetrate deeper into specimens which are highly scattering, such as liver tissues. In addition, signals generated from SHG, THG, and CARS are not accessible through single-photon interactions, hence it is complementary to fluorescence imaging [41].

2.2.1 Fundamentals of nonlinear optics

Nonlinear optical phenomena arise from the interaction of intense light with a material, thereby modifying the optical properties of that material system. In order to understand optical nonlinearity, we begin with the dipole per unit volume or the macroscopic polarization P which is proportional to the electric field strength in the regime of linear optics [42].

$$P = \varepsilon_0 \chi^{(1)} E \tag{2.1}$$

where ε_0 is the relative permittivity of free space and $\chi^{(1)}$ is the proportionality constant known as linear susceptibility of the medium. Under intense laser irradiation whereby the electric field strength becomes comparable to the intra-atomic electric field, nonlinear responses can be seen as deviations from the linear response and therefore can be described as a power series expansion in the field as

$$P = \varepsilon_0 \left(\chi^{(1)} E + \chi^{(2)} EE + \chi^{(3)} EEE + \ldots \right) \tag{2.2}$$

where $\chi^{(2)}$ and $\chi^{(3)}$ are the nonlinear susceptibilities of the medium. These three terms describe a large proportion of the diverse optical phenomena that we are familiar. The linear term gives rise to index of refraction, absorption, dispersion and birefringence of a medium, the second-ordered term gives rise to second harmonic generation which is only possible in non-centrosymmetric media, while the third-ordered term gives rise to third harmonic generation and two-photon absorption. We consider second harmonic generation and two-photon absorption processes in greater details as they are the underlying principles used in this work.

2.2.2 Theory of TPEF and SHG

Two-photon absorption was first predicted by Maria Goeppert-Mayer in her doctoral thesis in 1931 [43] and later observed experimentally in 1962 by Abella [44]. Two photons of longer wavelength than required for transitions between two energy states are simultaneously absorbed to excite electrons of the molecule from the lower energy state to the higher energy state. Using longer wavelengths for excitation, for example in the infrared, is advantageous in the study of biological specimens in that these wavelengths are scattered to a lesser extent and hence are able to penetrate deeper into the sample as compared to visible wavelengths.

In two-photon processes, a transition between states of same parity is allowed, unlike the case for one-photon transitions where it is forbidden [45]. These photons must arrive within approximately 0.5 fs [46] in time for simultaneous absorption and for signals to be observable, the concentration of photon flux has to be on the order of 10^{31} photons/cm^2 s [47]. It is therefore necessary to have tight-focusing and high temporal control. Hence, we would require high numerical aperture (NA) objective lenses and ultrafast pulsed lasers to satisfy the above criteria. The probability of TPA, n_a, was empirically found to be [47]:

$$n_a \propto \frac{\delta_2 P_{\mathrm{ave}}^2}{\tau_p f_p^2}\left(\frac{(\mathrm{NA})^2}{2\hbar c\lambda}\right)^2 \tag{2.3}$$

where δ_2 is the two-photon cross-section of the molecule, P_{ave} is the time averaged power of the laser beam, τ_p is the pulse duration, f_p is the repetition rate of the pulses, NA is the numerical aperture of the objective lens, and λ is the wavelength of the laser. Typically, the state-of-the-art instrumentation parameters would result in saturation of the fluorescence output at one photon pair per pulse per fluorescence. Upon excitation by two-photon absorption, the molecule relaxes via the fluorescence pathway in the time frame of nanoseconds and, unlike single photon excited fluorescence which falls off quadratically from the focus, the fluorescence intensity following a two-photon excitation falls of as the fourth power of the distance from the focus. This would mean that the signals come essentially from very close regions of the focal volume giving rise to an intrinsic optical sectioning capability without a confocal pinhole.

The second order term in the expansion of the macroscopic polarization arises only when light of sufficiently high intensity passes through a non-centrosymmetric medium. This is due to the fact that the polarization depends only on the square of the electric field thereby oppositely directed fields in centrosymmetric media will not have effect on it. This second order polarization can be explicitly written as [42]:

$$P^{(2)}(t) = 2\varepsilon_0 \chi^{(2)} E E^* + \left(\varepsilon_0 \chi^{(2)} E^2 e^{-i2\omega t} + \text{c.c.}\right) \tag{2.4}$$

From the second term of the above equation, it can be seen that the nonlinear field created in the medium has frequency twice that of the input light. This process can be thought of as the annihilation of 2 photons of frequency, ω, for the generation of 1 photon of double the frequency, 2ω with the promotion of an electron from the ground state to a virtual state.

The intensity of the radiated field can be found from [42]:

$$I_2(L) = \sqrt{\frac{\mu_0}{\varepsilon_0}} \frac{2\omega^2}{n_1^2 n_2 c^2} [\chi^{(2)}]^2 I_1^2 L^2 \left[\operatorname{sinc}^2\left(\frac{\Delta k L}{2}\right)\right] \tag{2.5}$$

where L is the length in the propagation direction. One of the critical conditions for frequency doubling to grow within the medium is that the wavevectors of the incident and second harmonic waves must satisfy the phase matching condition [42]:

$$\Delta k = k_{2\omega} - 2k_{\omega} = 0 \tag{2.6}$$

Otherwise, the efficiency of conversion of the power of the second harmonic field from the incident field will be greatly reduced. The attainment of this phase matching condition has been very well studied in crystal optics and there exist remedial methods to circumvent the condition such as quasi-phase matching, as the ideal state of perfect phase matching is not realistically achievable. Phase matching conditions in biological tissues have been studied to great details by Campagnola *et al* [48].

2.2.3 Nonlinear optics used in biological research

Nonlinear microscopy has been considered as a reliable method for imaging of biological samples thanks to its extraordinary advantages of 3D imaging: 1) The short, high-energy pulses impinging on the samples could reduce photodamage and phototoxicity; 2) The longer excitation wavelengths in the near-infrared range can reach deeper penetration and reduce scattering in the tissue; 3) Especially for SHG that relate to intrinsic structure of the materials, no fluorescent proteins or dyes are required.

Nonlinear imaging has been successful in applications of various biological fields. The TPEF microscopy has been used to map network organization of neuronal electrical activity [49] and visualize dendritic spine motility [50], to describe 3D blood flow architecture in brain [51], to Quantitatively imaging of immune-cell motility and morphology [52], such as the in vivo interaction of T cells and dendritic cells (DCs) dynamics in lymph nodes [53], in cranial bone marrow [54] and in tumors [55]. It also permits in vivo imaging using invasive procedures such as implantable windows [56]. SHG imaging has been using in two main biological areas of measuring neurons and collagen due to their special structural properties [57, 58]. In particular, SHG can be used for quantitative assessment of collagen in various organs as an indication of fibrosis development [59, 60].

Nonlinear microscopy has demonstrated far-reaching advantages in cancer research, including melanoma, breast cancer, cervical and ovarian cancer in both animal and human studies [61-63].

2.2.4 Application of TPEF and SHG in the study of liver fibrosis

With the development of mode-locked lasers and nonlinear optical techniques, TPEF and SHG become an affordable option for tissue imaging, especially for measurement of collagen, given the properties of SHG. In particular, the feasibility of using SHG microscopy in monitoring fibrosis in livers has been demonstrated [11, 64, 65].

Our group has utilized combined TPEF and SHG microscopy for highly sensitive collagen quantification and for collagen remodeling study in early stages of liver fibrosis. The results obtained using TPEF/SHG microscopy are standardized and highly reproducible. Subtle changes in distribution and amount of collagen and cell morphology are quantitatively characterized in the TPEF/SHG images; thus they are monitor the structural progression of collagen at all stages of liver fibrosis [11]. We have also developed a standardized quantification system in continuum for liver fibrosis assessment, Fibro-C-Index, which is based on the morphological characteristics and spatial distributions of the collagen in the background tissue and cellular damage [66]. The feasibility of this quantification system is further verified in clinical diagnosis by performing a preliminary trial using human tissue. Figure 2.3 shows the images of BDL-induced liver fibrosis at different stages taken by conventional MT staining and integrated TPEF and SHG microscope. The pathological development of liver fibrosis, including changes in collagen fibers, bile duct, and hepatocyte morphology, could be clearly recorded by TPEF/SHG imaging without the need for tissue staining.

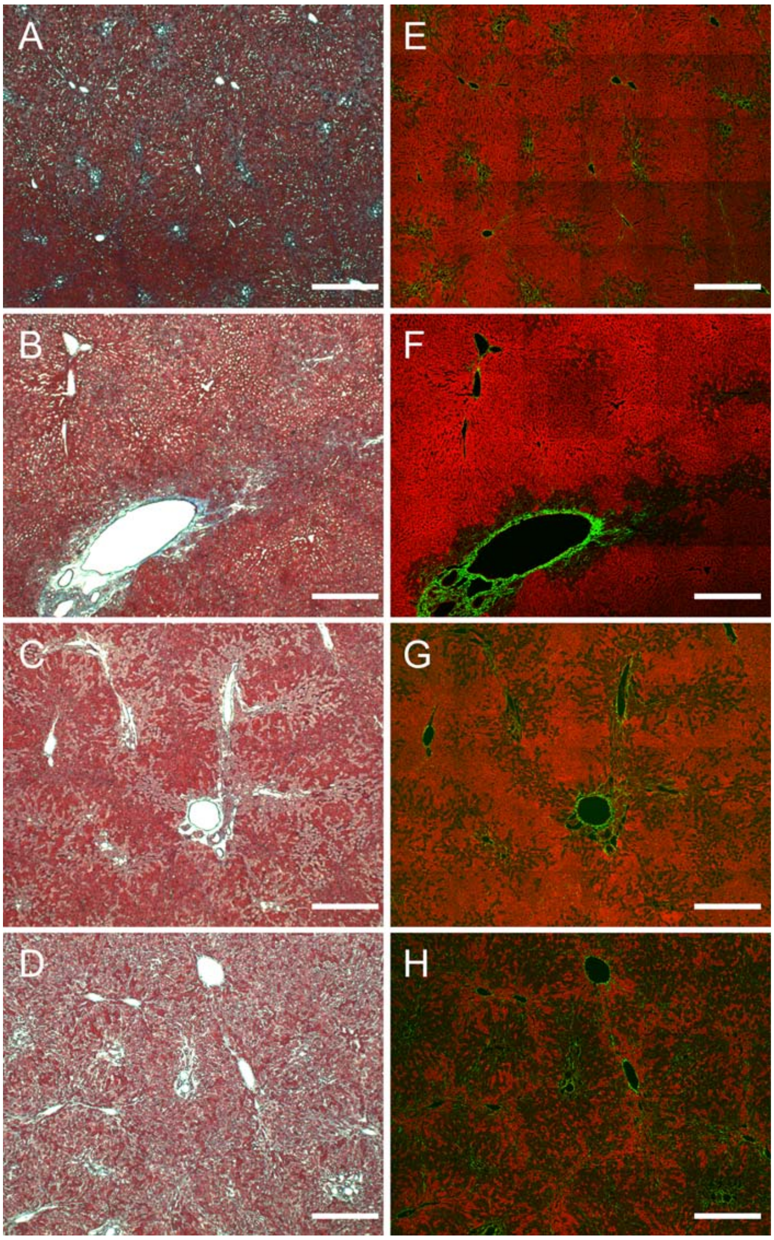

Figure 2.3 Morphological changes at different stages of liver fibrosis recorded with (A) to (D) conventional Masson Trichrome staining, as well as (E) to (H) TPEF and SHG microscopy. (Adapted from [66], reprinted with permission.)

2.3 Multifocal multiphoton microscopy (MMM)

2.3.1 Methods to improve imaging speed of multiphoton microscopy

A practical limitation of conventional multiphoton excitation fluorescence microscopy is its imaging speed which is typically up to several frames per second. This speed can realistically study only a few hundred cells without providing comparable statistical accuracy and precision of quantitative assays such as flow cytometry. Moreover, some other application cases also demand faster systems, including measurement of dynamic processes [67-69], studies of tissues and organs that have larger structures [70, 71]. Therefore, high-speed imaging technique is necessary for large volume tissue imaging.

To date, three kinds of methods have been implemented to increase imaging speed. The first method is using higher speed scanners instead of galvanometric mirror scanners those are used in conventional multiphoton microscopy. In 1999, Kim et al developed a high-speed two-photon microscopy with submicrometer resolution by a polygonal mirror scanner which is based on raster scanning of a single diffraction-limited spot [72]. Using this microscope, the scanning rate is approximately 100 times faster than conventional scanning microscopy.

In the same year Fan and colleagues developed another high-speed two-photon microscopy with a resonant mirror scanner whose maximum frame rate achieves 240 frames/s [73]. Besides, acousto-optical deflectors (AODs) have been utilized by a few groups to enhance scanning speed [74-77]. In general, a scanning speed of about 30 frames per second has been achieved by these high speed scanners with a comparable imaging depth in tissues to conventional multiphoton microscopy. However, an increase in frame rate is obtained by reducing pixel dwell time, which eventually decreases the image SNR. This can be partially compensated by increasing the excitation laser power, but it may result in excitation saturation and cause photodamage to the specimen [78, 79].

The second method used to enhance speed is to utilize two-photon wide-field imaging based on the technique of simultaneous spatial and temporal focusing of the femtosecond illumination pulses [80, 81]. The excitation beam is spatially separated into a “rainbow beam” and overlapped at the focal plane with its shortest duration, obtaining depth-resolved images. This method replaces a focus eliminating the need for lateral scanner to reach faster imaging speed. The drawback of this method is that the performance is often limited by the lower axial resolution compared with conventional multiphoton microscopy and sometimes lower SNR if the emission photons are highly scattered.

The third kind of method to improve imaging speed is to parallelize the multiphoton imaging process, which is commonly referred to as MMM. For MMM, the region on the specimen is scanned by multiple excitation foci simultaneously while each of them scans a sub-region, instead of a single excitation focus scanning the whole region point by point. And the emission light from all foci is collected together by a spatial-resolved detector, usually a charge coupled device (CCD) camera. Therefore, the imaging speed improvement is proportional to the number of foci. Multiple beamlets in this microscopy are generated by a microlens array [13], a beam splitter [82], diffractive optical element (DOE) [83] or a light modulator [84]. As introduced earlier, there is a much smaller cross-section than confocal processing since it is a low probability of occurrence for multiphoton events. A common way to compensate it is using large excitation intensities, but it is limited by photodamage and absorption saturation to tissue specimen in practice. With this method, MMM reaches a high imaging speed without the necessity to increase excitation power, thus avoiding the photon absorption saturation as well as reducing photo-toxicity. Moreover, presently available lasers in the market provide higher power beyond the need at the given point with the exception of application of imaging into high-scattered tissues. Using multiple foci could take full advantage of the exceeded power [41]. For typical Titanium:Sapphire (Ti:Sa) laser with several Watts of output, approximately one hundred foci can be effectively generated for tissue imaging resulting in about two orders of magnitude improvement in imaging speed. After the first MMM developed by Hell group (1998), there have been several generations of MMM improved by researchers that will be introduced in the next section. In the last few years, MMM has been applied to the 3D imaging of biological specimens, including living cells [85] and dynamic processes [86].

Compared to the first two methods discussed above, MMM is the more promising method for 3D high resolution imaging in liver fibrosis.

2.3.2 Different types of MMM

As mentioned above, one of the major thrusts to enhance multiphoton imaging speed is to use MMM by splitting single high-powered laser beam into multiple beamlets. Therefore, the two critical components in an MMM system are the generation of an array of focal points and the detection of the multiple foci.

Generation of an array of focal points

The first MMM setup originally designed for TPEF in 1998 uses a microlens array with a Nipkow-type arranged focal pattern [13]. This type of microscopy was also adapted to a setup of SHG multifocal microscopy [87]. In the setup, the 5×5 array of microlenses etched on a fused-silica disk is arranged with a constant helical pitch, forming spirals with typically 10 rows. The illuminating beam is split into beamlets after the microlens array, and focused into an array of approximately 5×5 foci at the prefocusing plane. The frame rate for this setup is as high as 225 frames/s, essentially limited by the readout time of the camera. A second report proposed to use a static microlens array and a pair of galvanometric scanners driven in a Lissajous pattern to avoid edge effects [88]. The studies mentioned above illustrate that MMM makes a much more efficient use of laser power and can reduce the image acquisition time from 1 s to 10-50 ms [89]. However, for this system, the uniformity of the multiple foci is limited to 50% and the transmission efficiency is only 25%.

An elegant method of creating multiple foci while simultaneously delaying consecutive beams is to employ beamsplitters which has found its way into commercial systems (TriM scope, LaVision BioTec, Goettingen, Germany) [82]. In this case, the beam profile is maintained for each beamlet and not relayed to the focal plane. A temporal delay of a few picoseconds is introduced between adjacent foci by the different optical path lengths that the beams have to travel within the beamsplitter system. Dividing the beam into virtually equally intense beamlets is imperative because each beamlet illuminates a different subfield. A significant advantage of the beamsplitter approach is that the relative spacing between focal points can be smoothly varied. However, a large fraction of the laser light is wasted to attain equal beamlet intensities. In addition, the tilting of the beamsplitters must be handled with particular care in order to obtain equidistant foci with each beamlet centered on the objective entrance pupil.

In the past few years, a high efficiency DOE has been utilized to create multiple foci [83]. In the first setup implemented with DOE, combined with two galvanometric scanners, TPEF images with a field of view of 100×100 μm^2 and a resolution of 512×512 pixels in approximately 100 ms are obtained. The DOE generates a 4×4 foci array with 25 µm separations between foci (using a 60 µm, 1.4 NA objective) with 75% diffraction efficiency. The use of DOE permits a very uniform (~99%) intensity distribution at the focal plane, which is in sharp contrast with microlens arrays that might have intensity fluctuations as high as 50% from their central part to their edges. In 2006, a DOE was used to produce a 10×10 hexagonal array of foci which was scanned using two galvanometric mirrors driven by white noise [90].

Detection of multiple foci

Similar to two-photon wide-field imaging, the SNR of multifocal multiphoton microscopy is also limited by the tissue scattering of emission compared with single focus scanning multiphoton microscopy. Simultaneous detection of multiple foci requires detector with spatial resolution that can distinguish signals from all the foci at the same time. All the schemes presented so far for MMM operate in one imaging modality and use conventional detectors, such as CCD or complementary metal–oxide–semiconductor (CMOS) cameras. However, when emission photons generated at one focus are scattered in a turbid specimen and arrive at detector pixels that do not map to the focus location, the SNR of the image suffers. One solution is to use a novel type of detector, namely, a multi-anode photomultiplier tubes (MAPMT) [12]. It is based on the same operating principle as a photomultiplier tube (PMT) except that it has 64 independent active areas arranged in an 8×8 matrix. This detector can be coupled into an

MMM with an $n \times n$ array of foci, $n = 1, 2, \dots, 8$. The main modification to a traditional MMM imaging setup is that, in order to have a one-to-one correspondence between foci and active areas on the MAPMT, it is necessary to de-scan the signals. The authors report 320×320 pixel images taken at 19 frames/s. The use of MAPMT in descanned detection geometry can compensate lower SNR. The larger detection area of each anode greatly reduces the crosstalk between foci due to the scattering of emission photons and significantly improves the image SNR.

Chapter 3

Objectives and Significance

3.1 Limitations of current work

In view of the previous review, multiphoton microscopy is a remarkable method to study changes of tissue morphology, collagen structure and distribution during both progression and regression of liver fibrosis. TPEF and SHG signals are able to provide 3D subcellular resolution information for hepatocytes and collagen in liver. Nevertheless, there are a few limitations in current studies:

- Present work on collagen by SHG imaging mostly focus on single mode detection for forward or backward SHG signals. But these two kinds of signals reflect different structures of collagen fibrils. Analysis based on single mode detection can only provide morphological information, while the ratio of forward to backward SHG reveals fibril size and packing.

- A large sampling size is very important for any quantitative analysis to draw significant conclusions. According to the present imaging speed of conventional multiphoton microscopy, however, it takes years to finish one lobe of mouse liver. Therefore, it is necessary to find a way to increase imaging speed.
- As an exceptional method, MMM is able to increase imaging speed by parallelizing multiphoton image processes. To achieve multifocal excitation and corresponding detection, there is a need to split a single beam into multiple beamlets with high uniformity in intensity over all beamlets with compact optical components and set up a detection system to acquire signals coming from multiple locations efficiently with high sensitivity. But previous studies focused on either multifocal generation or detection. No work has improved both of them in one setup so far.
- In addition to morphological information from TPEF signals, it is crucial to obtain collagen signals concurrently for liver fibrosis studies. However, none of the existing multifocal multiphoton microscopy was designed for this purpose.

3.2 Specific objectives and significance

The main aim of this study was to investigate the spatial distribution of collagen in liver during liver fibrosis progression process by using a MMM imaging system integrated with SHG. As mentioned in Section 2.3, MMM itself can be improved by utilizing a high-transmittance multifocal generator and a high-efficient detector. The specific objectives of this research were:

- To study the correlation of forward and backward SHG as well as their average intensity ratio in different liver fibrosis stages, and improve fibrosis staging by combining these features into one index.
- To design and construct a novel MMM system with 64-time faster imaging speed than conventional multiphoton microscopy. The system would consist of a multifocal generator with high transmittance and uniformity and a highly sensitive detector. Meanwhile, to integrate SHG as the second channel into MMM so that the whole imaging system is able to obtain TPEF and SHG signals synchronously.
- To characterize the new MMM-SHG system by measuring its specifications and to improve its performance for the study of liver

fibrosis by developing customized image post-processing method and implementing an automated slicing module.

The new imaging system should be able to image large volume of tissue or even the whole organ with 64-time faster speed over conventional multiphoton microscopy. The 3D high resolution images obtained could visualize cell morphology and collagen distribution as well as monitor the changes of both information during liver fibrosis progression in a spatial-dependent manner.

Chapter 4

Improving Liver Fibrosis Diagnosis Based on Forward and Backward SHG Signals

Collagen has been prevalently used to assess liver fibrosis stages by SHG microscopy in various studies. These studies mostly focus on single mode detection for forward or backward SHG signals. However, these two kinds of signals reflect different structures of collagen fibrils. Moreover, single mode detection can only provide morphological information, while the ratio of forward to backward SHG reveals fibril size and packing.

In this chapter, the correlation of forward and backward SHG as well as their intensity ratio in different liver fibrosis stages was investigated to validate that they are not only able to differentiate healthy and fibrotic liver, but also effectively stage liver fibrosis. Furthermore, an SVM classification algorithm was applied to combine these features into one index. A more significantly accurate prediction demonstrates that this method can be a promising tool for liver fibrosis diagnosis.

4.1 Introduction

Liver fibrosis is the consequence of a sustained wound-healing response to chronic hepatocellular damage and it may result in cirrhosis, liver failure, and portal hypertension [1]. Collagen accumulation is one of the most significant phenomena and diagnostic characteristics in liver fibrosis development.

Due to its noncentrosymmetric structure, collagen is able to produce an SHG signal, which is intrinsic and requires no fluorophores presence in tissue. Therefore, SHG microscopy has been used for collagen quantification as an indicator of fibrosis progression [58-60, 91, 92], especially in liver [11, 65, 93]. However, most studies have only focused on the use of forward SHG signal to diagnose liver fibrosis.

Recently, it has been recognized that forward and backward SHG signals are generated simultaneously, and different morphological features of collagen fibrils have been extracted in forward SHG and backward SHG images [94]. For example, researchers studied and confirmed that the ratio of forward SHG to backward SHG signals arises from fibril size and packing. This concept has been used to differentiate healthy and diseased tissues in osteogenesis imperfect (OI) [95], ovarian cancer [96] and breast cancer [97]. Therefore, the combination of forward and backward SHG signals may provide in tandem complementary information about collagen and provide a new means to improve liver fibrosis diagnosis.

Here, our primary goal is to investigate the feasibility of using the combination of forward and backward SHG signals for improving liver fibrosis diagnosis in a well-established disease model [98]. In this work, we not only validated feasibility of differentiating normal and fibrotic liver tissues from forward SHG, backward SHG and their average intensity ratio, but also quantitatively monitored the evolution of collagen through the whole liver fibrosis progression by comparing with morphological staging performed by pathologists which is considered to be the existing gold standard for liver fibrosis diagnosis [99, 100]. Furthermore, an SVM algorithm was performed to effectively improve the diagnostic accuracy at different fibrosis stages based on the combination of all extracted features.

4.2 Materials and methods

4.2.1 Preparation of animal model and tissue samples

All animal-related experimental procedures were carried out in conformity with the laboratory animal protocol approved by the Institutional Animal Care and Use Committee (IACUC). Male Wistar rats at an average weight of 220 g were used to establish the TAA-induced liver fibrosis model. Two rats were housed in each cage in the Biological Resource Centre (BRC) of Biopolis, A*STAR with free access to laboratory chow and water in a 12:12h light/dark schedule. TAA was administrated into the rats through intra-peritoneal injection (ip.) with 200 mg/kg of body weight with Phosphate Buffer Solution (PBS), three times a week for 14 weeks. Rats were sacrificed at week 0 (control), 2, 4, 6, 8, 10, 12, 14 after liver fibrosis induction. Liver tissues were extracted, paraffinized and sectioned with a thickness of 5 µm and 50 µm for staining and SHG imaging respectively.

4.2.2 Histo-pathological scoring

5 µm tissue slices were stained with a MT stain kit (Chroma View advanced testing, no. 87019, Richard-Allan Scientific, Thermo Fisher Scientific, Wathan, Massachusetts) and imaged with bright-field

microscopy (Aperio Digital pathology Environment) for comparison with SHG images. Each sample was scored by a pathologist based on blind reading to reduce any bias using Metavir score [27]. In the Metavir scoring system, liver fibrosis was classified into five stages from F0 to F4 according to the severity of fibrosis: no fibrosis, fibrous portal expansion, few bridges or septa, numerous bridges or septa, and cirrhosis.

4.2.3 Experimental setup of nonlinear optical microscopy

50 µm tissue samples from 5 rats in each scored stage were used for SHG imaging. The nonlinear optical system, shown in Figure 4.1, was developed based on a confocal imaging system (LSM 510, Carl Zeiss, Heidelberg, Germany) as described in our previous work [66, 101]. The excitation light comes from a femtosecond mode-lock Ti:Sa laser (Mai-Tai broadband, Spectra-Physics) tuned to 900 nm, passing through a pulse compressor (Femtocontrol, APE GmbH, Berlin, Germany) and an acousto-optic modulator (AOM) for group velocity dispersion (GVD) compensation and power attenuation respectively. An oil immersion objective with NA 1.3 (Carl Zeiss: EC Plan-Neofluar, 40×) was used for microscopic imaging. The beam focuses on specimen after being reflected by a dichroic mirror (KP 650) that deflects laser light longer

than 650 nm and allows transmission of light shorter than 650 nm. There are two tracks to detect reflected TPEF signal in track 1, transmitted forward SHG and reflected backward SHG signal in track 2 respectively. TPEF signal was collected by the same objective lens, reflected by a mirror and filtered by a 500-550 nm band-pass filter to an identical PMT as transmission mode. The mirror was taken off to switch on track 2. Backward SHG signal simultaneously generated in tissue was reflected by another mirror and recorded by a spectral detector that includes 32-spectral channels and allows spectral detection between 430-750 nm. Emission beam at 450±10 nm was recorded by the spectral system. Forward SHG was collected by a condenser (NA=0.55) in transmission mode and filtered by a 450±10 nm band-pass filter. A short-pass filter (BG39) was placed in front of PMT to block infra-red (IR) light. Settings for both channels were kept the same for all images through the whole experiment. In each scored stage, 20 images per sample were acquired and each one has 225×225 μm^2 field of view with 1024×1024 pixels. A fine focusing stage (HRZ 200 stage, Carl Zeiss) was used to change and record the focus position and to translate the samples after x-y scan. The depth of 0 µm refers to the tissue surface where the signal of reflection from the interface between the tissue and the glass coverslip reaches to maximum.

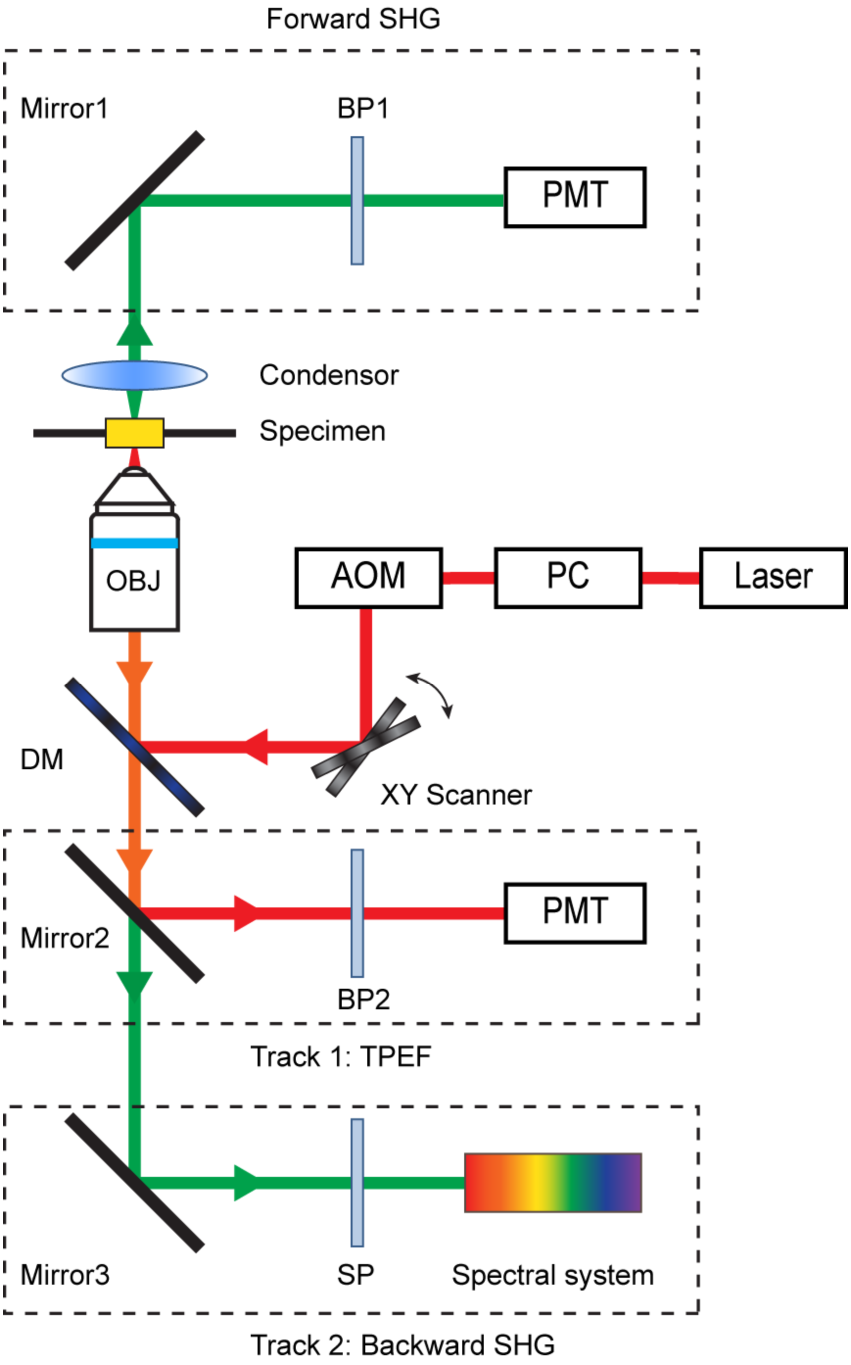

Figure 4.1 Schematic illustration of nonlinear optical system configuration: Excitation laser was a tunable mode-lock Ti:Sa laser (710 to 990 nm set at 900 nm) with a pulse compressor and an acousto-optic modulator (AOM) for power control. The laser passed through a dichroic mirror (DM), an oil-immersion objective lens (40×, NA=1.3) before reaching tissue specimen on an automatic X-Y stage. Forward SHG signal was collected by a condenser (NA=0.55), through a field diaphragm, and a 440-460 nm band-pass filter (BP1) to a PMT. For reflection mode track 1, TPEF signal was collected by the same objective lens, filtered by a 500-550 nm BP2 to another PMT; In track 2, mirror2 was taken off so that backward SHG signal was reflected by mirror3 and filtered by a short-pass filter (SP) before being recorded by a spectral system.

4.2.4 Image acquisition and segmentation

To accurately extract collagen information from SHG images, especially the presence of collagen in the liver organ, the reduction of a gray-level image to a binary image is required. In this study, three different methods for segmenting collagen fibrils were utilized. They are based on Otsu thresholding method [102], K-means clustering [103] and Gaussian mixture model (GMM) [104]. For all of these segmentation processes, a binary image was obtained with separated collagen area (pixel value set as 1) and background (pixel value set as 0) after corresponding computation algorithm.

Otsu method is a classic global thresholding algorithm, which aims to find the best threshold to minimize intra-class variance and maximize the between-class variance, which is defined as

$$\sigma_{\omega}^{2}(t)=\omega_{1}(t)\sigma_{1}^{2}(t)+\omega_{2}(t)\sigma_{2}^{2}(t), \tag{4.1}$$

where weights ω_i are the probabilities of the two classes separated by a threshold t and σ_i^2 variances of these classes. The desired threshold is computed from the maximum σ_i^2.

K-means clustering is one of the most popular and iterative clustering methods for image classification, which aims to partition n

observations into k clusters in which each observation belongs to the cluster with the nearest mean. The segmentation target is to separate collagen signals from the background so that k is set to 2 in our study (one is for the collagen signals and the other is for the background). The distances between every pixel to each cluster mean were calculated and the nearer cluster was chosen. Then cluster centers were re-computed by averaging all confirmed pixels until convergence was reached. This process could be generally expressed by

$$\arg\min_{S} \sum_{i=1}^{k} \sum_{x_j \in S_i} \left\| x_j - \mu_i \right\|^2 \tag{4.2}$$

where x_j belongs to a given set of observations ($x_1, x_2, \ldots, x_n$), S_i is the within-cluster sum of squares that needs to be minimized.

The GMM-based method is based on the assumption that the distribution of intensities is a mixture of several Gaussian distributions, each corresponding to a separate tissue class. In an SHG image, the intensity of pixels is modeled as the mixture of two Gaussian distributions, one representing collagen area with strong SHG signals and the other representing the background. The Gaussian distribution parameters were estimated by Expectation-Maximization algorithm [104].

A typical SHG image (3072×3072 pixels, ~$1.38\times1.38\ \mathrm{mm}^2$) was applied by all above segmentation methods for comparison. Figure 4.2 shows the binary images generated from Otsu thresholding method (b), K-means clustering (c) and GMM (d). As shown in the results, all the three algorithms are able to segment most of the thick collagen fibers around blood vessels. Compared to Otsu thresholding method and K-means clustering, GMM can achieve better segmentation result by picking up dimmer and finer collagen fibers while incurring minimal noise in the image. The binary image from GMM segmentation can not only show more obvious collagen feature around vessels (hole in the center and bottom right corner), but also reveal clearer bridging between the vessels. This result is coincident to collagen distribution in fibrotic stage. Therefore, it can be concluded that GMM is a better segmentation method to extract collagen fibers and this is the same with previous studies [105]. GMM method has been chosen to segment all SHG images in this work.

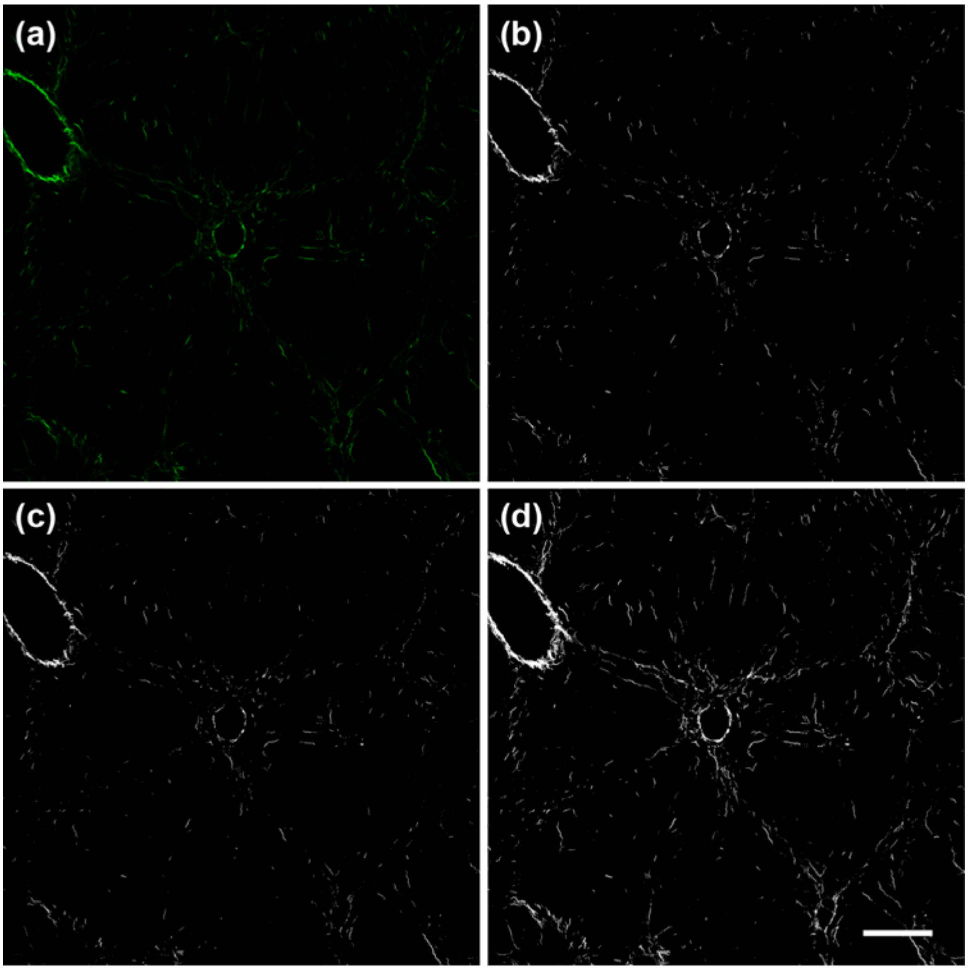

Figure 4.2 Images of fibrotic rat liver tissue from forward SHG (false color as green) modality (3072×3072 pixels) (a) and segmented by three different algorithms based on Otsu thresholding method (b), K-means clustering (c) and Gaussian mixture model (d). Scale bar: 200 µm.

4.3 Results and discussions

4.3.1 Validation of TPEF/SHG images for studying liver fibrosis

Figure 4.3 shows images of a section of control rat liver tissue from TPEF channel (a), forward SHG channel (b) and backward SHG channel (c) respectively. In the tile scan image (3072×3072 pixels,

1.38×1.38 mm^2), signals from TPEF and two SHG modalities are perfectly overlapped to reveal the hepatic architecture (Figure 4.3(d)). Cells, shown as light blue color, connect tightly to each other and sinusoids form between hepatocytes lines. Black dots inside cells represent nuclei. Blood vessels are clearly visible as black holes in hepatic parenchyma. The veins pointed by white arrows in Figure 4.3(c) and (d) are believed to be portal tracts because they are obviously three gathered vessels, i.e. hepatic artery, portal vein and bile duct. The larger hole on the right does not mean the vein is actually larger than the other two. It is caused by sectioning when there is a small angle between cutting direction and the vein. Correctly matching standard morphological structure of liver tissue, thick collagen fibers (shown as red color in Figure 4.3(a) and green color in Figure 4.3(b)) are around blood vessels; while thin collagen fibers are along hepatocytes. The result proves that two-photon microscopy is able to acquire TPEF signal for hepatocytes and SHG signal for collagen synchronously. The two kinds of signals are well colocalized and provide subcellular resolution information to spatially display hepatic architecture without staining. In particular, both forward and backward SHG signals are proved to be able to reveal distribution and morphology of collagen fibrils. This provides strong support to further study fibrosis staging based on collagen characteristics from forward and backward SHG.

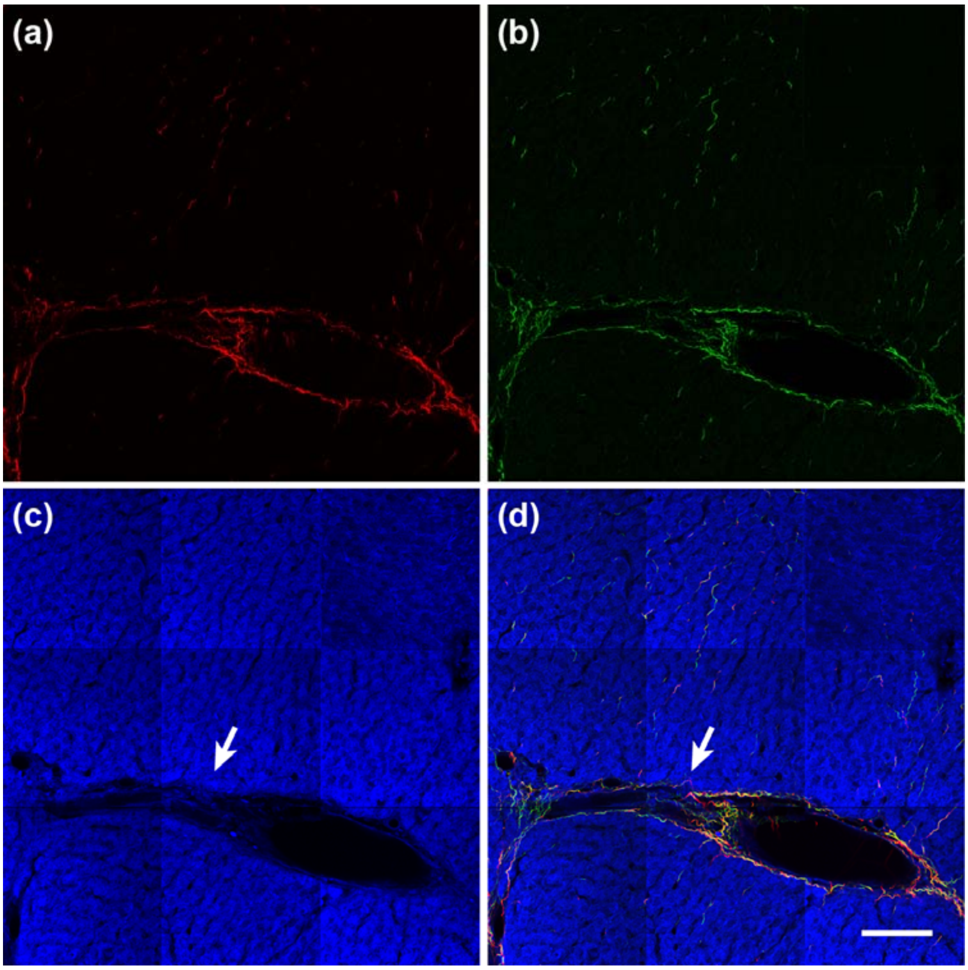

Figure 4.3 Images of rat liver tissue in control group from forward SHG channel (a), backward SHG channel (b), TPEF channel (c). All images (3072×3072 pixels) were taken from 50 μm paraffin embedded section tissue slice. Detailed overlay image (d) showed that signals from TPEF (false color as blue) and two SHG (false color of forward SHG as red, false color of backward SHG as green) modalities are perfectly overlapped to reveal the hepatic architecture that thick collagen around blood vessels and fine collagen fibrils along hepatocytes. Scale bar: 100 μm.

4.3.2 Comparison and quantification of forward and backward SHG images among different fibrosis stages

Morphology of collagen fibers at different pathological fibrosis stages were visualized by the nonlinear optical system from both forward and backward aspects of SHG signals. Figure 4.4 shows selected images that reflect typical characteristics of collagen accumulation in the tissue with the development of liver fibrosis. The collagen distribution in images from forward SHG (first column in red color) and backward SHG (second column in green color) are similar. Signals from both of the modalities are able to present fine collagen fibrils in high resolution. In stage 0 (Metavir score F0, first row in Figure 4.4) and stage 1 (F1, second row), collagen mainly locates around portal tracts and central veins as thin circles. More collagen is generated at vessel area that obviously makes the circles thicker in stage 2 (F2, third row). Besides the thickness, more and more fine collagen fibrils are produced and formed a thin net in the tissue surrounding vessels for stage 3 (F3, forth row). Some fibrils extend out to another vessel area, as shown by white arrows. In the last stage, i.e. stage 4 (F4, last row), much more collagen extends until it links with collagen from other vessels and gets much thicker, forming broad septa between portal areas, and between portal areas and central veins. This phenomenon is a key criterion for late stage fibrosis assessment in various score systems [28, 29, 106-108]. Therefore, it is obvious that clear changes of collagen deposition during fibrotic progression can be recorded by both forward SHG and backward SHG images from nonlinear optical approach without any staining and correctly reflect different phases of fibrotic progression.

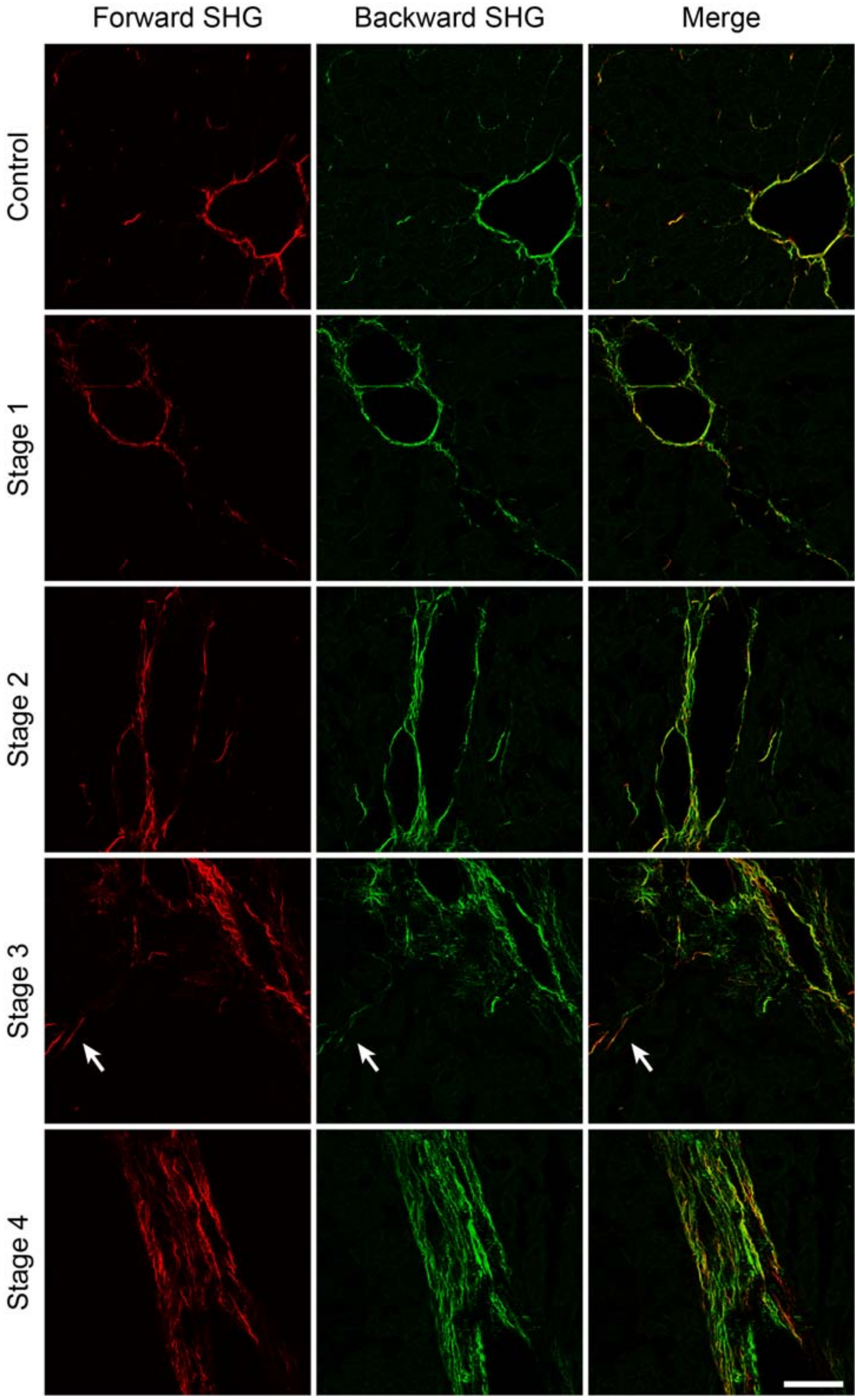

Figure 4.4 Forward and backward SHG signals from collagen at different liver fibrosis stages. Both forward SHG signals (first column, false color as red) and backward SHG signals (second column, false color as green) showed significantly increment of collagen deposition with the development of fibrosis from control (first row) to late stages (row 2-5 corresponds to stage 1-4 respectively). Merged images (third column) indicated the perfect overlay of forward and backward SHG signals. Scale bar is 50 µm.

Quantification is required for diagnostic purpose, especially for fibrosis staging. To accurately extract collagen information from SHG images, GMM-based segmentation method is utilized. This method was shown to be more accurate than other methods such as global thresholding and clustering methods, as discussed in Section 4.2.4. After segmentation, final masks were created on both raw forward and backward SHG images to present collagen content in the tissue samples. The segmentation results of forward SHG, backward SHG and the overlap area are shown in Figure 4.5(A). Figure 4.5(A)(a)(b) are images of fibrotic liver tissue in stage 2 (1024×1024 pixels, ~225×225 μm^2) from forward SHG channel, backward SHG channel respectively. Their corresponding segmentation images are shown in Figure 4.5(A)(d)(e). Collagen distributions were completely preserved in the segmentation, even very fine fibrils.

From the segmentation images, collagen area percentage can be calculated through dividing the number of pixels that belongs to collagen by total area of an image. Figure 4.5(B) indicates that total collagen area percentage increases significantly with the natural progression of liver fibrosis and evidently reflects different stages based on histo-pathological results. The collagen area percentage from forward SHG channel and backward SHG channel are at highly similar level in stage 0 to stage 2. From stage 3, collagen area percentage from backward SHG channel gets higher than forward SHG channel. A plausible explanation is the septa structure have started forming so that more scattering light were generated backwardly instead of penetrating forwardly. Therefore, the quantitative result shows capability of both forward and backward SHG of collagen for liver fibrosis staging and this is in good agreement with previous experiments.

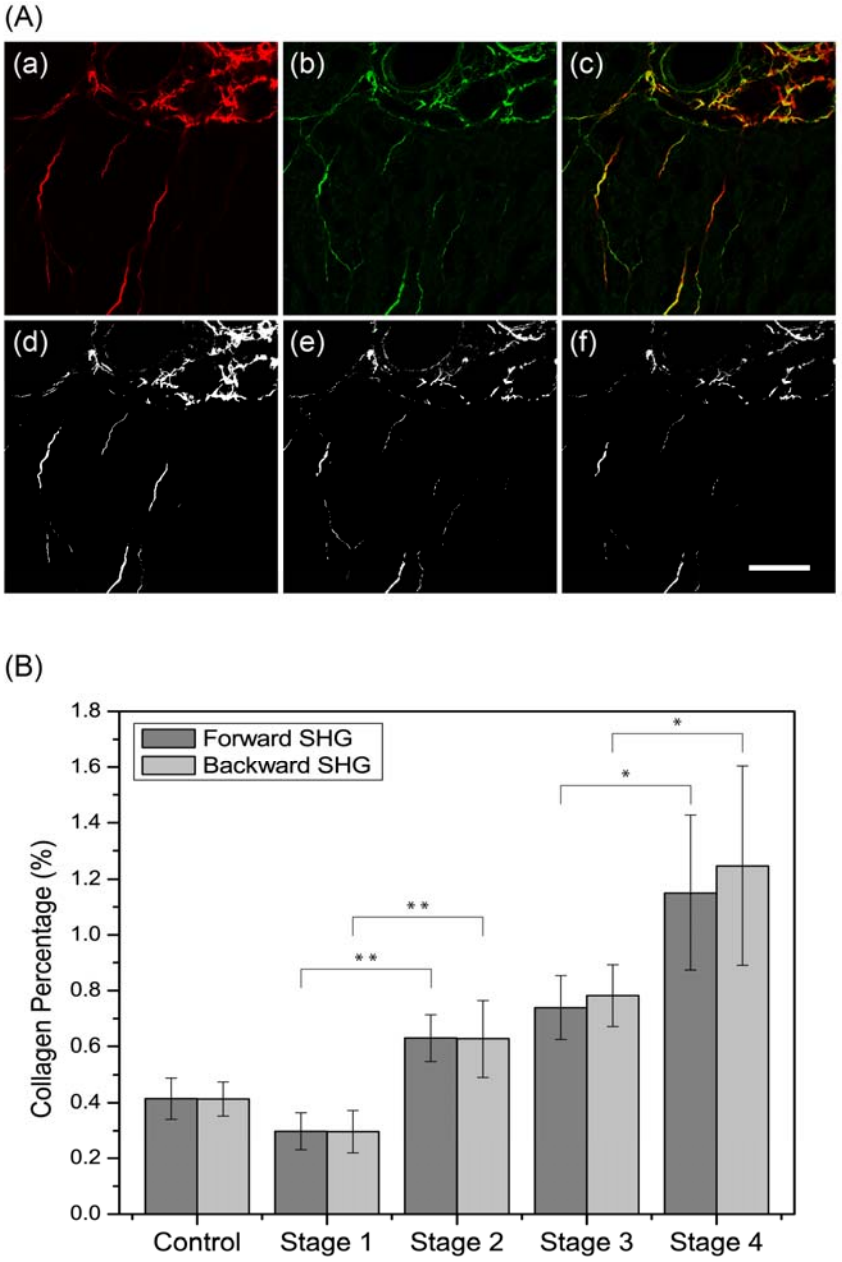

Figure 4.5 Quantification of liver fibrosis progression from areas of collagen detected by nonlinear microscopy. (A) Segmentation algorithm based on Gaussian Mix Model was applied on original forward SHG (a) and backward SHG (b) images. The segmentation results of both forward (d) and backward (e) SHG images are able to preserve collagen distribution and morphology. Even though the signals from two channels were highly colocalized (c), a limited area was exactly overlapped (f). (B) Collagen area percentage quantified from forward and backward SHG images respectively and they are significantly increased with the fibrosis progression. Comparison between two adjacent stages is performed with student's t-test. Significant differences (*p<0.05, **p<0.01) exist between stage 1 vs. stage 2 and stage 3 vs. stage 4. There are no significant differences between normal vs. stage 1 and stage 2 vs. stage 3 (p>0.05). Error bars represent standard deviation (SD).

4.3.3 Ratio of forward to backward SHG in different fibrotic stages

The segmentation masks from forward and backward SHG channels were cross-compared and their overlap area was extracted, shown in Figure 4.5(A)(f). This information corresponds to the orange color in the original image with merged channels (Figure 4.5(A)(c)). The result indicates that collagen fibrils in forward and backward SHG images are not completely colocalized even though their final collagen area percentages are at highly similar levels for all stages. The difference is due to the coherent nature of SHG that it has a phase (and spatial) relationship with the laser excitation. This characteristic underlies the observed contrast in the forward and backward modes and provides a great more information about the structure of the collagen fibrils. Combining these two kinds of signals would possibly reveal the evolution of fibrillar collagen during fibrosis progression and further contribute to liver fibrosis diagnosis. Thus, the signal intensity ratios of forward SHG to backward SHG at different stages were studied. All images were grey scaled and saturated pixels were removed to make sure every pixel counted is able to truly reflect intensity level. Figure 4.6(A) shows images of fibrotic liver tissue in stage 3 in original mode (a) and after grey-scaled for forward SHG channel (b) and backward

SHG channel (c) respectively. The signal intensities from the two channels are clearly dissimilar to each other. Based on the grey-scaled images, average intensities of all the pixels within collagen masks that obtained in section 4.3.2 were calculated. Figure 4.6(B) shows the ratio of average intensity of forward SHG to backward SHG acquired in same location. It illustrates that the intensity ratio decreases with the development of fibrotic status. The decrement can be adequately explained that a greater portion of collagen in late stages form septa which results in more backward light scattering, while less forward light is collected accordingly. Unlike the general results in the literature, the forward SHG signal is smaller than backward SHG signal. Three main factors, we believe, contribute to this result. First, as the chosen focal plane is close to the surface of tissue (2 μm), there will be a higher probability of multiple scatterings along the direction of forward SHG instead of the direction of backward SHG. Therefore, the ratio of forward SHG to backward SHG will be less than 1 and subsequently increases if we focus deeper into the specimen [95, 109]. Second, the objective lens for backward SHG detection and the condenser for forward SHG detection have different NA. The collection angle of forward channel is smaller than that of backward channel. Third, the signal attenuations of forward and backward SHG are different due to different optical paths. It is important not to overlook that stage 1 and control group can be significantly differentiated from intensity ratio result when it is not clear from collagen area percentage result. Hence, average intensity ratio of forward to backward SHG is able to provide complementary information onto traditional analysis of collagen area percentage.

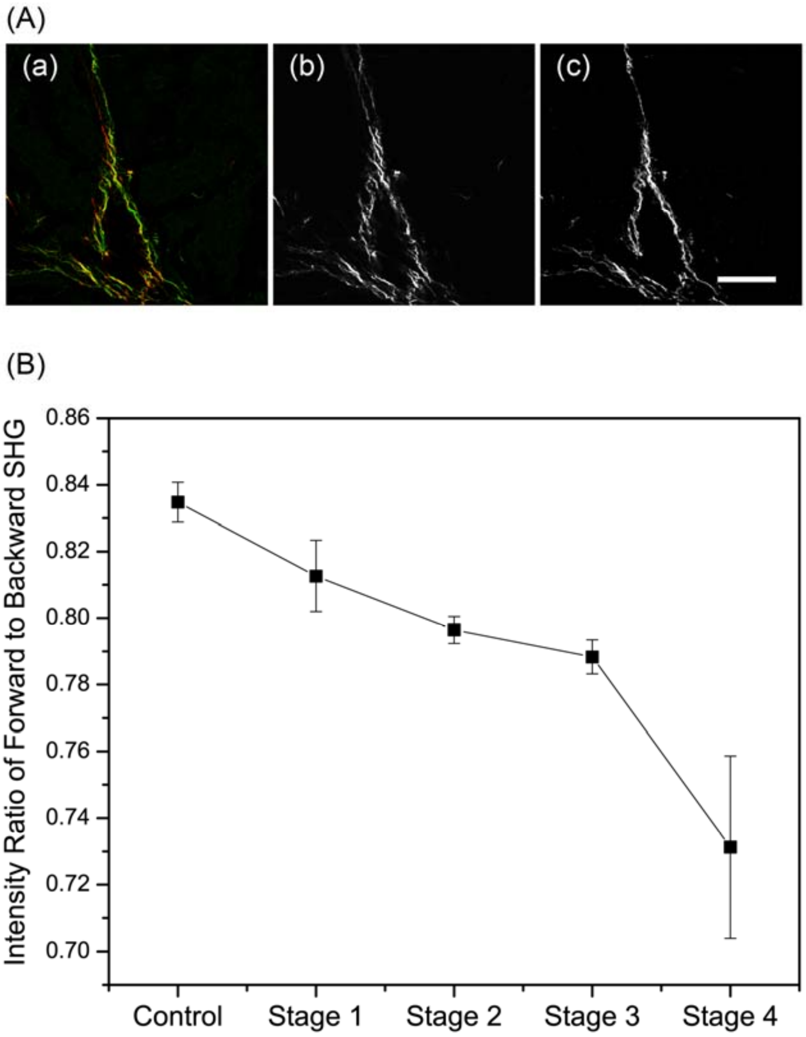

Figure 4.6 Quantification of average intensity ratio of forward and backward SHG signals. (A) Gray scaled forward SHG image (b) and backward SHG image (c) from original images (a). (B) Quantitative results from gray scaled images on average intensity ratio of forward and backward SHG signals at different fibrosis stages. Error bars represent SD.

4.3.4 Extent of liver fibrosis progression by combined features

All the above results validate that the three quantitative assessments (forward SHG collagen area percentage, backward SHG collagen area percentage, average intensity ratio of forward SHG to backward SHG) are not only able to identify different fibrosis stages base on histopathological scores, but also assist each other with complimentary information. In another word, they describe the event from different aspects and are limited to be a reliable index for liver fibrosis diagnosis alone. It is expected that the combination of all these features would provide more complementary information and improve the accuracy of the diagnosis. Therefore, a support vector machine (SVM) classification method was chosen due to its advantage of classifying data measured from multiple signal sources (multivariate data) with relatively small sample sizes [110]. SVMs are supervised learning models in machine learning to analyze data with the purpose of separating them into different groups with a clear and widest gap. In this process, all data are set as points distributed in space. Even though SVMs are good at performing both linear and nonlinear classifications, they are especially competent in nonlinear ones which are suitable for multiple inputs. In this case, we used a pre-computed nonlinear SVM algorithm that is a radial basis function Kernel in LIBSVM (V3.17) [111] to classify the samples based on all the above three quantitative features. 10-fold cross-validation was utilized so that all samples were used for both training and validation to enhance the prediction accuracy. Receiver operating characteristic (ROC) curves of collagen percentage in forward SHG (blue), in backward SHG (green), intensity ratio of forward SHG to backward SHG (brown) and SVM classification results (red) were drawn according to different fibrosis stages (Figure 4.7). It is clear that SVM results show a better prediction on fibrosis staging, especially in late stages. It means the combination of three features by SVM classification algorithm significantly improved fibrosis diagnosis compared to quantification of each feature alone. Specifically, the area under ROC curve (AUC) values of SVM results are 0.762, 0.842, 0.857 and 0.851 for distinguishing each adjacent stage, respectively.

Overall, we can quantitatively monitor the fibrosis progression in time based on the three features extracted. And each feature can be used separately as the clear indicator of the disease progression.

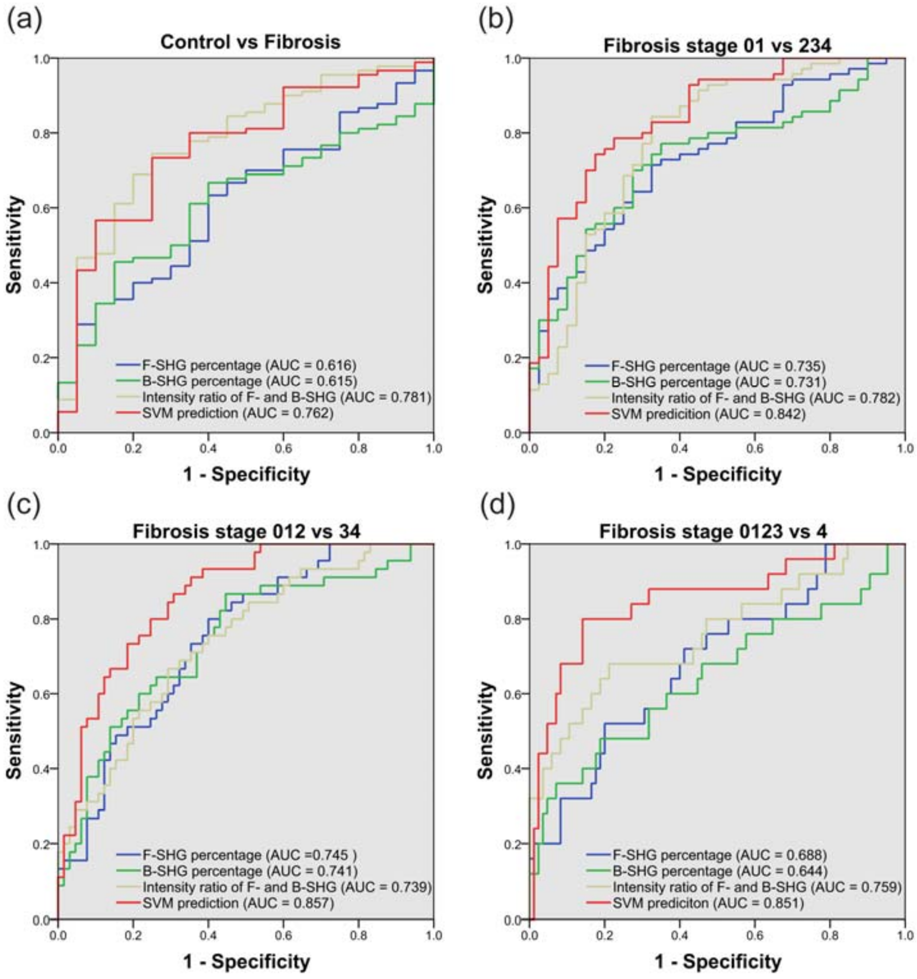

Figure 4.7 Comparison of fibrosis staging differentiation ability by receiver operating characteristics (ROC) curves of collagen area percentage from forward SHG signals (blue), collagen area percentage from backward SHG signals (green), average intensity ratio of forward and backward SHG signals (brown) and SVM algorithm to combine the above three features (red).

4.4 Conclusions

In summary, the present chapter validated the feasibility of a novel quantitative method by combining forward and backward SHG signals from collagen for liver fibrosis staging. This method integrated three quantitative assessments, including collagen content percentage of forward SHG and backward SHG as well as average intensity ratio of forward to backward SHG signals. The combined results showed a more significant classification capability that would enhance accuracy of liver fibrosis diagnosis in each stage. Since the three features are acquired in one-time scanning, further imaging and more processing procedures are not required. Thus, this method renders a promising tool for diagnosis of liver fibrosis development in different stages more accurately.

Chapter 5

Design and Construction of Dual Channel Multifocal Multiphoton Microscopy (MMM)

Quantitative results are very important but hard to achieve due to small sampling size resulted from limited imaging speed by conventional multiphoton microscopy. To enhance the imaging speed for liver fibrosis study, we have built an integrated MMM and SHG system by parallelizing the normal multiphoton imaging process with multiple foci. The system utilizes a highly transmitting and uniform DOE to generate an 8×8 array of foci and an MAPMT for detection, so that the imaging speed is 64 times faster than normal multiphoton microscopy. The new high speed imaging system can be used for large volume tissue imaging and 3D reconstruction.

This chapter recounts on the ground development of the MMM prototype system from optical, electrical and software aspects. Basic performance tests for DOE will be conducted after a brief description of the system optical pathway. Individual parts of electronics will be introduced and subsequently followed by software description.

5.1 Introduction

In Chapter 4, it is proven that liver fibrosis is able to be staged by quantifying SHG images for collagen content percentage after segmentation, or average intensity ratio of forward to backward SHG signals, or combining all above information with SVM algorithm from SHG images. This method could be a promising tool for diagnosis and monitoring fibrosis progression as well as regression, and it has been applied on our various projects. For instance, we used the quantification of collagen content percentage to study dimethylnitrosamine (DMN)-induced liver fibrosis regression through gene therapy.

In this project, hepatocyte growth factor (HGF) gene was specifically delivered to activated HSCs in fibrotic liver using vitamin A–coupled liposomes by retrograde intrabiliary infusion to bypass capillarized hepatic sinusoids to validate the hypothesis that targeted delivery of HGF transgene enhances regression of DMN-induced acute liver disease. Male Wistar rats (250 g) were administered 1% DMN through ip. for 3 consecutive days each week for 3 weeks to establish liver fibrosis and then not administering DMN for the next 7 days. Liposomes with pDsRed2-HGF plasmid DNA were administered for gene delivery [112]. All animal procedures were humanely carried out under the premises of the IACUC protocol (090492) approved by BRC, Biopolis, Singapore. Three groups of rat liver samples were collected for comparison: 1) Control (healthy control); 2) DMN (disease control); 3) Vitamin A + HGF (treatment group).

Two-photon microscopy was used to monitor and quantify the regression of the DMN-induced liver fibrosis with gene delivery treatment. The experimental setup was the same as described in Section 4.2.3. TPEF and forward SHG signals were collected and analyzed for this study. 10 locations were randomly picked from each animal sample and conducted single scan. Each image was 1024×1024 pixels, 450×450 μm^2 (Figure 5.1(a)). From the result shown in Figure 5.1(c), collagen percentages of healthy control and disease control match the experimental prediction that healthy control group shows the lowest fibrotic level; DMN group has much higher fibrotic level. However, the collagen percentage of treatment group, which is supposed to be the second lowest in all, is the highest in the end. And this result does not match with the other fibrotic markers test, such as TGF-β1. This might be due to three reasons: 1) Sampling size for scanning is not enough; 2) Collagen degradation is slower than biomarkers, namely a longer time point needs to be observed; 3) Collagen percentage is not a good fibrosis marker for this animal model. To ascertain the main reason, we first enlarged the sampling size by conducting two 9×9 tile scan (Figure 5.1(b)) for each animal so that the sampling size was enlarged from 10 to 162. The quantification from the tile scan shows a different result that treatment group has lower fibrotic level, which is consistent with the other biomarker tests. It illustrates that the sampling size with single scan at 10 random locations is not large enough to provide quantitative information. The larger sampling size is, the more accurate quantification result can be achieved. Nevertheless, it is very time consuming to scan for large sample areas. It takes more than an hour just for a two-dimensional (2D) scanning of 9×9 tile area. And that is only 1/16000 namely 0.0625% of one lobe of the liver. According to this, the quantification result may be even more different for a liver lobe whose scanning would require 130 days using conventional multiphoton microscopy. Therefore, a high-speed imaging method is necessary to pursue quantitative results.

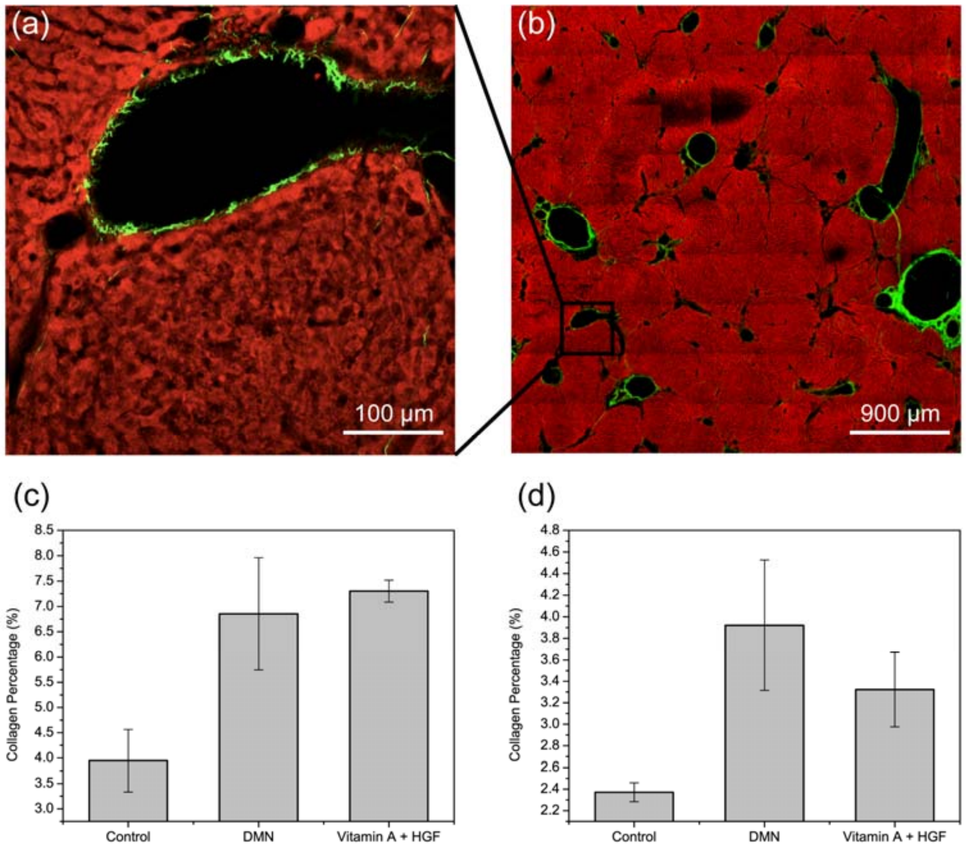

Figure 5.1 Quantification of collagen percentage from different sampling sizes in gene delivery study. For ten random single scans (1024×1024 pixels, 450×450 µm^2) per sample (a), treatment group (Vitamin A + HGF) has higher collagen percentage than disease group (DMN)(c); While for two 9×9 tile scans (9216×9216 pixels, 4050×4050 µm^2) per sample (b), treatment group has lower collagen content which is in agreement with hypothesis and other fibrotic marker tests (d).

As introduced earlier in Chapter 2, there are mainly three approaches to enhance multiphoton imaging speed. The first approach is using high-speed scanners such as polygonal mirrors [72] or AODs [74, 76, 77] instead of conventional galvanometric mirror scanners. The second way is using wide-field imaging [80, 81]. However, both of the methods sacrifice image resolution, image contrast and high SNR. Therefore, MMM is the ideal choice at this stage. This method is an intermediate approach between the other two techniques by parallelizing the normal multiphoton imaging process. The single beam in conventional multiphoton microscopy is separated into multiple beamlets so that a number of foci are scanning the specimen simultaneously. The whole scanning size at specimen is the sum of the sub-region scanned by each focus. Hence, the imaging speed is enhanced proportionally to the sum of the number of foci.

5.2 System overview

The whole MMM imaging system is mainly composed of laser, optics, microscope, electronics and software as a set of complete operation of scanning and signal acquisition under software control.

The schematic of the whole system is shown in Figure 5.2. The excitation beam comes from a Ti:Sa mode-locked laser. To obtain fast scan, a DOE is utilized for separating one beam into 64 beamlets to parallelize the conventional multiphoton imaging process. 64 beamlets in an 8×8 array are focused on specimen by an objective lens that is attached on an upright microscope. By controlling a 2D scanning mirror set, a square area on specimen is scanned pixel by pixel. The emission light goes back along the same optical path. Signals are separated into two channels by a dichroic mirror and recorded by two MAPMTs, each of them has 64 detection areas for corresponding beamlets. For each channel, light signals are converted into electrical signals, modulated by discriminators and sent to Xilinx field-programmable gate array (FPGA) board. The Xilinx FPGA board is a signal control center that not only transfers signals into computer, but also received commands from computer to control scanning mirrors. Software with friendly interface is installed in computers for configuration, control and display scanned images.

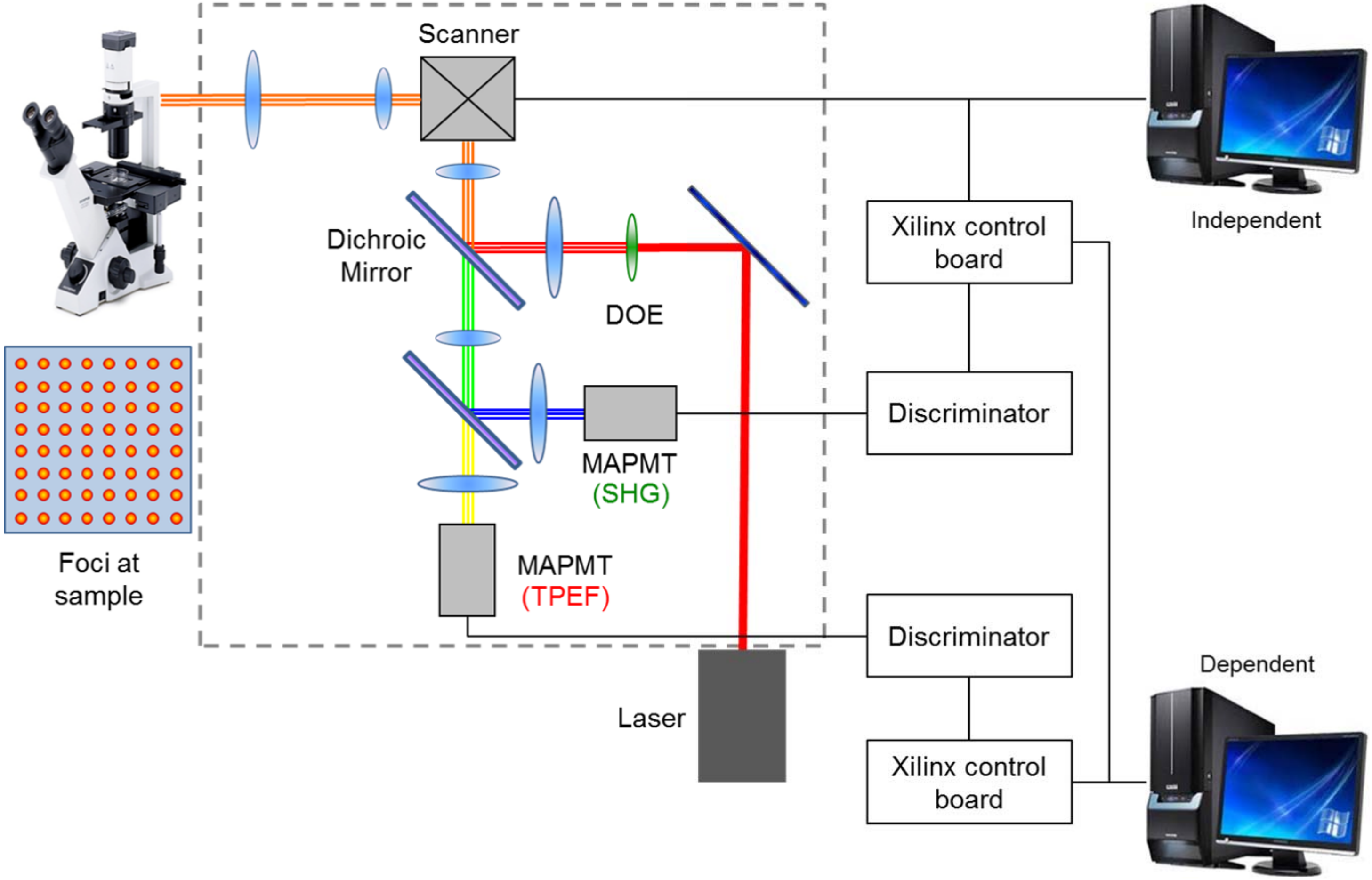

Figure 5.2 Overview of the whole new MMM imaging system, including laser, optical path, microscope, electronics and computers.

5.3 Optics in MMM system

5.3.1 Laser

There is a limit to the number of foci as we need to make sure each foci has enough power to excite tissue specimen. Owing to the wavelength tunability, short pulse length and high repetition rate, mode-locked Ti:Sa lasers have become the light sources of choice for multiphoton microscopy. Mode-locked Ti:Sa and similar laser systems typically provide 1 to 2 W of average power at a repetition rate of 80 MHz at pulse lengths of 200 fs or 1 to 2 ps. For our system, an 8×8 array of foci is generated by DOE. To get enough signals, the power for each foci should be at least 25 mW. Assuming the transmittance of all the other optical lenses is 80% and DOE is 70% (from factory datasheet), the power needed for the whole system with 64 foci is at least 2.86 W. Therefore, we choose Coherent Chameleon Ultra II laser whose peak average power is more than 3.3 W.

5.3.2 Factors influencing optical design

There are a few optical parts that are necessary in a normal microscopy, such as scanning mirror, scan lens, tube lens, dichroic mirror, objective lens and detector. Beside those, additional lenses would be added into the optical path to adjust beam size. In general, the space between a pair of achromatic doublet lenses can be of any distance since the beam is collimated (shown in Figure 5.3). In our system, however, DOE is placed in between a pair of achromatic doublet lenses so that the beam array is divergent when each beamlet is collimated. Therefore the distance between the pair of achromatic doublet lenses should be fixed to decide the beam array size.

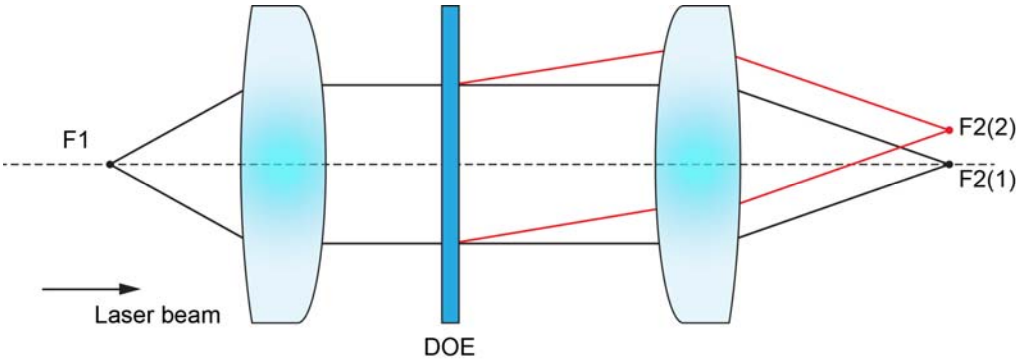

Figure 5.3 Beam path by a pair of achromatic doublet lenses. DOE is placed between the lens pair; hence the distance of the lens pair decides the separation of multiple foci.

The following conditions of beam size need to be satisfied due to practical situation in optical design.

1) The beam should be focused at scanning mirror and its diameter need to be ≤3 mm due to mirror size (6 mm each);
2) The beam diameter at any lens shall not be larger than 2 inch. Firstly, all commercial lenses in the market are ≤2 inch. Any larger size lens need to be customized manufactured and its quality is hard

to be guaranteed. Secondly, significant aberration will be generated if large area beyond the lens center is illuminated.

3) The back aperture of objective lens theoretically needs to be fulfilled, and in our case its dimension is approximately 20 mm. However, final beam dimension is decided by considering both of back aperture size and its optical transmittance to ensure enough light power to the sample. This will be discussed in the next session.

5.3.3 Optimal beam size at back aperture of objective lens

Generally speaking, laser beam should fulfill the back aperture of objective lens to maximize the field of view within effective area. However, it is found through our experiments that there is a large fraction of power loss when light goes through objective lens and the loss percentage might change with the beam size. Therefore, it is required to choose a beam size that can balance field of view and power loss.

To decide an optimal beam size, an experiment was performed to calculate objective transmittance with a series of incident beam size from 5 mm to 20 mm that is nearly the back aperture of the objective lens. Light power was measured by a power meter before and after the objective lens. Figure 5.4 shows the results. A sharp drop of power transmittance starts from 13 mm. There is only 50% of power left if the back aperture is fulfilled, and with this power, biological tissues are not able to be sufficiently excited. Hence, we decided to choose 11 mm as the beam size where the power transmittance is 82.5%.

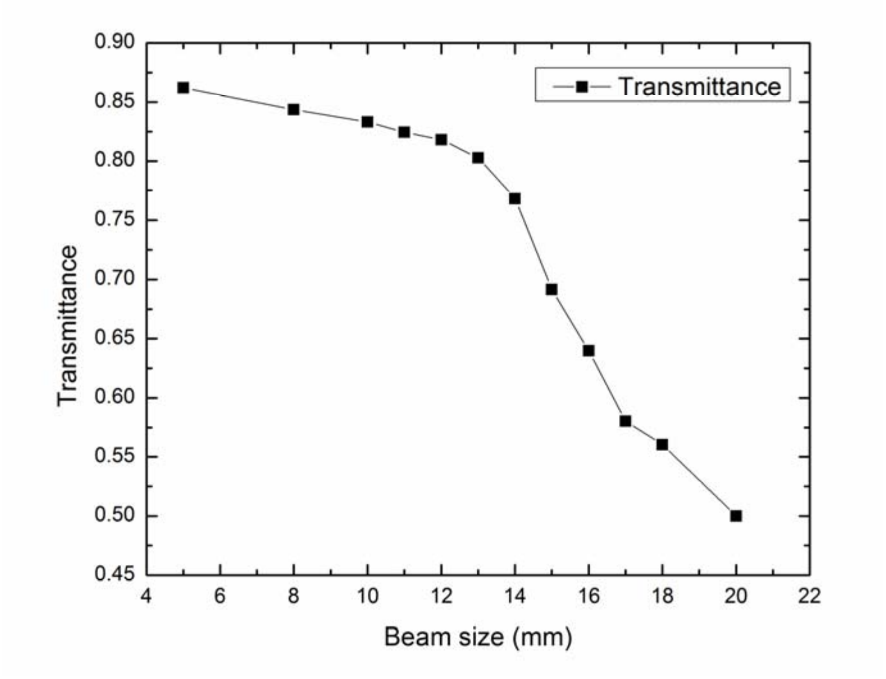

Figure 5.4 Power transmittance of Olympus 25× water-immersion objective lens with the beam size at back aperture. Transmittance decreases when beam size is getting larger.

5.3.4 Schematic of MMM optical pathway

A schematic of the MMM optical path is depicted in Figure 5.5. The light source used is a Ti:Sa laser (Chameleon Ultra II, Coherent, Santa Clara, CA). It outputs approximately 3.3 W of mode-locked pulsed light at 780 nm wavelength. Excitation beam from the laser is expanded by a pair of achromatic lenses (L_1’ and L_2’) and illuminates a

DOE (customized, Holo/Or, Rehovoth, Israel) to generate an 8×8 array. The beamlets generated from DOE diverge with 0.8 degree separation angle. After two more lenses (L_1 and L_2), the beamlets are reflected by a short-pass dichroic mirror (680DCSPXR, Chroma Technology) onto X-Y galvanometric mirror scanners (6215H, Cambridge Technology, Lexington, MA) which is positioned in the focal plane of lens L_2. Scan lens combined with tube lens expands the beamlets to under-fill the back aperture of an objective, balancing the needs of high excitation power at each foci and a large field of view. The objective used is a 25× water immersion lens with 1.05 NA (Olympus, Center Valley, PA). It focuses the array of 8×8 excitation beamlets into foci at the specimen. An image is formed by scanning the excitation foci across the specimen using the scanning mirrors. Emission beamlets collected by the same objective retrace the same excitation paths. They are de-scanned via the scanning mirrors to become stationary irrespective of the scanner motion. After descanning, the beamlets are separated by a dichroic mirror (T435lpxr, Chroma Technology, Bellows Falls, VT) so that the light with the wavelength longer than 435 nm is transmitted toward an MAPMT (H7546B-20, Hamamatsu, Bridgewater, NJ), as the TPEF channel. A short-pass filter (ET680sp-2P, Chroma Technology, Bellows Falls, VT) and a long-pass filter (HQ450lp, Chroma Technology, Bellows Falls, VT) are added just in front of MAPMT to block IR light and select hepatocytes autofluorescence that is longer than 450 nm respectively. At the meantime, the light with wavelength shorter than 435 nm is reflected by the dichroic mirror toward the other MAPMT which is the SHG channel. An identical IR blocker and another band-pass filter with 390±20 nm barrier (HQ390/40m, Chroma Technology, Bellows Falls, VT) are added for SHG signal selection. For both channels, the 8×8 emission beamlets are focused at the centers of the corresponding MAPMT detection areas.

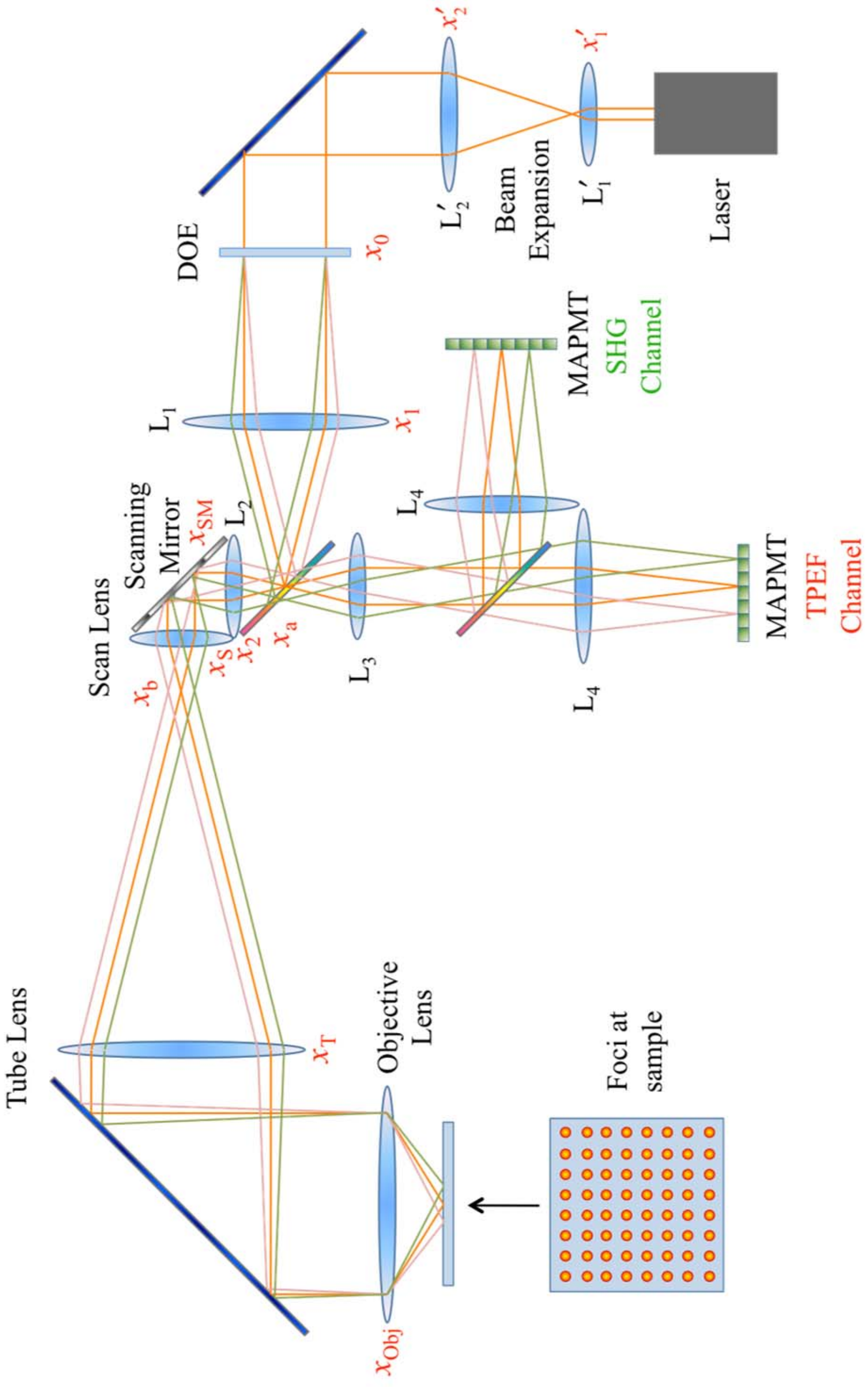

Figure 5.5 Schematic of MMM optical path with TPEF and SHG channels from laser to specimen.

Based on the design of optical path (Figure 5.5) and dimensions of the optical table, the optical lenses for MMM system were chosen and listed in Table 5.1.

Table 5.1 Beam size and choice of lenses for the MMM optical path.

Beam location	Beam size (mm)	Lens	Focal length (mm)	Lens type	Lens size
X_1'	1.5	L_1'	30	Achromatic doublet	1”
X_2'	5	L_2'	100	Achromatic doublet	2”
X_0	5	DOE		Achromatic doublet	1”
X_1	18.14	L_1	80	Achromatic doublet	2”
X_a	7.83	-	-	-	-
X_2	13.28	L_2	25	Eye piece	1”
X_{SM}	1.56	Scanner	-	-	-
X_S	13.28	Scan Lens	25	Eye piece	1”
X_b	7.83	-	-	-	-
X_T	28.12	Tube Lens	175	Achromatic doublet	3”
X_{Obj}	10.94	Objective	7.2	Achromatic doublet	-
X_3	14.16	L_3	35	Achromatic doublet	1”
X_4	26.81	L_4	75	Achromatic doublet	2”

5.4 Basic tests of DOE

Diffractive optical elements are basically a grating with a thin micro structure pattern to generate the desired distribution of spots. The DOE used in our system is able to separate one beam into 64 beamlets in an 8×8 array with 0.8 degree separation angle. The 1” element is transparent with 23 mm clear aperture and designed for 780 nm. According to the data sheet, its efficiency is 70%. Here, a few basic tests were performed on DOE before implementing it into the system, including beam uniformity, pulse broadening and resolution.

5.4.1 Beam uniformity

This test aims to measure transmittance efficiency of DOE and energy variation of the 64 beamlets. To perform it, the laser beam was illuminated on the DOE directly and the beam power before DOE is 1.96 W (Figure 5.6). After DOE, 64 collimated beamlets were diverged and formed a square pattern of 8×8 array on a screen. The power of each point was measured. Average power of 64 beamlets is 23.87 mW with standard deviation of 3.92 mW. Therefore, the power transmittance of DOE is ~77.9% which is a bit better than manufacturing specification of 70%. The uniformity of 64 beamlets is ~84%.

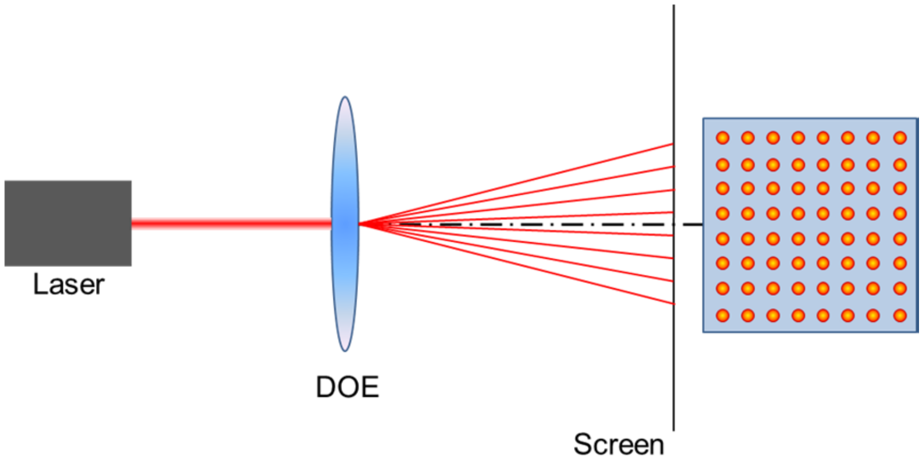

Figure 5.6 Beam uniformity and power transmittance efficiency test for DOE.

5.4.2 Pulse broadening

This test aims to compare pulse width for a system with and without DOE. For pulsed lasers, the fluorescence signal F is given by

$$F \propto \frac{\delta P^2}{f_p \tau}\left(\frac{(\mathrm{NA})^2}{2\hbar c\lambda}\right)^2 \tag{5.1}$$

where δ is the two-photon cross-section at wavelength λ, P is the average laser intensity, f_p is the repetition rate of pulses, τ is the pulse duration, NA is the numerical aperture of the focusing objective, $\hbar$ is the Planck's constant$/2\pi$, c is the speed of light. In a typical setup, all the parameters are fixed except P and τ. Therefore, the relation shows

$$F \propto \frac{P^2}{\tau} \tag{5.2}$$

The changes to pulse duration for the system with DOE and without DOE can be studied by measuring the average beam intensity of excitation light and emission light under the same conditions with DOE (P_w, F_w) and without DOE (P_{wo}, F_{wo}).

$$\frac{\tau_w}{\tau_{wo}} = \frac{P_w^2 F_{wo}}{P_{wo}^2 F_w} \tag{5.3}$$

From Figure 5.7, $\frac{\tau_w}{\tau_{wo}} = \left(\frac{F_{wo}}{P_{wo}^2}\right) \Big/ \left(\frac{F_w}{P_w^2}\right) = 91.835/70.37 \approx 1.305$, the results show that the pulse duration with DOE is 1.305 times than without DOE, i.e. the pulse is 30.5% wider when a DOE is utilized in a system than it is not being used. This would reduce the two-photon excitation probability.

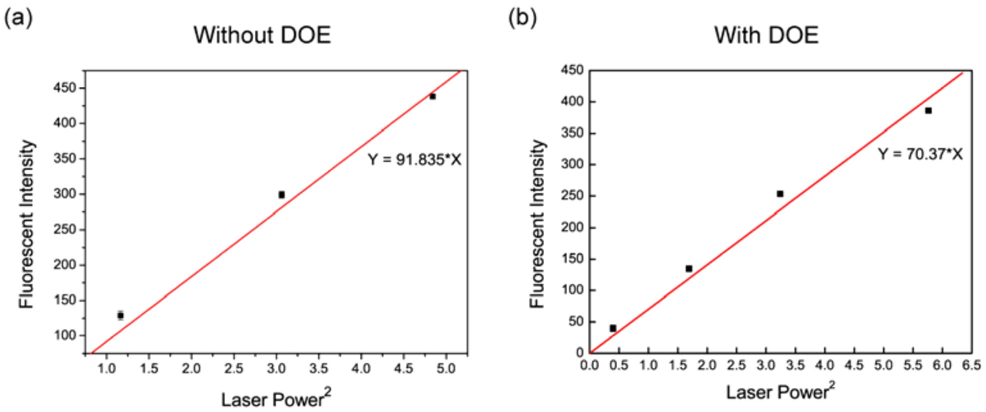

Figure 5.7 Pulse width in the systems without DOE (a) and with DOE (b). Slopes of the linear curve illustrates the ratio of fluorescence signals to square of laser power, which are proportional to pulse duration. Comparing slopes in (a) and (b), pulse is broadened 30.5% when DOE is utilized in a two-photon microscopy.

To reduce the effect of broader pulse, a pulse compressor (Chameleon PreComp, Coherent, Santa Clara, CA) is implemented after the laser. It has 680-1080 nm tuning range and above 90% transmission across entire tuning range. The mechanism of the pulse compressor is shown in Figure 5.8. Pulse is positively chirped in an optical imaging system after a number of materials (such as lenses) for wavelengths shorter than about 1.5 mm because red colors always propagate faster than blue colors and precede the blue wavelengths in the pulse. Inside the pulse compressor, a negative GVD is created by the angle dispersion of prisms and optical gratings to adjust the time and position of red wavelength and blue wavelength to let blue colors catch up with red ones, resulting in the compensation of positive dispersion.

With the compensation of pulse compressor, the pulse width when arriving on specimen is corrected to be as narrow as it comes out from laser so that it would not be affected by the optics along the path inclusive of DOE.

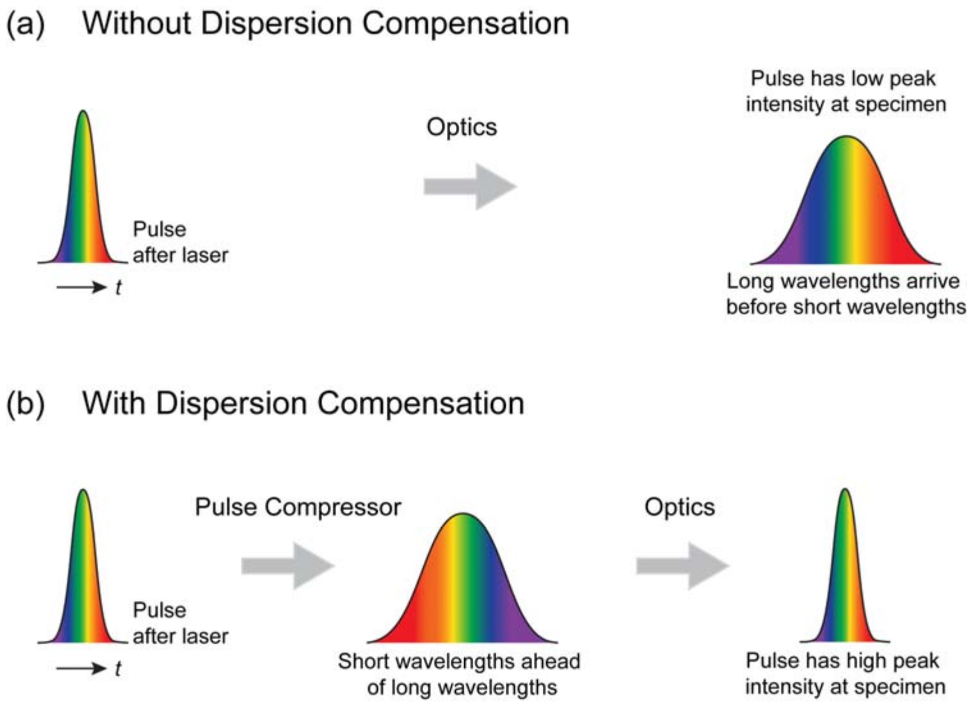

Figure 5.8 Function of a pulse compressor on pulse width adjustment. A negative GVD is created by several prisms to let red wavelengths traverse longer distance in glass than blue wavelengths. As a result, the pulse width when arriving on specimen is as narrow as it comes out from laser so that it won't be affected by the optics along the path inclusive of DOE.

5.4.3 Point spread function (PSF)

The intensity in space near the focus is described by the illumination point spread function, $\mathrm{PSF}(x,y,z)$, and PSF^2 is used to define the true optical resolution in multiphoton microscopy [79]. It can be calculated by fitting the lateral and axial intensity-squared profiles to a Gaussian function. The most practical way to determine the resolution of an optical system is to measure the Full-Width at Half-Maximum (FWHM) of the Gaussian curve - PSF^2 for a multiphoton system, as shown in Figure 5.9.

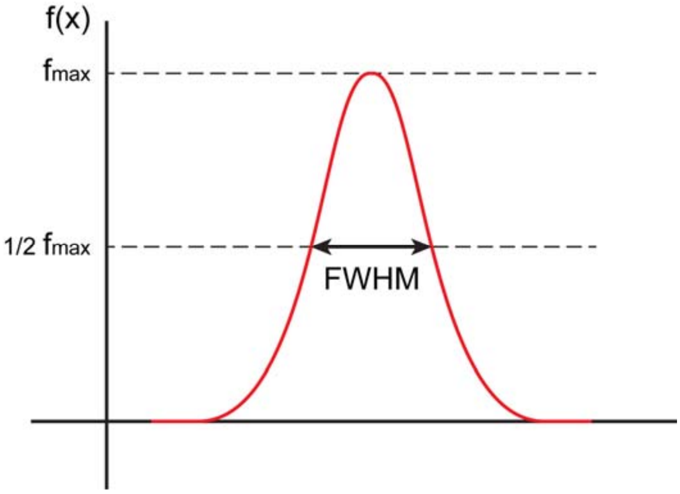

Figure 5.9 Illustration of optical resolution measurement by calculating FWHM of a Gaussian curve. In a multiphoton microscopy, the Gaussian profile is fitted by square of point-spread-function (PSF^2).

To study the effect of implementing DOE on optical resolution, PSF of with and without DOE for an existing two-photon microscopy were measured and each FWHM was calculated for comparison. The laser at 780 nm wavelength and an oil immersion objective lens with NA 1.0 were used in this test. 0.1 µm diameter Yellow-Green fluorescent beads mixed with 2% low-melting-point agarose gel at concentration of 1:2000 was prepared onto slides as imaging samples. Details of fluorescent beads sample preparation will be described in Section 6.2.3. Among a series of z-stack images with 0.1 µm interval distance, the image that shows the center of a single bead was chosen. Pixel intensities on a line that passes the bead center were extracted and fitted with Gaussian function by Matlab fitting tool to calculate the FWHM.

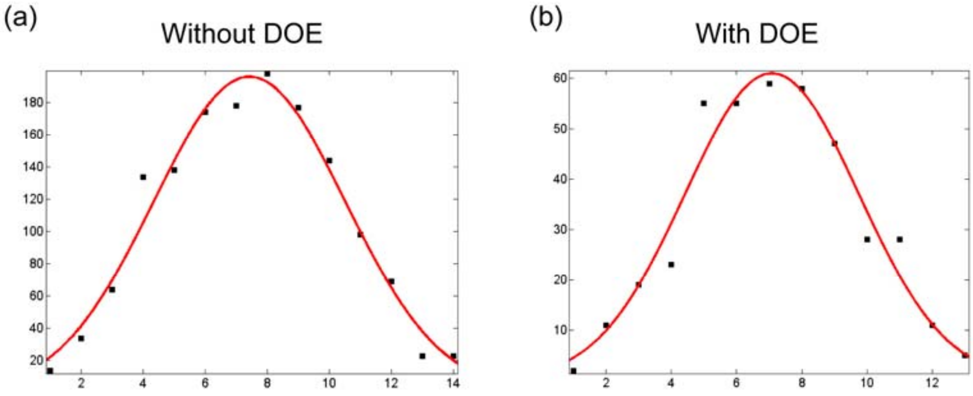

Figure 5.10 PSF measurement without DOE (a) and with DOE (b) in an existing multiphoton microscopy. 0.1 µm fluorescent beads are imaged. After fitting the intensity of pixels on a line that passes the center of a bead by Gaussian function, the FWHM of the system without DOE is 0.7250 µm while FWHM with DOE is 0.6279 µm.

The fitting curves for PSF without and with DOE are shown in Figure 5.10. From the calculation, the FWHM without DOE is 0.7250 µm while with DOE is 0.6279 µm. It illustrates that the addition of DOE does not reduce the system resolution.

5.5 MAPMT detection unit

The detector that is being used in our system is a multi-anode photomultiplier tube. It is of the matrix type multi-anode with metal channel dynodes for electron multiplication [113]. This type of MAPMT has very low crosstalk during secondary electron multiplication as a focusing mesh directs emitted photoelectrons from the photocathode to the first dynode and subsequent dynodes with minimal spatial spread in the secondary electron flow. Besides a low crosstalk, these tubes have excellent magnetic immunity as a result of metal housing and the minute distance between the dynodes electrodes. In our particular case, for an optimal detection at the detector, an 8×8 matrix MAPMT was chosen to match the number of foci generated as 1 laser beam splits into 64 beamlets at the DOE. The large effective detection area per foci ensures that scattered emission photons are more efficiently collected [12].

5.6 Lateral and axial stage control

In X-Y directions, a motorized stage (OptiScan ES111, PRIOR Scientific, Rockland, MA) is used. Controlled by Prior ProScan II controller, it has 126mm×76mm travel range and 1 µm resolution. The stage in this MMM system is not only for adjusting lateral movement, but also support our customized automated slicing module which will be discussed in Chapter 6.

To achieve 3D scanning for a tissue block, an automated slicing module is designed with a z-direction translational stage with 0.1 µm resolution and cutting function. For accomplishment of scanning at different depths, the objective lens is fixed on an electric-driven fast piezo focus system (PD72Z4CAQ, PIFOC, Physik Instrumente, Germany) and then manually moved in to the appropriate axial position using the manual dial of the microscope's objective positioner. The piezo objective positioner is able to provide 400 nm travel length and 2.5 nm step resolution so that the system can do fine 3D stack scanning within each axial step of the automated slicing module. It communicates with the computer through an RS232 or USB cable and can be controlled by company software or our own developed software.

5.7 Electronics in MMM system

Electronic parts in MMM system connect MAPMT, X-Y scanners and computer to accomplish a complete signal processing procedure of sending positional commands to scanners, receiving imaging signals from MAPMT, processing the signals and sending them to computer forming a part of image, then to the next position. This network is mainly consisting of Xilinx FPGA board, Xilinx intermediate board, X-Y scanner drivers with power supply and 64-channel discriminators. The network of electrical parts are shown in Figure 5.11.

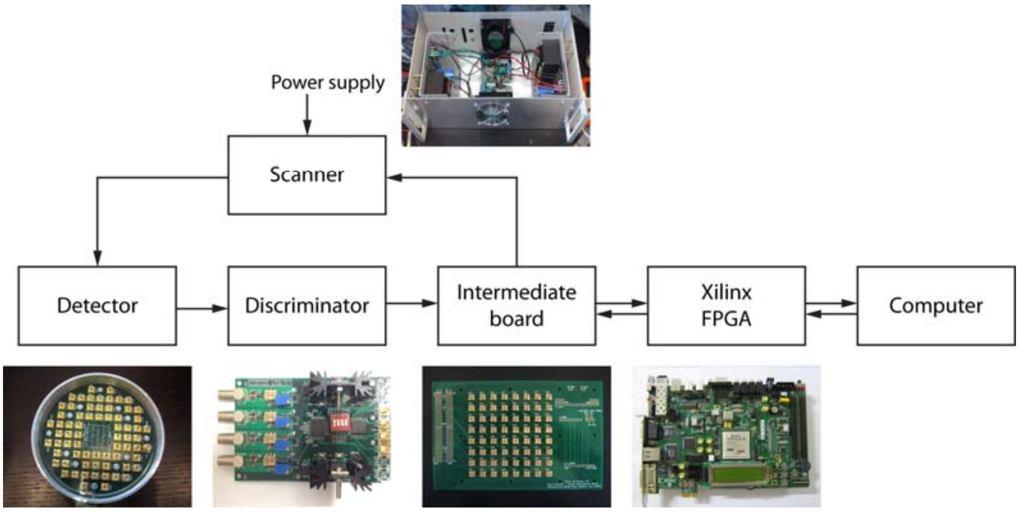

Figure 5.11 network of electrical parts in MMM system. Xilinx FPGA board is the main control in the system to send commands to scanner (supplied by in-house assembled power supply) and receive signals from MAPMT detector after signal acquisition and discrimination by discriminators.

5.7.1 Xilinx FPGA board and intermediate board

The main processor of the electronic circuitry is Xilinx FPGA board (Virtex-5 FXT FPGA ML507 Evaluation Platform, Xilinx, US). It is used not only to receive electrical signal that is converted from optical signal by MAPMT and processed by discriminators, but also to send the data to computer showing as an image, as well as to send scanning commands to X-Y scanners and piezo objective positioner. To connect with different electrical parts, a Xilinx intermediate board was designed. Three regions on the board were separated based on functions: 1) the first region with two 96-pos PCB receptacles (ssw-132-01-g-t, Samtec, New Albany, IN) connects to Xilinx FPGA board for data transfer; 2) the second region in the middle with 64 SMB connectors is used to connect MAPMT board to receive image signals; 3) the third region with several breakaway headers is used to connect with X-Y scanner drivers through a ribbon cable.

5.7.2 Scanning mirror control

The X-Y galvanometric mirror scanners (6215H, Cambridge Technology, Lexington, MA) are two mirrors with 6 mm aperture driven by two independent single axis servo drivers (MicroMax 671215HHJ-1, Cambridge Technology, Lexington, MA). Each servo driver supplied by +28V power (HD28-4-A, Power-one, San Jose, CA) receives commands from Xilinx FPGA board through a ribbon cable (3302/34, 3M, Two Harbors, Minnesota, MN). Among 30 conductors of the ribbon cable, 10 are connecting to ground, 4 for signaling to X and Y driver respectively, 16 for sending a 16-bit binary number to scanners for positioning. It is noteworthy that scanners need to be controlled by 16-bit signal while Xilinx FPGA board has only 12 bits. Therefore, one main function of Xilinx intermediate board is to expand 12 bits to 16 bits: 12 of them are given by Xilinx FPGA board; 4 bits are set manually (0, with shunt; 1 without shunt). Two commands are sent from Xilinx FPGA board, through intermediate board to X and Y galvanometric mirror respectively for positioning. The X-galvanometric mirror scans a line by tilting its angle in one direction, each angle corresponds to one pixel; while Y-galvanometric mirror stays in one position until one line in x direction is completed, or equivalently when the number of point scans in one line is fulfilled.

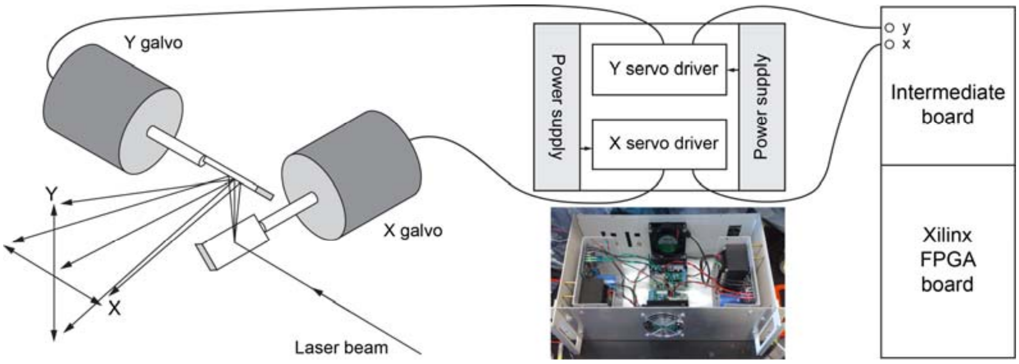

Figure 5.12 Scanning mechanism and electrical connection of scanner control. The X-Y scanners composed of two galvanometric mirrors are controlled by an in-house assembled power supply inclusive of a servo driver and a +28V power supply for each mirror. The servo drivers connect with Xilinx FPGA board through intermediate board to receive commands from software.

5.7.3 Signal acquisition and processing

The output electrical signals from MAPMT are amplified by discriminators before being sent to computer through Xilinx FPGA board. Although there are plenty of commercially available discriminators in the market for the appropriate readout of specific photodetectors, many of them have only one or two independent signal channels, and are either expensive or correspondingly of slow-speed. To simultaneously acquire 64 independent channels from MAPMT, the customized discriminators were developed using low-noise board design techniques and advanced electronic components such as monolithic broadband signal amplifiers and re-configurable logic chips which offers experimental flexibility. In addition, one discriminator board were designed to discriminate 4 individual photon counting amplifier, so that 16 boards are required for one 64-channel MAPMT in this case. It is flexible to combine different numbers of board for various microscopy configurations, such as for MMM with 6×6 or 4×4 array of foci.

The schematic diagram of one single channel of a discriminator board is shown in Figure 5.13. Typical photon-induced PMT signals generate short nanosecond pulses in the mV-range (50 Ω impedance system). In our case, the amplitude of Hamamatsu's MAPMT is about -50 mV. All inputs (In) are terminated (R_{term}) to provide 50 Ω input impedance, thus minimizing reflections. The -50 mV PMT signals are pre-amplified by a low-noise monolithic broadband amplifier (MAR-8ASM+, Mini-Circuits, Brooklyn, NY) that has wide bandwidth ($\leqslant 1$ GHz) and high gain (23 dB at 1 GHz) to about 600 mV. That therefore can be confidently discriminated by means of an appropriate high-speed comparator (MAX999, Maxim Integrated products, Sunnyvale, CA). The discrimination level – threshold voltage at the comparator's negative input can be adjusted by a 25-turn potentiometer and set for dark noise to experimental environment.

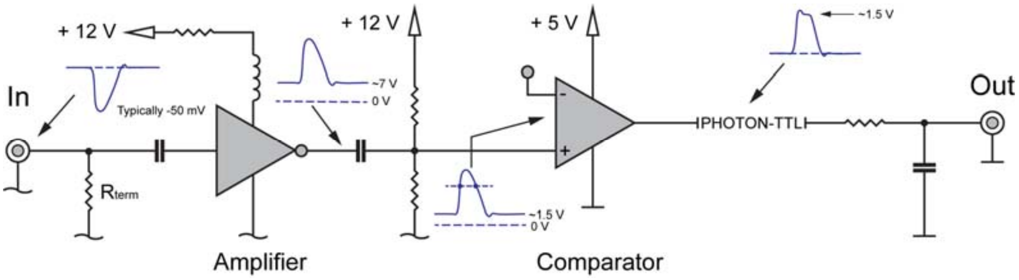

Figure 5.13 Schematic layout of a single channel discriminator. The input PMT signals are pre-amplified by a low-noise monolithic broadband amplifier (MAR-8ASM) that has wide bandwidth (⩽1 GHz) and high gain (23 dB at 1 GHz), then discriminated by a high-speed comparator (MAX999). The threshold voltage of comparator is determined by tuning a 25-turn potentiometer for dark noise setting.

Figure 5.14 shows one discriminator board with 4 individual channels and 16 discriminator boards assembled together with Xilinx FPGA board for a 64-channel detection. Collected signals from MAPMT are transferred to discriminators via SMB-LEMO cables and sent to Xilinx FPGA board via SMB-SMB cables after amplification and discrimination.

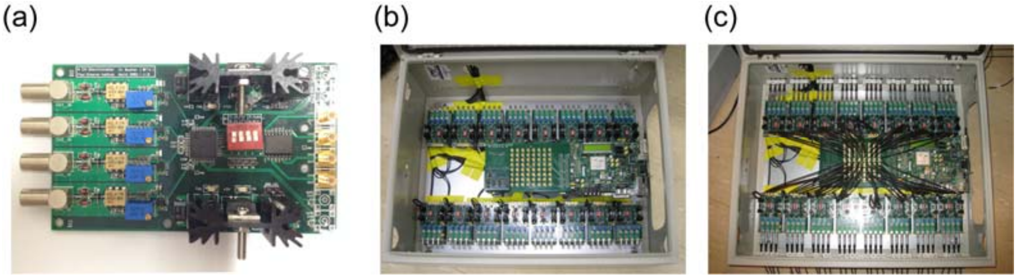

Figure 5.14 Finished product of one discriminator board with 4 individual channels (a) and sixteen boards assembled for 64 channels (b)(c). (a) Signal comes in from left side and out to the right after amplification and discrimination. The knob on the potentiometer (blue cube) is used to adjust discrimination level. (b) All sixteen discriminator boards are assembled together with Xilinx FPGA board and intermediate board in one box. (c) Discriminators are connected with MAPMT with SMB-LEMO cables to receive signals and connected with intermediate board with SMB-SMB cables to transfer signals to Xilinx FPGA board.

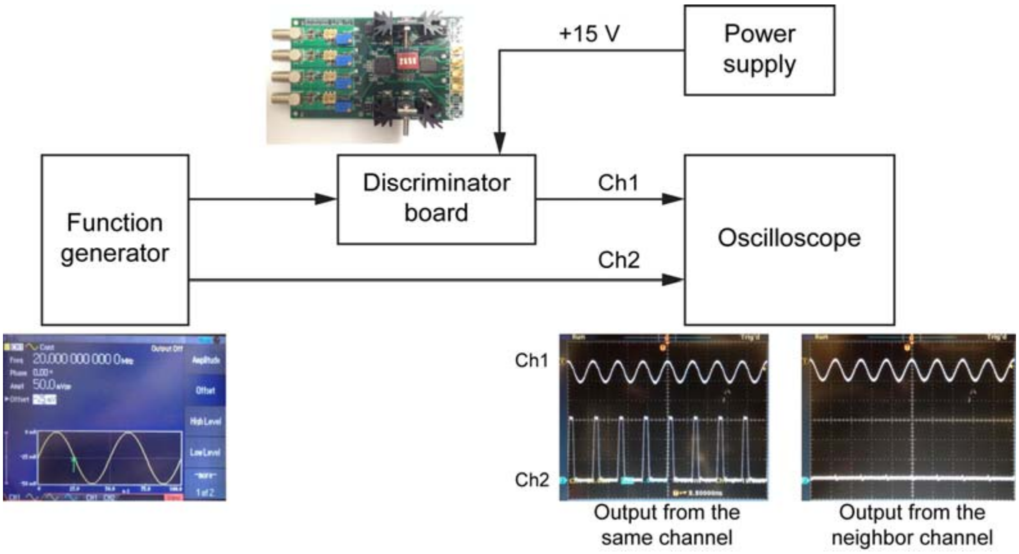

Figure 5.15 Flow chart of discriminator signal quality test. The discriminator board was powered by +15V DC and input by 20 MHz sine wave which gives 800 counts in 40 µs dwell time, similar with PMT signals. Output from same channel and neighbor channel with input were observed by an oscilloscope. For the same channel, output signals have the same frequency of 20 MHz and less than 5 V amplitude; for the neighbor channel, output signals are small and negligible.

After assembling, a simple test was performed to examine signal quality for each channel of discriminators and cross-talk between neighbor channels. Figure 5.15 shows the flow chart and results of the test. The discriminator board was maintained at working status by a +15V DC power. A sine wave at 20 MHz that gives 800 counts in 40 µs dwell time from a function generator (AFG3102, Tektronix, Beaverton, OR) was used as input to mimic PMT signals. An oscilloscope was connected to the function generator and discriminator board to observe both input and output signals. From the same channel with input function, the output signal should have the same frequency of 20 MHz and less than 5 V amplitude; while from the neighbor channel, the output signal should be very small and negligible.

5.7.4 Two channels synchronization

To simultaneously acquire both TPEF and SHG signals in one scan, two channels must be synchronized. Even though they have individual acquisition system inclusive of one Xilinx FPGA board, a set of discriminators and even a computer, only one channel should dominate the scanning and acquisition process, while the other is dependent. In this case, we choose TPEF channel as the dominant channel. Xilinx FPGA board of SHG channel is connected to the board of TPEF channel, so that SHG channel will not start acquiring data until TPEF board sends commands to it.

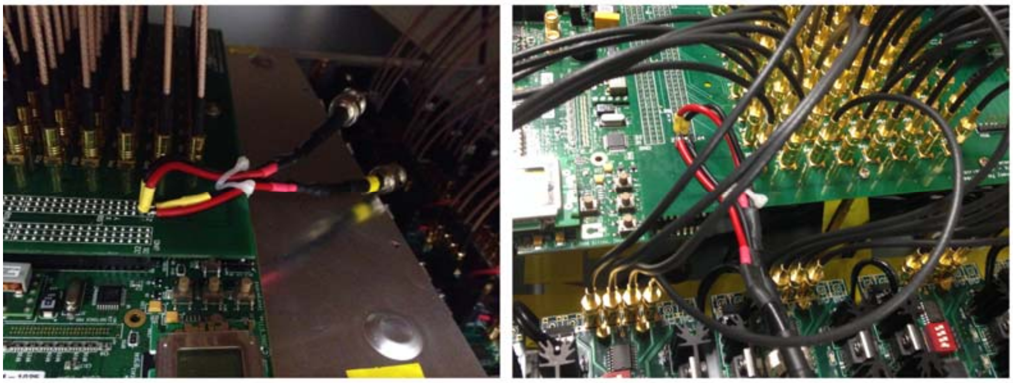

Figure 5.16 Synchronization of TPEF and SHG channels by connecting two Xilinx FPGA boards together and only TPEF channel is connected to scanner and runs the signal acquisition dominantly.

5.8 Software

Individual module control is achieved with the aid of the in-house developed software named “MIC”. Visual Studio C++ is the elected programming software for software development due to its good performance, efficiency and flexibility. The purpose of the in-house software is to control the whole imaging procedure, cooperating with hardware inclusive of scanning mirrors, a piezo stage, a lateral motorized stage and a Xilinx FPGA board.

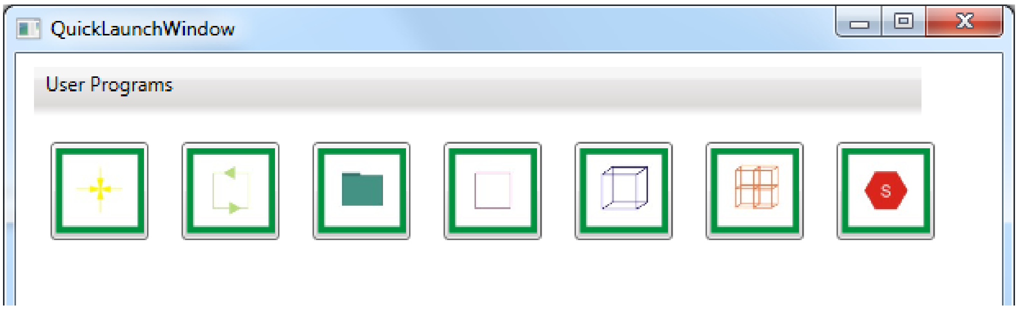

Figure 5.17 Options of program functions. According to icons from left to right: 1) Center microscope imaging area; 2) Continuous image acquisition (without saving images, mainly used for adjust focal plane); 3) Continuous image acquisition and save image; 4) Acquire a single 2D section; 5) Acquire a 3D volume (controlling piezo for 3D optical sectioning); 6)Montage to form a large image cube (controlling both piezo and lateral motorized stage to scan a larger imaging area); 7) Stop acquisition.

Different functions are listed in Figure 5.17 and to be chosen in a “Quick Launch Window” when it starts, mainly including:

1) Continuous image acquisition (without saving images, mainly used for adjust focal plane);

2) Continuous image acquisition and save image;

3) Acquire a single 2D section;

4) Acquire a 3D volume (controlling piezo for 3D optical sectioning);

5) Montage to form a large image cube (controlling both piezo and lateral motorized stage to scan a larger imaging area).

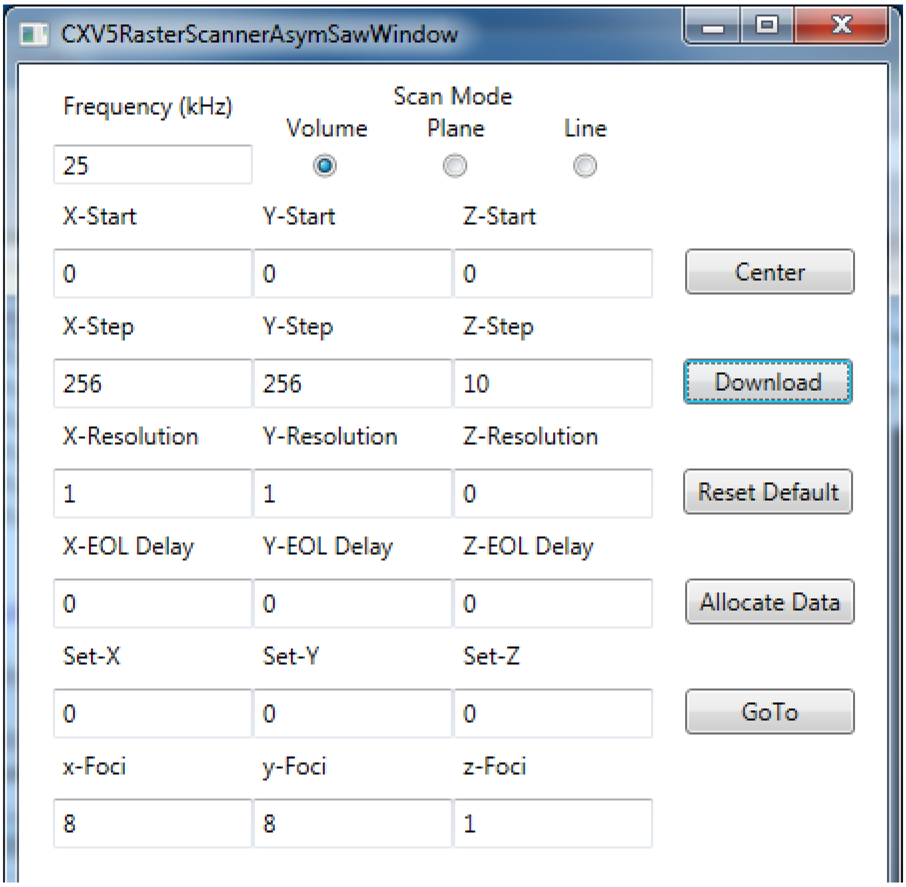

Frequency (kHz): 25

Scan Mode: Volume ● Plane ○ Line ○

X-Start	Y-Start	Z-Start
0	0	0
X-Step	**Y-Step**	**Z-Step**
256	256	10
X-Resolution	**Y-Resolution**	**Z-Resolution**
1	1	0
X-EOL Delay	**Y-EOL Delay**	**Z-EOL Delay**
0	0	0
Set-X	**Set-Y**	**Set-Z**
0	0	0
x-Foci	**y-Foci**	**z-Foci**
8	8	1

Figure 5.18 Settings for scanning control. Frequency: pixel dwell time; X-/Y-/Z-Start: coordinates of the starting location; X-/Y-/Z-Step: pixels numbers for each foci in a sub-region; X-/Y-/Z-Resolution: pixel size; Set-X/-Y/-Z: coordinates of a specific location.

Scanning configurations can be modified in optical scanner section from inventory list. Figure 5.18 shows the settings those are commonly used for this MMM system. “Frequency” is set for pixel duration, i.e. 25 kHz means dwell time at each pixel is $\frac{1}{25\text{ kHz}} = 40$ µs. “Start” is the coordinates of the start point (x_0, y_0, z_0). “Step” is the pixel number for all three axes in each sub-region; since the whole 8×8 array and all its sub-regions are square, X- and Y- Step need to be set to the same value. “Resolution” is the pixel size during scanning; number $N = 0, 1, 2, \ldots$ represents 2^N times of the smallest pixel size which theoretically is 0.1 µm; Table 5.2 shows real pixel size and minimum required step number for different resolution number. “Set” is to let scanner stop at a specific coordinates without scanning.

Table 5.2 Numbering of resolution setting to real pixel size and required minimum step number accordingly.

Resolution N	2^N	Pixel size (µm)	Required step number
0	1	0.1	460
1	2	0.2	230
2	4	0.4	115
3	8	0.8	58
⋮	⋮	⋮	⋮

Once all the settings are set, the data acquisition can be initialized by the software. The acquisition starts from command center – Xilinx

FPGA board by sending location coordinates to scanner and piezo for (x, y, z) positioning. MAPMT records the sum of photon counts within one pixel dwell time according to pre-set scanning frequency and converts the photons into voltage before entering 64-channel discriminators. FPGA receives the signal after it being amplified and discriminated by the discriminators, records it for this specific location and sends scanner and piezo the next location coordinates until all steps are finished. Then the completed image will be displayed on the computer and stored in destination folder.

5.9 Conclusions

We developed a novel dual channel multifocal multiphoton microscopy to increase imaging speed for liver fibrosis study. TPEF and SHG channels were synchronized to detect hepatocytes fluorescence and collagen signals simultaneously. A DOE was utilized to generate an 8×8 array of foci so that 64 individual beamlets would scan the specimen concurrently. The DOE has high uniformity for all beamlets and does not affect system resolution, while pulse is broadened when using DOE so that a pulse compressor was implemented into the system to compensate the effect. MAPMT was applied to detect emission light from 64 foci accordingly in a descanned detection geometry with the benefit of compensating lower SNR. The optical signals were converted into electrical signals, amplified and discriminated by 64-channel discriminators and sent to the central processor – Xilinx FPGA board and to computer. All the scanning control is done by an in-house software.

Chapter 6

Characterization and Improvement of MMM for the Study of Liver Fibrosis

In this chapter, characterization and improvement of the prototype MMM for the study of liver fibrosis are discussed. Preparation procedures of various samples are described. The results of system uniformity, pixel size measurement and optical resolution measurement will be presented in the next section. To imfprove MMM performance for liver fibrosis study, an image post-processing method for photon reassignment and the design of an automated slicing module are discussed in the end.

6.1 Introduction

Liver fibrosis is a major health problem in the world as it is a precursor to cirrhosis and primary liver cancer. There is about 3% of the world's population that has chronic hepatitis C viral infection, which is only one of the causes of liver fibrosis [114]. Therefore, accuracy of liver fibrosis diagnosis is very critical for guidance to treat and prevent development toward severe stages.

For current liver fibrosis diagnosis, biopsy with subsequent histopathological evaluation is still the gold standard method to assess its severity [25, 35]. However, it takes at least a few hours to fix, section, stain and be evaluated by a pathologist. In addition, the evaluation is qualitative and features-based. Subjectivity occurs during pathologic assessment. Therefore, the current biopsy process is slow and has a higher chance of classifying the same biopsy into different stages by pathologists. Moreover, the sample used for estimating fibrosis extent is a 2D slice from a biopsy volume, which provides limited information of the real 3D situation of the liver.

In previous chapters of this thesis, SHG/TPEF imaging modalities were studied on their application for collagen quantification in different fibrotic stages, and a new multifocal multiphoton microscopy has been developed to provide 64-fold faster imaging speed. We now propose to apply MMM in monitoring liver fibrosis progression in a spatial-dependent manner. It can be a promising tool as a real-time optical examination for clinical applications such as providing instant assessment during surgeries.

To achieve the goal, the new MMM system should not only have high-resolution to visualize liver structure inclusive of hepatocytes and collagen fibrils, but also have the ability to present high-quality 3D images from 2D scanning without any loss of information. In this work, we tested the PSF of the MMM system to validate its high resolution and feasibility for liver imaging. We also developed an algorithm for photon reassignment to improve image contrast. Furthermore, an automated slicing module was designed for an imaging-slicing-imaging procedure so that 3D reconstruction could be performed in the future.

6.2 Materials and methods

6.2.1 Preparation of fluorescent solution

Fluorescent solutions were prepared for optical alignment, image uniformity and pixel size measurement purposes. Figure 6.1 shows the fluorescence spectra of a few fluorescent dyes after two-photon absorption [115]. After being excited by Ti:Sa laser at 784 nm with continuous wave power of 0.8 W and a pulse duration of 100 fs, fluorescein (labeled as F) reached a fluorescence flux peak of 36 a.u. at

520 nm. Moreover, fluorescein dye is considered to be the most common fluorescent probe due to its high molar absorptivity, large fluorescence quantum yield and high photostability. Since our light source is 780 nm from Ti:Sa laser which is very close to the setup used in that experiment, Figure 6.1 is a very good reference for choice of fluorescent dye. In our new dual-channel MMM system, two channels are separated by a 435 nm dichroic mirror. Emission beamlets longer than 435 nm transmit through the mirror and are recorded by MAPMT as a TPEF channel for visualizing hepatocytes in this project. Therefore, fluorescein is the best choice for TPEF channel alignment and test.

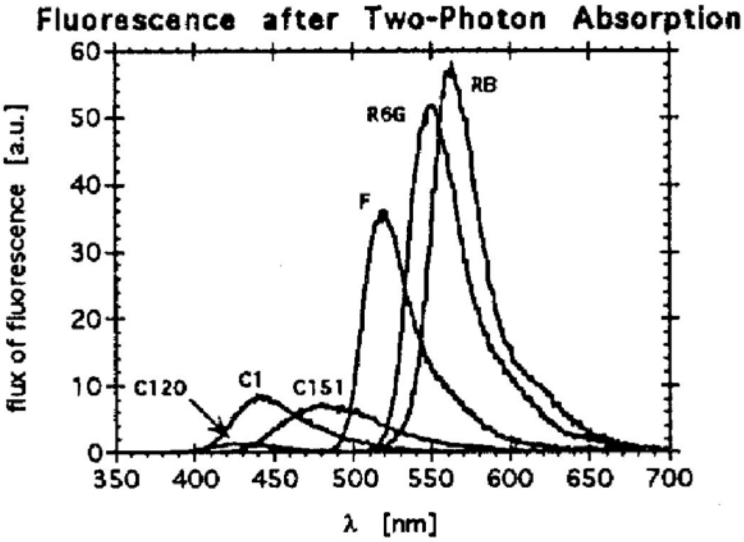

Figure 6.1 Comparison of fluorescence flux after two-photon absorption of the 10^{-5} M solutions in ethanol. The excitation wavelength at two-photon absorption was 784 nm at a continuous wave power of 0.8W and a pulse duration of 100 fs. Fluorescein (labeled as F) has a fluorescence flux peak of 36 a.u. at 518 nm, and coumarin 1 (labeled as C1) has a fluorescence flux peak of 9 a.u. at 450 nm. (Adapted from [115], reprinted with permission.)

Fluorescein fluorescence is pH dependent. Its buffer solution was made with mixture of 150 mM H_3BO_3 and 1M NaOH so that the pH value was maintained above 9. Then fluorescein powder (46955, Sigma-Aldrich, St. Louis, MO) was dissolved in the buffer solution. 355 µM fluorescein solution was made for TPEF channel alignment and uniformity test; 1.775 mM fluorescein solution was made for pixel size measurement.

Coumarin 1 was picked for SHG channel alignment and test because fluorescent signals from fluorescein cannot be reflected by the 435 nm dichroic mirror to enter SHG channel. In Figure 6.1, coumarin 1 (label as C1) shows the strongest fluorescence intensity among the dyes whose emission peaks are at the shorter wavelength range than fluorescein, especially at 435 nm, although the intensity is much weaker than fluorescein. The solution was made by dissolving coumarin 1 powder (D87759, Sigma-Aldrich, St. Louis, MO) in 99.9% methanol.

Table 6.1 shows the fluorescence characteristics after two-photon absorption of fluorescein and coumarin 1 dissolved in 10^{-3} M methanol [115]. Both of the dyes can be excited by 780 nm Ti:Sa laser and their emission peaks are at the wavelength ranges for TPEF (>435 nm) and SHG (<435 nm) channels respectively. Fluorescein clearly has larger absorption extinction, hence its fluorescent intensity is higher than coumarin 1 and this matches the fluorescence flux curves in Figure 6.1

Table 6.1 Fluorescence characteristics after two-photon absorption of the 10^{-3} M solutions in methanol [115].

Substance	λ_{ab} (nm)	λ_{em} (nm)	ε (L mole^{-1} cm^{-1})
Fluorescein	498	518	6.39×10^4
Coumarin 1	374	450	2.54×10^4

6.2.2 Ronchi ruling slide as a test target

For the MMM system, 64 sub-regions at the specimen are scanned at the same time. Each of them should be connected with its neighbor regions well after scanning to form a complete large image. Therefore scanning steps and resolution need to be set precisely. Ronchi ruling slide was used to measure pixel size so that scanning steps can be calculated by $\frac{\text{field of view for each sub-region}}{\text{pixel size}}$.

A typical Ronchi ruling is illustrated in Figure 6.2 and it consists of constant-interval bar and space running parallel to each other, like a grating. A line and its neighbor space form a line-pair (lp). The reason of keeping the line width and line spacing as one-to-one ratio is when two identical Ronchi rulings are placed in contact with their respective lines running at right angles to each other, the spaces will then become small perfect square. Otherwise the resulting spaces would not be squares, but rectangles. High precision Ronchi ruling glass targets are excellent for evaluating resolution, field distortion, and parfocal stability. Commercial Ronchi rulings have various versions with different lp per length unit, such as inch and millimeter. In this experiment, a 600 lp/mm Ronchi ruling slide was utilized. A very little amount of 1.775 mM fluorescein solution was dropped onto the slide. A coverslip was placed on the fluorescein solution and pressed tightly to let all the solution fully fill the line space without leaving any on the line. After scanning, an image with alternated black and white strips should be shown (as illustrated in Figure 6.2) and the black strips correspond to the lines while white strips correspond to the spaces on the Ronchi ruling due to strong fluorescent signals from fluorescein solution. Since the Ronchi ruling is 600 lp/mm, each lp is 1.667 µm. Pixel size then can be calculated by counting pixel numbers in one lp on the image.

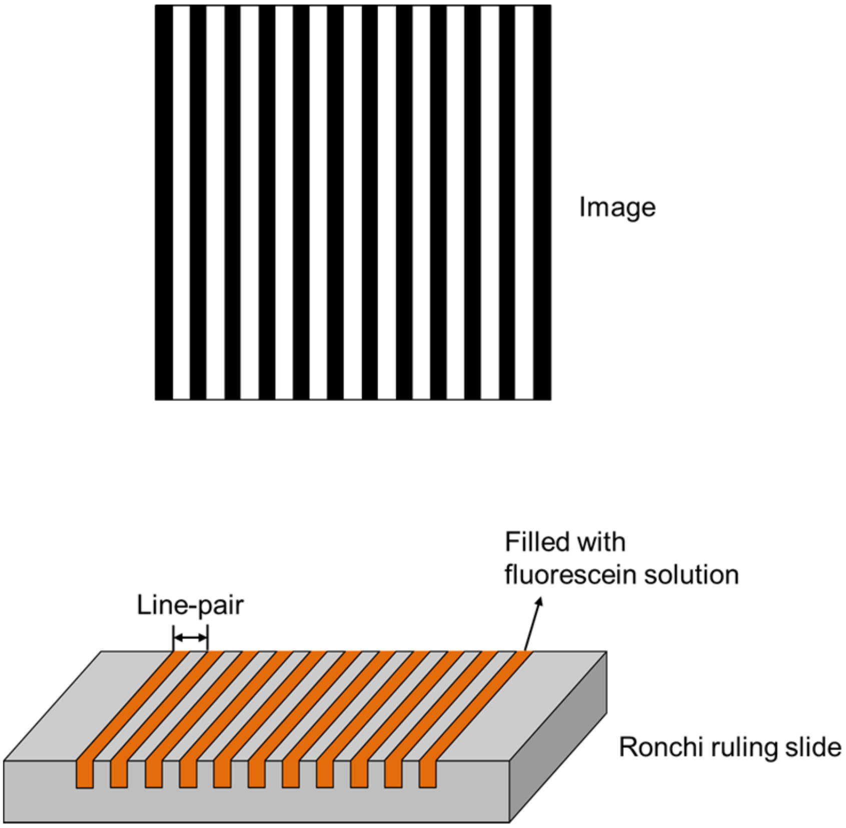

Figure 6.2 Structure of a typical Ronchi ruling slide. One line and one space next to it form a line-pair (lp). The Ronchi ruling slide used in this experiment is 600 lp/mm for pixel size measurement by filling the slots with 1.775 mM fluorescein solution and covered with a coverslip.

6.2.3 Preparation of fluorescent beads samples

Different sizes of fluorescent beads sample were prepared for optical resolution measurement. 4 µm, 1 µm, 0.5 µm and 0.1 µm diameter yellow-green fluorescent latex microspheres beads (FluoSpheres, Life technologies, Carlsbad, CA) at concentrations of 0.02% and 0.05% were made respectively. To immobilize the bead solution on glass slides, 2% agarose gel was prepared by mixing agarose powder (UltraPure, Life technologies, Carlsbad, CA) and distilled water. Due to the low melting point of 65.5°C, the gel was kept in 72°C water bath (AquaBath, Thermo fisher scientific, Waltham, MA) for standby. Took 0.2 µl beads solution into melted 1000 µl agarose gel and mixed well with vortex (Scientific Industries, Inc., Bohemia, NY) for the concentration of 0.05%; while mixed 0.5 µl beads solution with melted 1000 µl agarose gel for the concentration of 0.02%. Dripped 10 µl mixed solution on glass slide, covered with coverslip and sealed well.

6.2.4 Preparation of animal model and tissue samples

All animal-related experimental procedures were carried out in conformity with the laboratory animal protocol approved by the IACUC. Male Wistar rats at an average weight of 220 g were used to establish the TAA-induced liver fibrosis model. Two rats were housed in each cage in the BRC of Biopolis, A*STAR with free access to laboratory chow and water in a 12:12h light/dark schedule. TAA was administrated into the rats through ip. with 200 mg/kg of body weight with PBS, three times a week for 14 weeks. Rats were sacrificed at week 0 (control), 2, 4, 6, 8, 10, 12, 14 after liver fibrosis induction. Liver tissues were extracted, paraffinized and sectioned with a thickness of 50 µm.

6.2.5 Maximum likelihood estimation for photon reassignment

In true experiments by using MAPMT, with severe scattering in a turbid specimen, scattered emission photons will still arrive at neighboring anodes, resulting in the formation of ghost images, which are duplicates of the image acquired by one focus visualized in neighbor sub-images. To remove the ghost images and increase the SNR of the original image, these scattered emission photons should be reassigned to their original pixels. A post-processing method based on maximum likelihood estimation has been developed by quantifying the crosstalk between the different anodes of the MAPMT based on the actual optical model of the MMM system [116].

The signal for an MMM system with $N \times N$ equally spaced foci at location (x, y) of an imaging sensor (CCD or CMOS) at any scan location (i, j, k) can be written as

$$I_{MMM}\left(x, y, i, j, k\right) = \sum_{m,n}^{N,N} \left\{ \left[E_0^2 h^2 \left(\vec{x} - \vec{x}_{m,n}^{0} - \vec{x}_{i,j}^{'} \right) \cdot O\left(\vec{x} + \vec{x}_{k}^{'} \right) \right] \otimes h_m\left(\vec{x}, k \right) \right\} \Big|_{z=0} \tag{6.1}$$

In this equation, the emission PSF is $h_m(\vec{x}) = (1-\alpha) h(\vec{x}) + \alpha h'(\vec{x})$, assuming $h_m(\vec{x}) = h(\vec{x})$ in the absence of scattering and $h'(\vec{x})$ represents the PSF for the scattered emission photon. Without the emission scattering effect, the emission photon scattering strength α is zero; otherwise, $\alpha(k)$ is depth dependent but invariant over each 2D plane. For specimen with tissue-like scattering property, the mean of detected photon count $N(a,b,i,j,k)$ by each anode (a,b) at each scan location (i,j,k) is

$$I_{MD}(a,b,i,j,k) = (1-\alpha(k))H_0 I(a,b,i,j,k) + \alpha(k)\sum_{m,n}^{N,N} C_{(a,b),(m,n),k} I(m,n,i,j,k) \tag{6.2}$$

where (a,b) are the PMT anode index and (m,n) are the foci index. Scattering matrix coefficients $C_{(a,b),(m,n),k}$ are a set of constant values which are related to the radially integrated PSF (H_0) of the scattered light. $N(a,b,i,j,k)$ follows Poisson statistics $P(I_{MD}) = \frac{I_{MD}^{N} e^{-I_{MD}}}{N!}$. Hence, the log-likelihood function of the readout process can be written as

$$l_S = \sum_{a,b,i,j,k} \left[N(a,b,i,j,k) \ln I_{MD}(a,b,i,j,k) - I_{MD}(a,b,i,j,k) \right] \tag{6.3}$$

The original fluorophores distribution at the corresponding axial depth recorded by MMM system is considered to be initial value for iteration process. So the iteration step for maximum likelihood estimation of fluorophores distribution can be written as

$$\hat{I}^{(k+1)}\left(a,b,i,j,k\right)=\hat{I}^{k}\left(a,b,i,j,k\right)-\frac{\left\{\frac{\partial l_S\left(I,H_0,C,\alpha,k\right)}{\partial I\left(a,b,i,j,k\right)}\right\}_{I(a,b,i,j,k)=\hat{I}^{k}(a,b,i,j,k)}}{\left\{\frac{\partial^2 l_S\left(I,H_0,C,\alpha,k\right)}{\partial^2 I\left(a,b,i,j,k\right)}\right\}_{I(a,b,i,j,k)=\hat{I}^{k}(a,b,i,j,k)}} \tag{6.4}$$

Maximization of likelihood functions with respect to C and α have similar forms. The log-likelihood function is evaluated at each iteration step for maximum likelihood estimation of fluorophores distribution until convergence.

6.2.6 Integration of automated slicing module

Suffered from limited penetration depths into tissue, histological sectioning is the standard approach to obtain 3D reconstructions from large volume specimens. However, it is inevitable to destroy tissue structure or even lose certain specimen during mechanical cutting. Furthermore, various orientations of tissue slices placed on glass slides increase the difficulty in image post-processing for 3D reconstruction. Hence, In order to image large volume tissue samples, it is better to run the whole system automatically with a slicing module, so that we can do imaging, slicing and imaging again repeatedly until the entire tissue block is completed, while the specimen orientation stays the same and its surface parallels with focal plane during the whole procedure. Figure 6.3 illustrates the automated image-slice-image procedure with a complemented slicing module. Adjusted by piezo on objective lens, 50 µm of sample block surface is scanned at the beginning. Then the sample block is lowered to cutting height. After being sliced off the top 30 µm, the sample block is up back to imaging height for the next scanning. In this case, there will be 20 µm-depth overlap between two images to ensure image completeness. Besides, the automation of imaging and slicing can improve the whole system's efficiency and reduce manual labor.

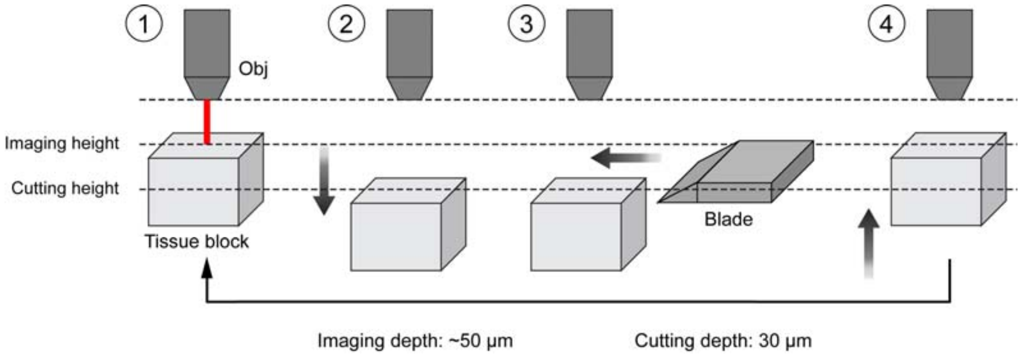

Figure 6.3 Illustration of automated image-slice-image procedure. 1) Scan 50 µm of tissue block surface at imaging height. 2) Lower the tissue block to cutting height. 3) Cut off the first 30 µm of tissue block. 4) Rise tissue block back to imaging height for the next scanning.

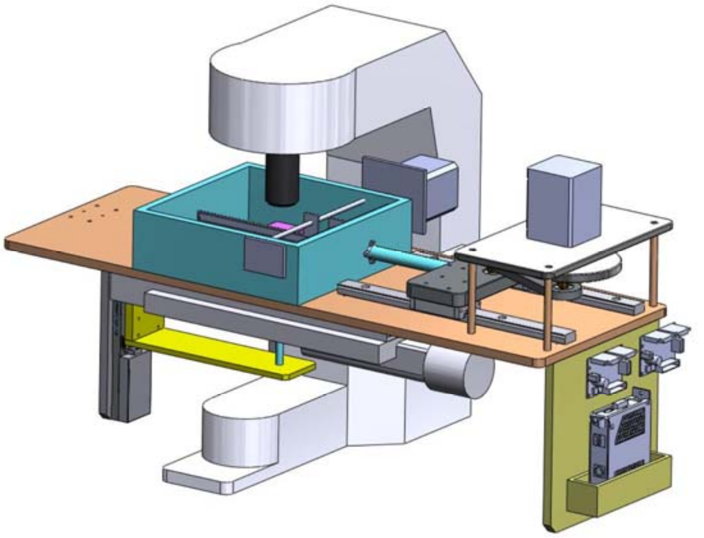

Figure 6.4 Design of automated slicing module. The module is mounted on existing X-Y motorized stage. A water tank (green) is placed at center to make the slicing performed under water due to the water-immersion objective lens. A 1D translation stage is installed under the water tank to adjust height of tissue block.

Figure 6.4 shows the design of the automated slicing module for slicing a biological tissue sample encased in a paraffin block (40×40×20 mm). This slicing module is attached to the existing X-Y motorized stage which is mounted on the MMM microscope frame. Considering the objective lens is water immersion, the slicing will be performed inside a water tank. A single-track translation stage with 0.1 µm resolution is placed under tissue block to adjust its height for scanning and cutting.

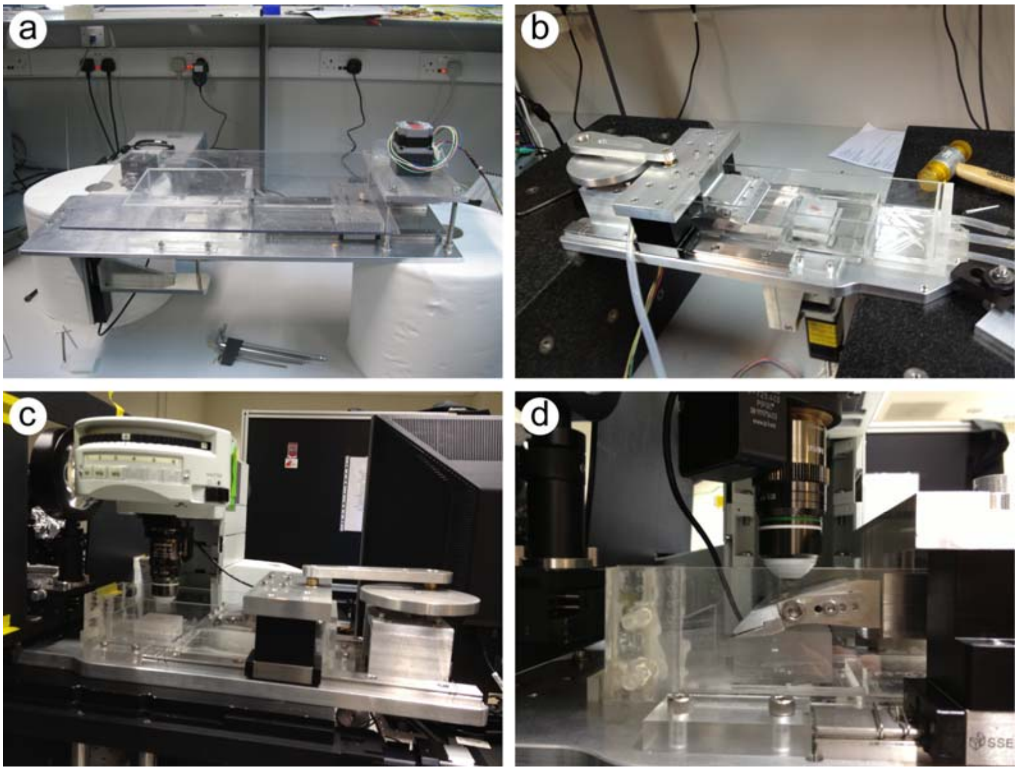

Figure 6.5 Prototype of automated slicing module. Compared to the first generation (a), the slicing module of second generation (b) is more stable by using a metal block to support blade instead of a thin slicing rob, has a larger water tank and a water pump to clear sample chips around objective lens. The modified version of slicing module is more compact to fit the microscope (c)(d).

Figure 6.5 shows the prototype of customized automated slicing module. Figure 6.5(a) is the first generation product made according to original design (Figure 6.4). In this design, blade is mounted on a long slicing rod which connects to a stepper motor. The water tank is a relatively small cube to contain tissue block and the blade only. However, the slicing rod is too long and thin to provide a stable cutting and easy to cause deviation on slicing thickness. Besides, chips of sample from cutting float around inside water tank, affecting subsequent scans. Hence, the second generation of slicing module has been designed and built up to overcome the drawbacks. In the modified design (Figure 6.5(b)), the blade is mounted on a metal block instead of a slicing rod to improve its cutting stability. The water tank is expanded to a rectangular shape. On the other side away from stepper motor, the tank is connecting with a water pump to make the sample chips flow with water to the side, ensuring scanning proceeds in clean water. In addition, the whole module is more compact to fit the microscope compared to the first generation, as shown in Figure 6.5(c)(d).

6.3 Results and discussions

6.3.1 Dark noise and image uniformity

Dark noise is the signal that system received from pure outside and ideally it is only dark current which is the relatively small electric current that flows through photosensitive devices such as PMT even when no photons are entering the device. But in reality there are still photons coming from environment and exist all the time. Dark noise measurement would reveal the background noise level and based on it useful signal during experiments can be extracted.

The function of discriminators is to amplify imaging signal and reduce background noise. Therefore, it is very important to set appropriate noise reference before any experiments so that basic background noise is filtered but sensitivity to low signal is maintained. In particular when MMM has 64 independent discriminator channels, their noise reference should be set the same to ensure the whole image uniformity. Dark noise adjustment was carried out in the following conditions:

1) The lights in the room were off and the system was wrapped up by black board to prevent outside light entering MAPMT;
2) Laser was off so that no imaging signals were detected;
3) All the electronic parts were on, including Xilinx FPGA controlling board, discriminators, scanners and all power supplies because current noise is the main reason for dark noise and it cannot be avoided during any experiments.

Under the above conditions, the amplifier was adjusted on the discriminator board for each channel until there was no more than one photon shown in every pixel. Figure 6.6 shows the dark noise after setting. From the whole image, all 64 sub-regions are uniform that no clear boundaries displayed. Photon numbers in each pixel along the fourth column and fourth row (indicated by yellow lines) are either 0 or 1 and basically distribute evenly. On this dark noise basis, photons obtained during experiments are considered as imaging signals.

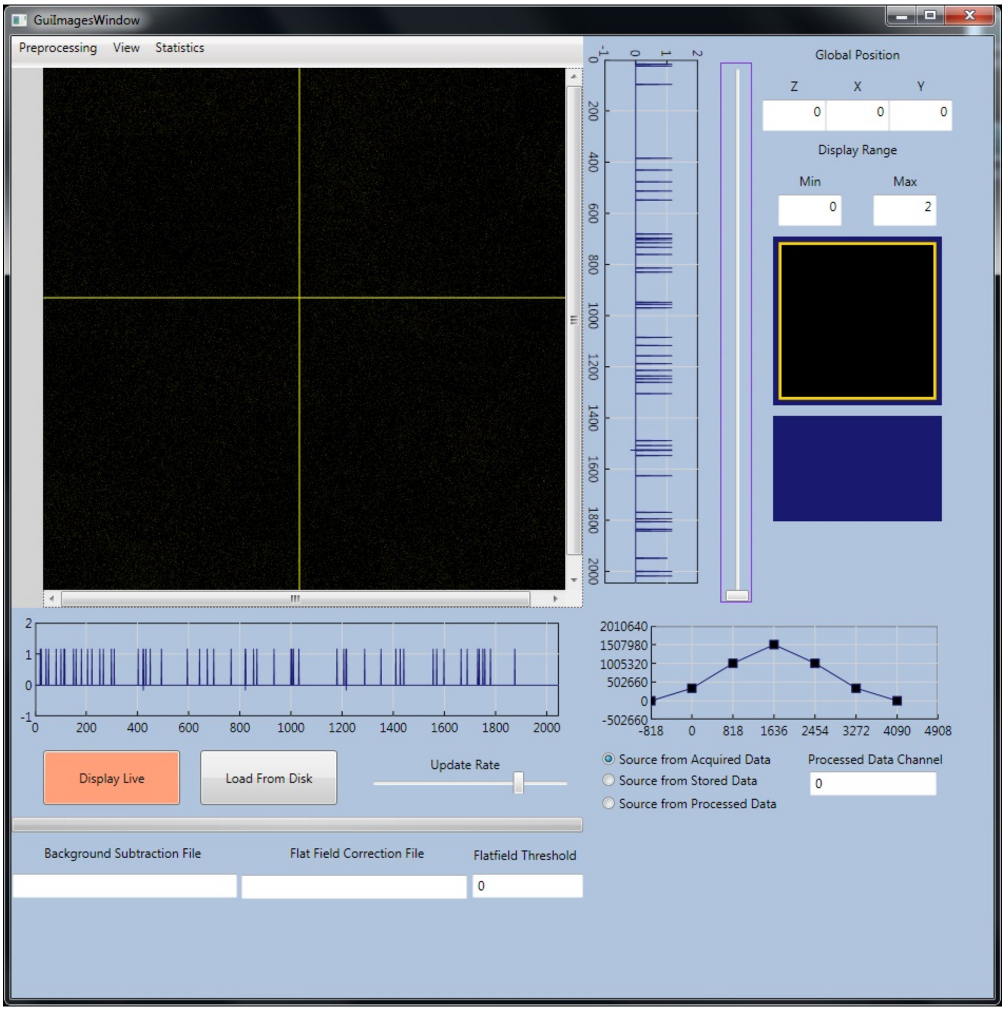

Global Position
Z 0
X 0
Y 0

Display Range
Min 0
Max 2

● Source from Acquired Data
○ Source from Stored Data
○ Source from Processed Data

Processed Data Channel: 0

Background Subtraction File:
Flat Field Correction File:
Flatfield Threshold: 0

Figure 6.6 Dark noise set by adjusting noise reference through discriminator amplifier under the condition that the system was wrapped up with black board to prevent outside light, the laser was off and all the electronic parts were running due to unavoidable current noise. 64 channels were adjusted independently to no more than one photon in every pixel and kept the noise level uniformly.

Even though every sub-region is set on the same reference, the detected signal quality and intensity varies between channels. The sub-region uniformity to imaging signals was tested by 355 µM fluorescein solution and the result is indicated in Figure 6.7. Photon numbers at right side and bottom reflect the intensity distribution of the third column and the sixth row. Signals at image center are the strongest and the intensity gradually weakens along the radius from the center. The sub-regions at four corners are the weakest. Signals at side are about 30% weaker than at center. Nonuniformity of beamlets split by DOE contributes to this result. Another contributing factor is that transmission efficiency on an optical lens is not even. For a beam, the further away from the lens center, more aberration occurs that weakens the signal intensity and resolution. The intensity difference between neighbor sub-regions is caused by sensitivity variety of discriminator channels.

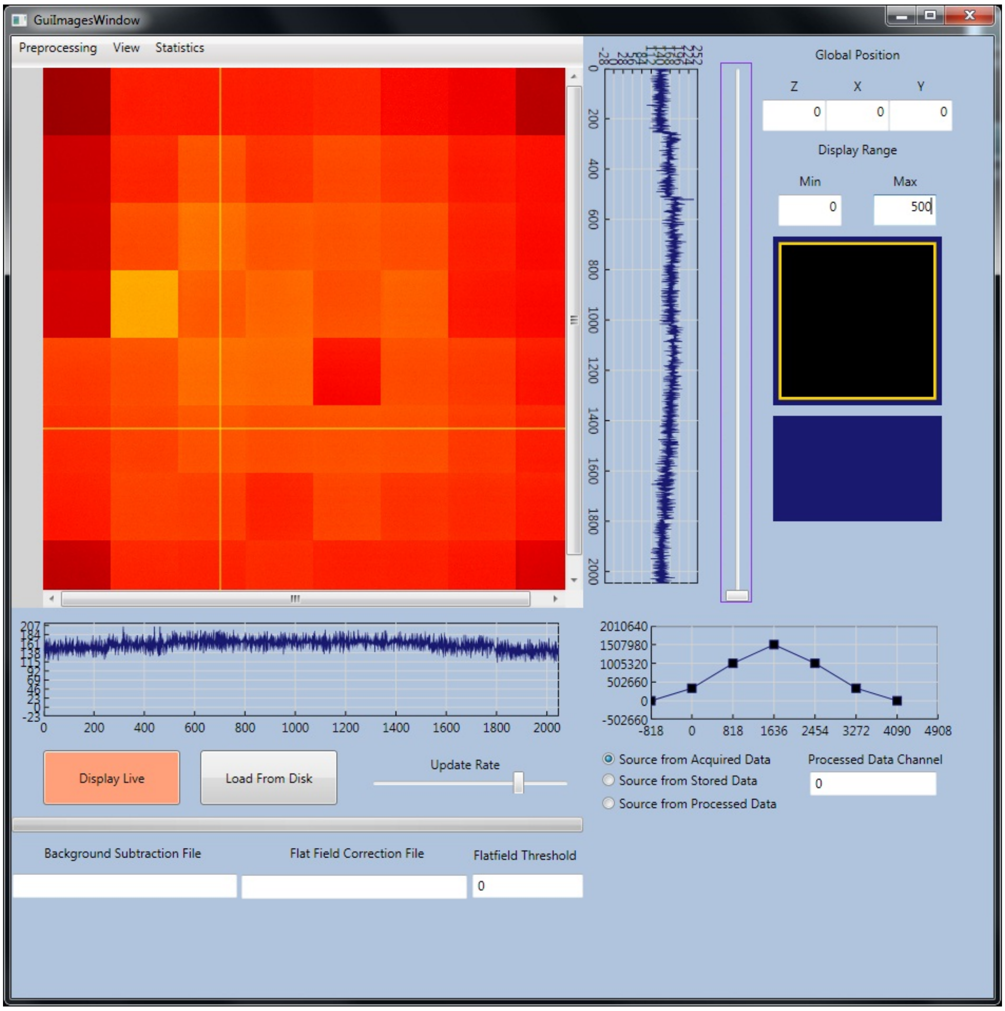

Global Position

Z 0 X 0 Y 0

Display Range

Min 0 Max 500

● Source from Acquired Data
○ Source from Stored Data
○ Source from Processed Data

Processed Data Channel 0

Flatfield Threshold 0

Figure 6.7 Image uniformity by scanning fluorescein solution with concentration of 355 µM. Photon numbers shown at right side and bottom indicate sub-regions at centers. Sensitivity varies between 64 channels.

6.3.2 Measurement of pixel size

Scanning resolution and steps can be chosen from the software due to different applications and purposes. Pixel size at different scanning mode needs to be measured to make sure appropriate step number is set so that every sub-region can connect well with each other to form a complete image. As explained in section 6.2.2, a 600lp/mm Ronchi rulings slide filled with 1.775 mM fluorescein solution was utilized to measure pixel size.

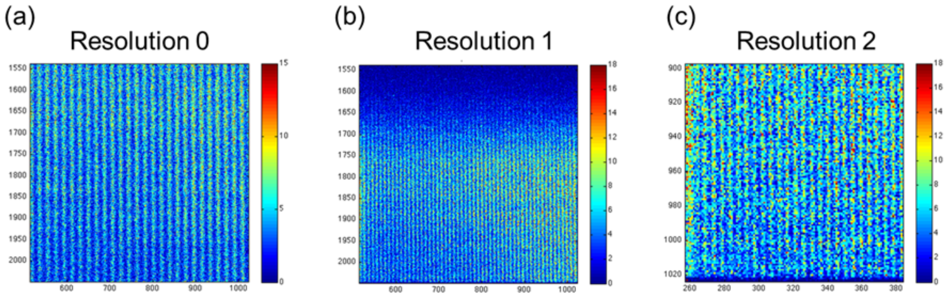

Figure 6.8 Pixel size measurement at different scanning resolution modes. Resolution 0 has the smallest pixel size (a), resolution 2 has the largest pixel size (c) and resolution 1 is in between (b). Pixel size can be calculated as dividing one line-pair size (1.667 µm) by pixel number that counted in one line-pair from the image. Scales of x and y are pixel number on the images.

Figure 6.8 shows two-photon images of Ronchi ruling at different scanning resolution modes. Resolution 0 in Figure 6.8(a) has the smallest pixel size while resolution 2 in Figure 6.8(c) has the largest pixel size, and the pixel size of resolution 1 in Figure 6.8(b) is in between. The alternated bright-dark pattern confirms the grating structure on the Ronchi ruling slide. Since resolution 1 has bigger pixel size than resolution 0, a larger sample area was covered over the same pixel numbers. Therefore, the strips look denser for resolution 1 than resolution 0. A smaller image scale was chosen for resolution 2 to better show its pattern even though it has a much denser pattern than resolution 1. Each line-pair size on the Ronchi ruling is about 1.667 µm ($1\text{mm} / 600\text{lp} \approx 1.667\,\mu\text{m}$). To get average pixel size, pixel numbers N

over 30 line-pairs were counted for each resolution, then the pixel size can be calculated by $1.667 \times 30 / N$. After calculation, pixel size for resolution 0 is 0.088 µm, resolution 1 is 0.174 µm and resolution 2 is 0.33 µm. Scanning steps then can be determined because the field of view of each sub-region on specimen is fixed as 46 µm. The detailed settings for different resolution mode are shown in Table 6.2. It is notable that the calculated step numbers are the minimum value to cover a sub-region area. In actual experiments, a larger number should be used because certain overlap between sub-regions is beneficial to preserve complete information from specimen.

Table 6.2 Settings for different resolution mode based on measured pixel size.

Modes	Resolution 0	Resolution 1	Resolution 2
Pixel size (µm)	0.088	0.174	0.33
Min. step number	523	265	140

6.3.3 Fluorescent beads image with different size

Yellow-green fluorescent beads with sizes of 4 µm, 1 µm and 0.5 µm were imaged by MMM TPEF channel to test signal quality and stage stability. Figure 6.9 shows the comparison of a 4 µm bead images taken when the sample was placed on different stages. Imaging setting was resolution 2 and 160 steps. When the beads sample slide was put on a plate stood on a 3D translation stage that fixed with a pillar, the image looks non-uniform because there was very tiny vibration during scanning (Figure 6.9(a)). The stability was much improved after changing to a motorized X-Y stage with a lab jack for Z direction control to find focal plane (Figure 6.9(b)).

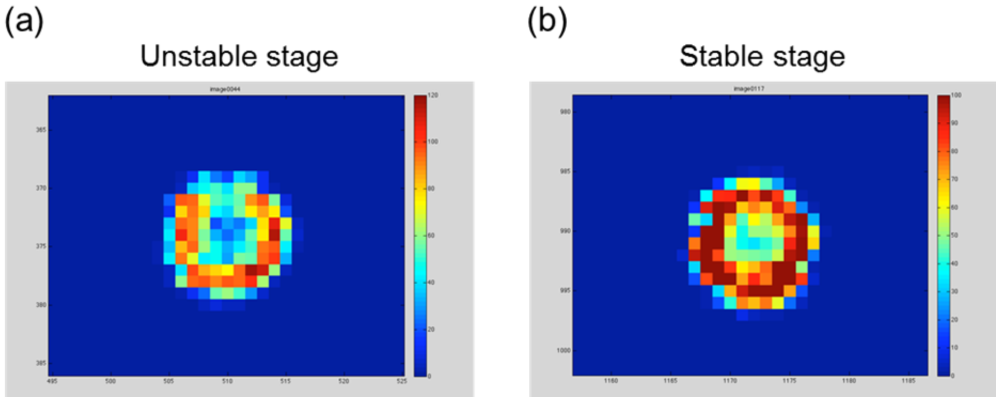

Figure 6.9 4 µm yellow-green fluorescent beads images on different stages. The bead looks non-uniform on a 3D translation stage fixed with a pillar (a) that confirmed to be unstable because there was very tiny vibration during scanning. The bead is round and uniform after improving the stage by using a lab jack (b).

Using the stable stage, 4 µm, 1 µm and 0.5 µm fluorescent beads were scanned under the setting of resolution 1 and 300 steps. Beads images are shown in Figure 6.10. 4 µm beads in Figure 6.10(a)(b)(c) occupy about 25 pixels and confirm the pixel size measurement result that at resolution 1 pixel size is 0.17 µm. The outer ring of the beads is brighter than inside because the fluorescent dye could not go deeper into the beads from surfaces. 1 µm beads in Figure 6.10(d)(e)(f) occupy about 6 to 7 pixels and 0.5 µm beads in Figure 6.10(g)(h)(i) occupy about 4 to 5 pixels. They all match the pixel size measurement previously. Signal intensities are much higher than background no matter what size of the bead is.

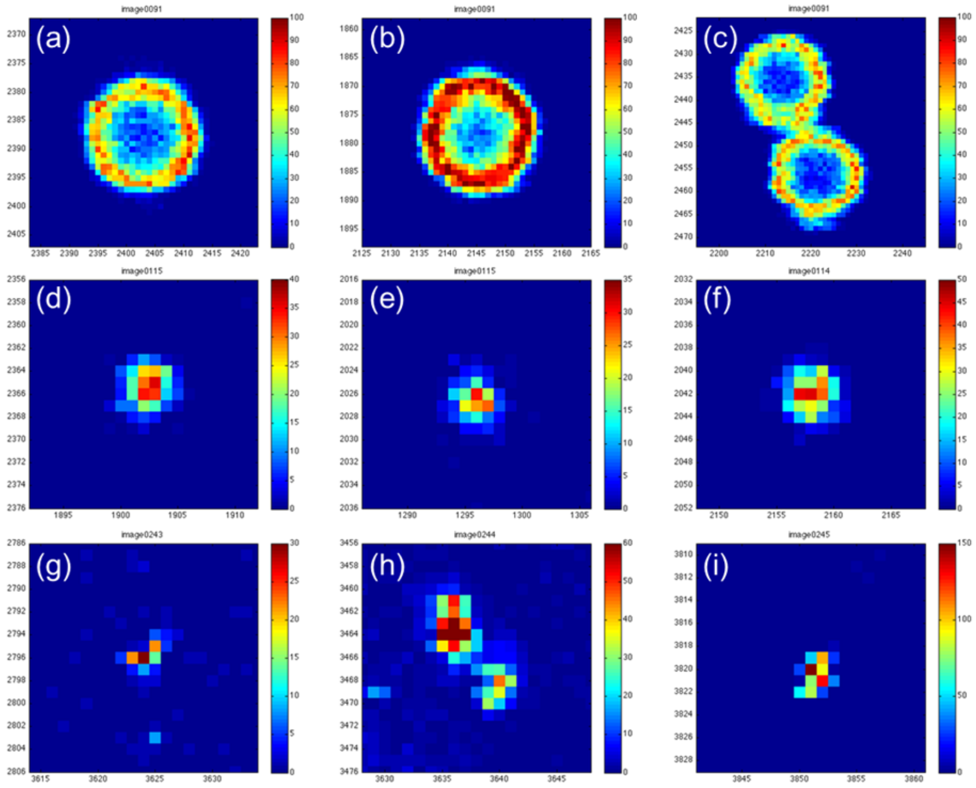

Figure 6.10 Images of yellow-green fluorescent beads at size of 4 µm (a)(b)(c), 1 µm (d)(e)(f) and 0.5 µm (g)(h)(i). Images were taken by MMM TPEF channel and imaging setting was resolution 1 and 300 steps.

6.3.4 Measurement of optical resolution

Optical resolution describes the limit distance between two distinguishable radiating points. As introduced earlier, the intensity in space near the focus is described by the illumination point spread function, $\mathrm{PSF}(x,y,z)$, and PSF^2 is used to define the true optical resolution in multiphoton microscopy [79], as shown in Figure 6.11. It can be calculated by fitting the lateral and axial intensity-squared profiles to a Gaussian function $f(x)=a\exp\left(-\frac{(x-b)^2}{2c^2}\right)+d$, where a, b, c and d are all real constants.

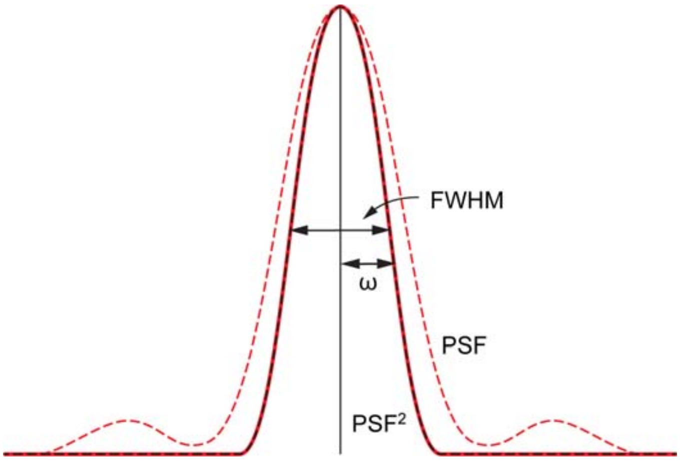

Figure 6.11 PSF (dashed red line) and PSF^2 (solid red line). Dashed black line is a fit to Gaussian function.

Then, theoretical lateral and axial resolution can be expressed by

$$\omega_{xy}=\begin{cases}\dfrac{0.320\lambda}{\sqrt{2}\mathrm{NA}} & \mathrm{NA}\le 0.7\\ \dfrac{0.325\lambda}{\sqrt{2}\mathrm{NA}^{0.91}} & \mathrm{NA}>0.7\end{cases}, \tag{6.5}$$

and

$$\omega_z=\frac{0.532\lambda}{\sqrt{2}}\left[\frac{1}{n-\sqrt{n^2-\mathrm{NA}^2}}\right] \tag{6.6}$$

Therefore, for our specific MMM system with 780 nm laser and 1.05 NA water immersion objective lens, the theoretical lateral resolution is $2\omega_{xy} = \frac{2\times 0.325\times 0.78}{\sqrt{2}\times 1.05^{0.91}} \approx 0.3429$ µm and axial resolution is

$2\omega_{z} = \frac{2\times 0.532\times 0.78}{\sqrt{2}}\left[\frac{1}{1.33-\sqrt{1.33^2-1.05^2}}\right] \approx 1.1425$ µm.

In practice, the common way to determine the resolution of an optical system is to measure the FWHM of the PSF^2 in two-photon system. It can be calculated based on the parameter c in Gaussian function according to

$$\mathrm{FWHM} = 2\sqrt{2\ln 2}\,c \approx 2.35482\,c \tag{6.7}$$

Figure 6.12(a) is an image of a 0.1 µm yellow-green fluorescent bead which is chosen for analysis. Among a series of z-stack images with 0.1 µm interval distance in z-direction, the bead in this specific image has the largest dimension and intensity so that we can consider it is the center plane of the bead. Pick a line that passes the center of the bead in Figure 6.12(b) and extract intensity of each pixel. Fit the squared intensities into Gaussian function to calculate its FWHM as the lateral optical resolution of MMM system using Matlab. The fitting curve is shown in Figure 6.12(d) and the calculated FWHM is 0.3240 µm. To study the axial resolution, focus on the center pixel of the bead and extract the intensities of the same pixel in all z-stack images, fit them to Gaussian function. The fitting curve is shown in Figure 6.12(c) and the calculated FWHM is 1.3003 µm.

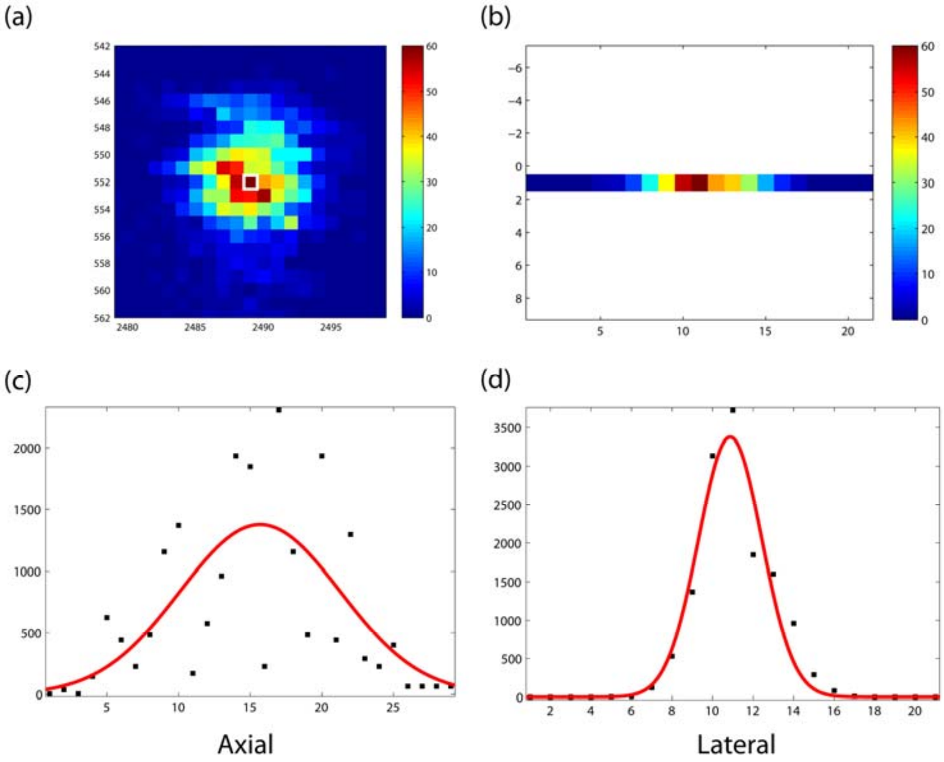

Figure 6.12 Optical resolution on axial and lateral direction from imaging a 0.1 µm fluorescent bead. A line (b) that passes the center of the bead (a) is chosen and fitted squared-intensities into Gaussian function (d) whose FWHM (i.e. lateral resolution) is 0.3240 µm. The intensities of center pixel of the bead (white square in (a)) in all z-stack images are extracted to calculate axial resolution (c) which is 1.3003 µm.

The measured lateral optical resolution is slightly smaller than theoretical value. It can be adequately explained that the image shown in Figure 6.12(a) is not exactly its center plane, resulting in the narrower of the fitting curve than it is supposed to be.

6.3.5 Imaging and image processing of liver samples

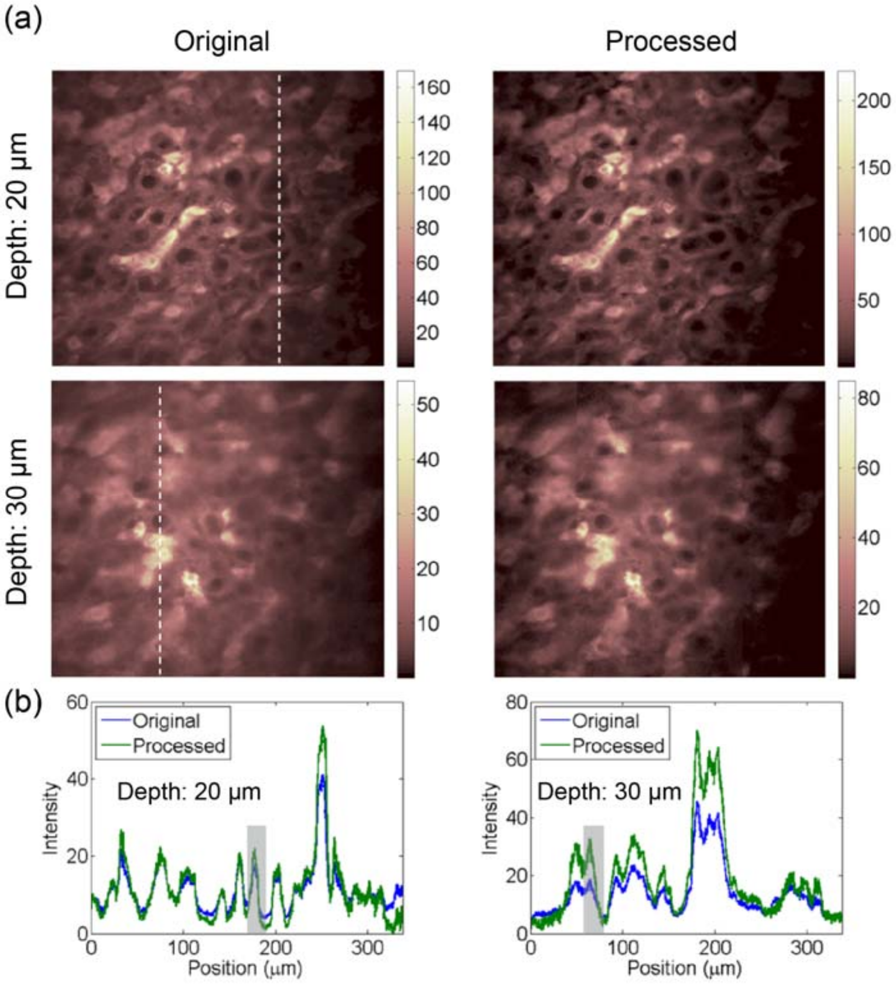

Figure 6.13 Fibrotic liver images by the MMM system. (a) Left acquired images at 20 µm and 30 µm imaging depths, and right are the corresponding processed images. (b) Intensity line plots for original and processed images for imaging depths 20 µm and 30 µm respectively.

Figure 6.13(a) shows the original MMM image and the processed image of the liver tissue sample at 20 µm and 30 µm imaging depths. They demonstrate that MMM is able to visualize clear liver cells and tissue structure. Comparing images at 20 µm depth and 30 µm depth, it is obvious that the deeper the blurring the images are. It is due to the fact that there are more scattering events when the photons travel a longer distance in the tissue. Ghost image in MMM are not so prominent because for the dense features scattering mainly generate a relatively uniform background haze at the neighboring anodes. In this case, the proposed method suppresses the photons in uniform background haze and reassigns them to original anode location. Figure 6.13(b) shows the intensity line plots for both imaging depths. It can be clearly observed that for the processed images the background noise is suppressed and image features are extracted with better signal strength. Contrast of the features, highlighted in Figure 6.13(b) at the imaging depths 20 µm and 30 µm, is calculated for the original and processed image. The quantitative comparison of contrast is shown in Table 6.3. Clearly, the maximum likelihood estimation method improves the contrast of features; this is essentially because of the improvement in signal strength of the image features concurrently suppressing the background haze at the respective anode, and therefore the available image photons are utilized more effectively.

Table 6.3 Contrast comparison of original and processed liver images for imaging depths 20 µm and 30 µm.

Depth (µm)	Original	Processed
20	0.62	0.87
30	0.54	0.81

6.4 Conclusions

The characteristics and improvement of the new MMM-SHG system were investigated for the study of liver fibrosis. The pixel sizes for different scanner settings were measured by Ronchi ruling slide that the smallest step size is 0.088 µm; while the other step sizes are times of the smallest one, such as 0.174 µm, 0.33 µm, ... Yellow-green fluorescent beads at different sizes from 0.1 µm to 4 µm were visualized and 0.1 µm beads were used for optical resolution measurement. The measured lateral resolution 0.3240 µm and axial resolution 1.3003 µm were pretty close to the theoretical values 0.3429 µm and 1.1425 µm respectively. It illustrates that the multifocal scanning would enhance the imaging speed, but would not affect imaging resolution. Due to the usage of MAPMT and high scattering of liver samples, image ghost generated when emission photons entered wrong anodes of detector. To remove the ghost and increase SNR, a post-processing method based on maximum likelihood estimation was developed and the contrast of processed liver images was clearly improved. Moreover, to realize the application of MMM on large tissue sample imaging, an automated slicing module was designed, produced and coupled into the system for an imaging-slicing-imaging procedure. It can not only reduce labor work on mechanical cutting, but also provide convenience for future 3D reconstruction.

Chapter 7

Conclusions and Future Directions

7.1 Conclusions

This thesis documented the study of liver fibrosis staging using nonlinear microscopy as well as the design, construction and characteristics of a new MMM imaging system to enhance imaging speed for future application in liver fibrosis studies.

Firstly, we validated the improvement of liver fibrosis staging by using the combination of forward and backward SHG signals into one index. A rat fibrosis model was established as an animal study platform, and tissue level imaging was applied. Both forward and backward SHG signals were collected from liver tissue samples at different fibrotic stages which were classified by conventional "gold standard" histopathological scoring system. We demonstrated the feasibility of monitoring liver fibrosis progression by quantifying collagen content percentage of forward SHG, collagen content percentage of backward

SHG and average intensity ratio of forward to backward SHG signals. Furthermore, a better index was created by using SVM classification method to combine these three features together for fibrosis assessment. It efficiently improved fibrosis diagnosis in future applications.

Secondly, we developed a novel descanned dual channel MMM with both TPEF and SHG modalities to increase imaging speed. By using a DOE with high transmittance and uniformity to generate an 8×8 array of foci, the system is able to image the specimen 64 times faster than conventional TPEF/SHG microscopy. To reduce the crosstalk between foci resulted from high scattering specimens, an MAPMT with 64 individual anodes was utilized to detect signals from 64 foci respectively. Besides design of optics, we also developed in-house 64-channel discriminators for signal acquisition and software to control the whole system. In summary, the advantages of the new integrated MMM and SHG system include: 1) 64-time faster imaging speed; 2) Ability to obtain TPEF and SHG signals synchronously; 3) Combination of DOE and MAPMT for high performance; 4) Possibility for 3D visualization of large tissue volume, even a whole organ.

Last but not least, to incorporate the MMM into future liver fibrosis study, we tested the specifications of the new system and developed an image post-processing method and a customized automated slicing module for the new MMM system. The system was validated to have good uniformity and resolution by applying various samples including fluorescein solution, coumarin 1 solution, Ronchi ruling slide, fluorescent beads of different sizes to test system uniformity, measure pixel size and lateral and axial optical resolution. We established an image post-processing method based on maximum likelihood estimation to remove ghost images and increase SNR from original images. Moreover, we developed and implemented an automated slicing module into the MMM system to realize an imaging-slicing-imaging procedure so that no loss of tissue information during mechanical sectioning and future 3D reconstruction would be easily performed.

7.2 Recommendations for further work

7.2.1 Establish fibrosis assessment index for MMM system

Due to different sensitivity among 64 anodes on MAPMT and unavoidable non-uniformity between center foci and edge foci, the characteristics of liver images from MMM system are not identical with conventional multiphoton microscopy, although imaging resolution of

MMM is as high as conventional one. Therefore, additional imaging processing algorithms should be developed and applied before extracting features from images. For example, compensation should be made to homogenize the raw image so that there will not be signal loss by any filtering actions during image processing. Besides, segmentation methods for collagen analysis should be re-evaluate to find a proper one for MMM images. Moreover, the main purpose of building MMM with automated slicing module is to scan large volume tissue block in 3D. Hence, algorithms on 3D reconstruction and analysis should be developed.

7.2.2 Study morphological changes of bridging in fibrosis progression

For current liver fibrosis diagnosis, biopsy with subsequent histo-pathological evaluation is still the gold standard method to assess its severity [25, 35]. Several grading and scoring systems have been developed and all of them are based on three conceptual fibrosis stages, including portal fibrosis, bridging fibrosis and cirrhosis [27-29]. The occurrence of fibrosis bridging is considered to be closer to end-stage fibrosis. It begins in portal tracts, spreads and connects to other areas that contain fibrosis (portal-to-portal, portal-to-central), forming a "bridge". However, limited information is available for its morphology and progression in 3D. It is notable that in Metavir scoring system, stage 3 is defined as "numerous bridges or septa", indicating that it might be a collagen sheet in space [27]. But no promising 3D images have shown proof for this concept, even though a few studies have been working on it [117, 118]. Therefore, we hypothesize that bridging fibrosis is a two-dimensional representation of a three-dimensional membrane of fibrosis (Figure 7.1(a)). It is important to prove the hypothesis and further quantitatively investigate that how the membrane forms.

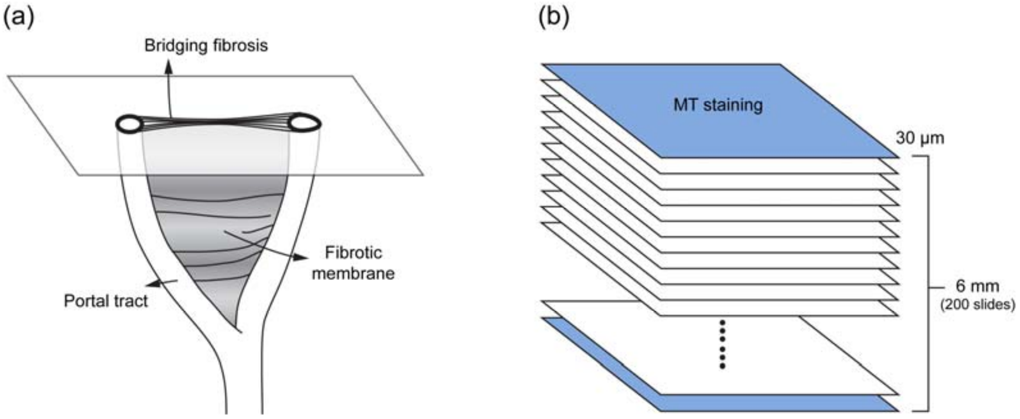

Figure 7.1 3D reconstruction of hepatic bridging fibrosis with MMM-SHG-Slicing system to validate the hypothesis that the bridging fibrosis is sections of fibrotic membranes (a). MMM-SHG-Slicing system is able to provide 3D information by scanning a 6 mm thick liver tissue block and compare the results with traditional MT staining (b).

Fibrotic animal models should be established as there are different tissue structure and collagen features in late stages. Liver fibrosis can be induced in both BDL and drug induction (such as TAA) methods for comparison. Livers can be extracted at different time points from sacrificed animals and paraffinized. With the automated slicing module, the tissue block of 6 mm in height can be entirely imaged by MMM system (Figure 7.1(b)) and reconstructed into a 3D liver atlas.

Bibliography

1. Bataller, R. and D.A. Brenner, *Liver fibrosis.* Journal of Clinical Investigation, 2005. **115**(2): p. 209-18.

2. Friedman, S.L., *Molecular regulation of hepatic fibrosis, an integrated cellular response to tissue injury.* Journal of Biological Chemistry, 2000. **275**(4): p. 2247-50.

3. Friedman, S.L., *Liver fibrosis -- from bench to bedside.* Journal of Hepatology, 2003. **38 Suppl 1**: p. S38-53.

4. Gutierrez-Ruiz, M.C. and L.E. Gomez-Quiroz, *Liver fibrosis: searching for cell model answers.* Liver International, 2007. **27**(4): p. 434-439.

5. Afdhal, N.H. and D. Nunes, *Evaluation of liver fibrosis: A concise review.* American Journal of Gastroenterology, 2004. **99**(6): p. 1160-1174.

6. Assy, N. and G.Y. Minuk, *Serum aspartate but not alanine aminotransferase levels help to predict the histological features of chronic hepatitis C viral infections in adults.* American Journal of Gastroenterology, 2000. **95**(6): p. 1545-1550.

7. Walsh, K.M., et al., *Basement membrane peptides as markers of liver disease in chronic hepatitis C.* Journal of Hepatology, 2000. **32**(2): p. 325-330.

8. Kanzler, S., et al., *Prediction of progressive liver fibrosis in hepatitis C infection by serum and tissue levels of transforming growth factor-beta.* Journal of Viral Hepatitis, 2001. **8**(6): p. 430-437.

9. George, D.K., et al., *Elevated serum type IV collagen: a sensitive indicator of the presence of cirrhosis in haemochromatosis.* Journal of Hepatology, 1999. **31**(1): p. 47-52.

10. Lee, H.S., et al., *Optical biopsy of liver fibrosis by use of multiphoton microscopy.* Optics Letters, 2004. **29**(22): p. 2614-2616.

11. Sun, W., et al., *Nonlinear optical microscopy: use of second harmonic generation and two-photon microscopy for automated quantitative liver fibrosis studies.* Journal of Biomedical Optics, 2008. **13**(6): p. 064010.

12. Kim, K.H., et al., *Multifocal multiphoton microscopy based on multianode photomultiplier tubes.* Optics Express, 2007. **15**(18): p. 11658-78.

13. Bewersdorf, J., R. Pick, and S.W. Hell, *Multifocal multiphoton microscopy.* Optics Letters, 1998. **23**(9): p. 655-7.

14. Maton, A., *Human Biology and Health.* 1993, Englewood Cliffs, NJ.: Prentice Hall.

15. Frantz, C., K.M. Stewart, and V.M. Weaver, *The extracellular matrix at a glance.* Journal of Cell Science, 2010. **123**(Pt 24): p. 4195-200.

16. Benyon, R.C. and J.P. Iredale, *Is liver fibrosis reversible?* Gut, 2000. **46**(4): p. 443-6.

17. Arthur, M.J., *Matrix degradation in liver: a role in injury and repair.* Hepatology, 1997. **26**(4): p. 1069-71.

18. Gosnell, J.E., et al., *Extracellular matrix regulates the hepatocellular heat shock response.* Journal of Surgical Research, 2000. **91**(1): p. 43-9.

19. Nakagawa, T., et al., *Role of ERK1/2 and p38 mitogen-activated protein kinases in the regulation of thrombospondin-1 by TGF-beta1 in rat proximal tubular cells and mouse fibroblasts.*

Journal of the American Society of Nephrology, 2005. **16**(4): p. 899-904.

20. Ricard-Blum, S. and F. Ruggiero, *The collagen superfamily: from the extracellular matrix to the cell membrane.* Pathologie Biologie (Paris), 2005. **53**(7): p. 430-42.

21. Arriazu, E., et al., *Extracellular matrix and liver disease.* Antioxidants & Redox Signaling, 2014. **21**(7): p. 1078-97.

22. Hahn, E., et al., *Distribution of basement membrane proteins in normal and fibrotic human liver: collagen type IV, laminin, and fibronectin.* Gut, 1980. **21**(1): p. 63-71.

23. Rojkind, M., M.A. Giambrone, and L. Biempica, *Collagen types in normal and cirrhotic liver.* Gastroenterology, 1979. **76**(4): p. 710-9.

24. Tsukada, S., C.J. Parsons, and R.A. Rippe, *Mechanisms of liver fibrosis.* Clinica Chimica Acta, 2006. **364**(1-2): p. 33-60.

25. Perrault, J., et al., *Liver biopsy: complications in 1000 inpatients and outpatients.* Gastroenterology, 1978. **74**(1): p. 103-6.

26. Goodman, Z.D., *Grading and staging systems for inflammation and fibrosis in chronic liver diseases.* Journal of Hepatology, 2007. **47**(4): p. 598-607.

27. Bedossa, P. and T. Poynard, *An algorithm for the grading of activity in chronic hepatitis C. The METAVIR Cooperative Study Group.* Hepatology, 1996. **24**(2): p. 289-93.

28. Knodell, R.G., et al., *Formulation and application of a numerical scoring system for assessing histological activity in asymptomatic chronic active hepatitis.* Hepatology, 1981. **1**(5): p. 431-5.

29. Ishak, K., et al., *Histological grading and staging of chronic hepatitis.* Journal of Hepatology, 1995. **22**(6): p. 696-9.

30. Manning, D.S. and N.H. Afdhal, *Diagnosis and quantitation of fibrosis.* Gastroenterology, 2008. **134**(6): p. 1670-81.

31. Poniachik, J., et al., *The role of laparoscopy in the diagnosis of cirrhosis.* Gastrointestinal Endoscopy, 1996. **43**(6): p. 568-71.

32. Pagliaro, L., et al., *Percutaneous blind biopsy versus laparoscopy with guided biopsy in diagnosis of cirrhosis. A prospective, randomized trial.* Digestive Diseases and Sciences, 1983. **28**(1): p. 39-43.

33. Maharaj, B., et al., *Sampling variability and its influence on the diagnostic yield of percutaneous needle biopsy of the liver.* the Lancet, 1986. **1**(8480): p. 523-5.

34. Schlichting, P., B. Holund, and H. Poulsen, *Liver biopsy in chronic aggressive hepatitis. Diagnostic reproducibility in relation to size of specimen.* Scandinavian Journal of Gastroenterology, 1983. **18**(1): p. 27-32.

35. Holund, B., H. Poulsen, and P. Schlichting, *Reproducibility of liver biopsy diagnosis in relation to the size of the specimen.* Scandinavian Journal of Gastroenterology, 1980. **15**(3): p. 329-35.

36. Regev, A., et al., *Sampling error and intraobserver variation in liver biopsy in patients with chronic HCV infection.* American Journal of Gastroenterology, 2002. **97**(10): p. 2614-8.

37. Imbert-Bismut, F., et al., *Biochemical markers of liver fibrosis in patients with hepatitis C virus infection: a prospective study.* the Lancet, 2001. **357**(9262): p. 1069-75.

38. Forns, X., et al., *Identification of chronic hepatitis C patients without hepatic fibrosis by a simple predictive model.* Hepatology, 2002. **36**(4 Pt 1): p. 986-92.

39. Sacconi, L., et al., *Cell imaging and manipulation by nonlinear optical microscopy.* Cell Biochemistry and Biophysics, 2006. **45**(3): p. 289-302.

40. Benninger, R.K., M. Hao, and D.W. Piston, *Multi-photon excitation imaging of dynamic processes in living cells and tissues.* Reviews of Physiology, Biochemistry & Pharmacology, 2008. **160**: p. 71-92.

41. Pawley, J., *Handbook of Biological Confocal Microscopy.* 2010: Springer.

42. Boyd, R.W., *Nonlinear Optics.* 2008: Elsevier Science.

43. Göppert - Mayer, M., *Über elementarakte mit zwei quantensprü ngen.* Annalen der Physik, 1931. **401**(3): p. 273-294.

44. Abella, I.D., *Optical double-photon absorption in cesium vapor.* Physical Review Letters, 1962. **9**(11): p. 453-&.

45. So, P.T., et al., *Two-photon excitation fluorescence microscopy.* Annual Review of Biomedical Engineering, 2000. **2**: p. 399-429.

46. Helmchen, F. and W. Denk, *Deep tissue two-photon microscopy.* Nature Methods, 2005. **2**(12): p. 932-40.

47. Diaspro, A. and M. Robello, *Two-photon excitation of fluorescence for three-dimensional optical imaging of biological structures.* Journal of Photochemistry and Photobiology B, 2000. **55**(1): p. 1-8.

48. LaComb, R., et al., *Phase matching considerations in second harmonic generation from tissues: Effects on emission directionality, conversion efficiency and observed morphology.* Optics Communications, 2008. **281**(7): p. 1823-1832.

49. Araya, R., et al., *The spine neck filters membrane potentials.* Proceedings of the National Academy of Sciences of the United States of America, 2006. **103**(47): p. 17961-6.

50. Majewska, A.K., J.R. Newton, and M. Sur, *Remodeling of synaptic structure in sensory cortical areas in vivo.* The Journal of Neuroscience, 2006. **26**(11): p. 3021-9.

51. Nishimura, N., et al., *Targeted insult to subsurface cortical blood vessels using ultrashort laser pulses: three models of stroke.* Nature Methods, 2006. **3**(2): p. 99-108.

52. Jain, R. and W. Weninger, *Shedding light on cutaneous innate immune responses: the intravital microscopy approach.* Immunology and Cell Biology, 2013. **91**(4): p. 263-70.

53. Shakhar, G., et al., *Stable T cell-dendritic cell interactions precede the development of both tolerance and immunity in vivo.* Nature Immunology, 2005. **6**(7): p. 707-714.

54. Cavanagh, L.L., et al., *Activation of bone marrow-resident memory T cells by circulating, antigen-bearing dendritic cells.* Nature Immunology, 2005. **6**(10): p. 1029-37.

55. Boissonnas, A., et al., *In vivo imaging of cytotoxic T cell infiltration and elimination of a solid tumor.* Journal of Experimental Medicine, 2007. **204**(2): p. 345-56.

56. Dong, J., et al., *Multiphoton in vivo imaging of amyloid in animal models of Alzheimer's disease.* Neuropharmacology, 2010. **59**(4-5): p. 268-75.

57. Nemet, B.A., V. Nikolenko, and R. Yuste, *Second harmonic imaging of membrane potential of neurons with retinal.* Journal of Biomedical Optics, 2004. **9**(5): p. 873-81.

58. Han, X., et al., *Second harmonic properties of tumor collagen: determining the structural relationship between reactive stroma and healthy stroma.* Optics Express, 2008. **16**(3): p. 1846-59.

59. Theodossiou, T.A., et al., *Second harmonic generation confocal microscopy of collagen type I from rat tendon cryosections.* Biophysical Journal, 2006. **91**(12): p. 4665-77.

60. Strupler, M., et al., *Second harmonic imaging and scoring of collagen in fibrotic tissues.* Optics Express, 2007. **15**(7): p. 4054-65.

61. Kirkpatrick, N.D., M.A. Brewer, and U. Utzinger, *Endogenous optical biomarkers of ovarian cancer evaluated with multiphoton microscopy.* Cancer Epidemiology, Biomarkers & Prevention, 2007. **16**(10): p. 2048-57.

62. Conklin, M.W., et al., *Aligned Collagen Is a Prognostic Signature for Survival in Human Breast Carcinoma.* American Journal of Pathology, 2011. **178**(3): p. 1221-1232.

63. Hua, D.Z., et al., *Monitoring the process of pulmonary melanoma metastasis using large area and label-free nonlinear optical microscopy.* Journal of Biomedical Optics, 2012. **17**(6).

64. Banavar, M., et al., *Detection of collagen by second harmonic microscopy as a diagnostic tool for liver fibrosis - art. no. 60891B*, in *Multiphoton Microscopy in the Biomedical Sciences VI*, A. Periasamy and P.T.C. So, Editors. 2006. p. B891-B891.

65. Cox, G., et al., *3-dimensional imaging of collagen using second harmonic generation.* Journal of Structural Biology, 2003. **141**(1): p. 53-62.

66. Tai, D.C., et al., *Fibro-C-Index: comprehensive, morphology-based quantification of liver fibrosis using second harmonic generation and two-photon microscopy.* Journal of Biomedical Optics, 2009. **14**(4): p. 044013.

67. Svoboda, K., et al., *In vivo dendritic calcium dynamics in neocortical pyramidal neurons.* Nature, 1997. **385**(6612): p. 161-5.

68. Padera, T.P., et al., *Conventional and high-speed intravital multiphoton laser scanning microscopy of microvasculature, lymphatics, and leukocyte-endothelial interactions.* Molecular Imaging, 2002. **1**(1): p. 9-15.

69. Roorda, R.D., et al., *Video-rate nonlinear microscopy of neuronal membrane dynamics with genetically encoded probes.* Journal of Neurophysiology, 2004. **92**(1): p. 609-21.

70. Chen, J.L., et al., *Clustered dynamics of inhibitory synapses and dendritic spines in the adult neocortex.* Neuron, 2012. **74**(2): p. 361-73.

71. Ragan, T., et al., *Two-photon tissue cytometry.* Methods in Cell Biology, 2004. **75**: p. 23-39.

72. Kim, K.H., C. Buehler, and P.T. So, *High-speed, two-photon scanning microscope.* Applied Optics, 1999. **38**(28): p. 6004-9.

73. Fan, G.Y., et al., *Video-rate scanning two-photon excitation fluorescence microscopy and ratio imaging with cameleons.* Biophysical Journal, 1999. **76**(5): p. 2412-20.

74. Iyer, V., B.E. Losavio, and P. Saggau, *Compensation of spatial and temporal dispersion for acousto-optic multiphoton laser-scanning microscopy.* Journal of Biomedical Optics, 2003. **8**(3): p. 460-71.

75. Reddy, G.D. and P. Saggau, *Fast three-dimensional laser scanning scheme using acousto-optic deflectors.* Journal of Biomedical Optics, 2005. **10**(6): p. 064038.

76. Zeng, S., et al., *Simultaneous compensation for spatial and temporal dispersion of acousto-optical deflectors for two-dimensional scanning with a single prism.* Optics Letters, 2006. **31**(8): p. 1091-3.

77. Katona, G., et al., *Fast two-photon in vivo imaging with three-dimensional random-access scanning in large tissue volumes.* Nature Methods, 2012. **9**(2): p. 201-8.

78. Cianci, G.C., J. Wu, and K.M. Berland, *Saturation modified point spread functions in two-photon microscopy.* Microscopy Research and Technique, 2004. **64**(2): p. 135-41.

79. Zipfel, W.R., R.M. Williams, and W.W. Webb, *Nonlinear magic: multiphoton microscopy in the biosciences.* Nature Biotechnology, 2003. **21**(11): p. 1369-77.

80. Oron, D., E. Tal, and Y. Silberberg, *Scanningless depth-resolved microscopy.* Optics Express, 2005. **13**(5): p. 1468-76.

81. Zhu, G., et al., *Simultaneous spatial and temporal focusing of femtosecond pulses.* Optics Express, 2005. **13**(6): p. 2153-9.

82. Fittinghoff, D., P. Wiseman, and J. Squier, *Widefield multiphoton and temporally decorrelated multifocal multiphoton microscopy.* Optics Express, 2000. **7**(8): p. 273-9.

83. Sacconi, L., et al., *Multiphoton multifocal microscopy exploiting a diffractive optical element.* Optics Letters, 2003. **28**(20): p. 1918-20.

84. Shao, Y., et al., *Multifocal multiphoton microscopy based on a spatial light modulator.* Applied Physics B, 2013. **107**(3): p. 653-657.

85. Straub, M. and S.W. Hell, *Multifocal multiphoton microscopy: a fast and efficient tool for 3-D fluorescence imaging.* Bioimaging, 1998. **6**(4): p. 177-185.

86. Fujita, K., et al., *Confocal multipoint multiphoton excitation microscope with microlens and pinhole arrays.* Optics Communications, 2000. **174**(1-4): p. 7-12.

87. Kobayashi, M., et al., *Second-harmonic-generation microscope with a microlens array scanner.* Optics Letters, 2002. **27**(15): p. 1324-6.

88. Buist, A.H., et al., *Real time two-photon absorption microscopy using multi point excitation.* Journal of Microscopy (Oxford), 1998. **192**: p. 217-226.

89. Andresen, V., A. Egner, and S.W. Hell, *Time-multiplexed multifocal multiphoton microscope.* Optics Letters, 2001. **26**(2): p. 75-7.

90. Jureller, J.E., H.Y. Kim, and N.F. Scherer, *Stochastic scanning multiphoton multifocal microscopy.* Optics Express, 2006. **14**(8): p. 3406-14.

91. Gong, B., et al., *Nonlinear imaging study of extracellular matrix in chemical-induced, developmental dissecting aortic aneurysm: evidence for defective collagen type III.* Birth Defects Research Part A: Clinical and Molecular Teratology, 2008. **82**(1): p. 16-24.

92. Odin, C., et al., *Orientation fields of nonlinear biological fibrils by second harmonic generation microscopy.* Journal of Microscopy (Oxford), 2008. **229**(Pt 1): p. 32-8.

93. Gorrell, M.D., et al., *Intrahepatic expression of collagen and fibroblast activation protein (FAP) in hepatitis C virus infection.* Advances in Experimental Medicine and Biology, 2003. **524**: p. 235-43.

94. Suzuki, M., et al., *Second harmonic generation microscopy differentiates collagen type I and type III in COPD*, in *Multiphoton Microscopy in the Biomedical Sciences Xii*, A. Periasamy, K. Konig, and P.T.C. So, Editors. 2012.

95. Lacomb, R., O. Nadiarnykh, and P.J. Campagnola, *Quantitative second harmonic generation imaging of the diseased state osteogenesis imperfecta: experiment and simulation.* Biophysical Journal, 2008. **94**(11): p. 4504-14.

96. Nadiarnykh, O., et al., *Alterations of the extracellular matrix in ovarian cancer studied by Second Harmonic Generation imaging microscopy.* BMC Cancer, 2010. **10**: p. 94.

97. Ajeti, V., et al., *Structural changes in mixed Col I/Col V collagen gels probed by SHG microscopy: implications for probing stromal alterations in human breast cancer.* Biomedical Optics Express, 2011. **2**(8): p. 2307-16.

98. Mitsuhashi, M., et al., *Examination of the rat model of liver injury via thioacetamide (TAA) or carbon tetrachloride (CCl4).* Journal of toxicologic pathology, 2004. **17**(3): p. 219-222.

99. Ruwart, M.J., et al., *The integrated value of serum procollagen III peptide over time predicts hepatic hydroxyproline content and stainable collagen in a model of dietary cirrhosis in the rat.* Hepatology, 1989. **10**(5): p. 801-6.

100. Tretheway, D., et al., *Should trichrome stain be used on all post-liver transplant biopsies with hepatitis C virus infection to estimate the fibrosis score?* Liver Transplantation, 2008. **14**(5): p. 695-700.

101. He, Y., et al., *Toward surface quantification of liver fibrosis progression.* Journal of Biomedical Optics, 2010. **15**(5): p. 056007.

102. Otsu, N., *A threshold selection method from gray-level histograms.* IEEE Transactions on Systems Man and Cybernetics, 1979. **9**(1): p. 62-66.

103. Lloyd, S.P., *Least squares quantization in PCM.* IEEE Transactions on Information Theory, 1982. **28**(2): p. 129-137.

104. Dempster, A.P., N.M. Laird, and D.B. Rubin, *Maximum likelihood from incomplete data via the EM algorithm.* Journal of the Royal Statistical Society. Series B (Methodological), 1977: p. 1-38.

105. Xu, S., et al., *Automated scoring system for liver fibrosis diagnosis with second harmonic generation microscopy.* Australian Journal of Intelligent Information Processing Systems, 2010. **12**(2).

106. Batts, K.P. and J. Ludwig, *Chronic hepatitis. An update on terminology and reporting.* The American Journal of Surgical Pathology, 1995. **19**(12): p. 1409-17.

107. Desmet, V.J., et al., *Classification of chronic hepatitis: diagnosis, grading and staging.* Hepatology, 1994. **19**(6): p. 1513-20.

108. Scheuer, P.J., *Classification of chronic viral hepatitis: a need for reassessment.* Journal of Hepatology, 1991. **13**(3): p. 372-4.

109. Hall, G., K.W. Eliceiri, and P.J. Campagnola, *Simultaneous determination of the second-harmonic generation emission directionality and reduced scattering coefficient from three-dimensional imaging of thick tissues.* Journal of Biomedical Optics, 2013. **18**(11): p. 116008.

110. Cortes, C. and V. Vapnik, *Support-vector networks.* Machine Learning, 1995. **20**(3): p. 273-297.

111. Chang, C. and C. Lin, *LIBSVM - a library for support vector machines.* www.csie.ntu.edu.tw/~cjlin/libsvm/.

112. Narmada, B.C., et al., *Hepatic stellate cell-targeted delivery of hepatocyte growth factor transgene via bile duct infusion enhances its expression at fibrotic foci to regress dimethylnitrosamine-induced liver fibrosis.* Human Gene Therapy, 2013. **24**(5): p. 508-19.

113. Hamamatsu, *Hamamatsu Photomultiplier Tube Handbook.* 3 ed.

114. Adler, M., et al., *Hepatitis C virus: the burden of the disease.* Acta Gastro-Enterologica Belgica, 2002. **65**(2): p. 83-6.

115. Fischer, A., C. Cremer, and E.H. Stelzer, *Fluorescence of coumarins and xanthenes after two-photon absorption with a pulsed titanium-sapphire laser.* Applied Optics, 1995. **34**(12): p. 1989-2003.

116. Cha, J.W., et al., *Reassignment of scattered emission photons in multifocal multiphoton microscopy.* Scientific Reports, 2014. **4**: p. 5153.

117. Takahashi, T., *Three-dimensional morphology of the liver in cirrhosis and related disorders.* Virchows Archiv. A, Pathological Anatomy and Histology, 1978. **377**(2): p. 97-110.

118. Hoofring, A., J. Boitnott, and M. Torbenson, *Three-dimensional reconstruction of hepatic bridging fibrosis in chronic hepatitis C viral infection.* Journal of Hepatology, 2003. **39**(5): p. 738-41.